OXFORD UNIVERSITY PRESS | Journal of Petrology

Draft Manuscript for Review

Crystals and melt inclusions record deep storage of superhydrous magma prior to the largest known eruption of Cerro Machín volcano, Colombia

Journal:	*Journal of Petrology*
Manuscript ID	JPET-Aug-23-0126.R2
Manuscript Type:	Original Manuscript
Date Submitted by the Author:	24-Aug-2024
Complete List of Authors:	Castilla, Silvia; University of Maryland at College Park, Geology Newcombe, Megan E.; University of Maryland at College Park, Department of Geology Piccoli, Philip; University of Maryland at College Park, Geology Peterson, Liam D.; University of Maryland at College Park, Department of Geology
Keyword:	melt inclusions, plagioclase hygrometer, plinian eruption, storage condition, superhydrous melt
Journal of Petrology now offers Virtual Collections of published papers. You may choose up to three collections from the list below. Virtual collections will increase the visibility of your work.:	Subduction Zones < Province Themes, Melt and Fluid Inclusions < Material Themes, Continental Crustal Genesis and Evolution < Process Themes

Crystals and melt inclusions record deep storage of superhydrous magma prior to the largest known eruption of Cerro Machín volcano, Colombia

Castilla, Silvia[1*]; Newcombe, Megan E.[1]; Piccoli, Philip M.[1]; Peterson, Liam D.[1]

[1] Department of Geology, University of Maryland, College Park, Maryland, 20742, United States

***Corresponding author:** sccm1705@terpmail.umd.edu

Tel: +1 4372431560

ABSTRACT

Cerro Machín, a volcano located in the northern segment of the Andes, is considered one of the most dangerous volcanoes in Colombia with an explosive record that involves at least five plinian events. Prior studies focused on the last dome-building eruption have suggested the presence of a water-rich mid-crustal magma reservoir. However, no direct volatile measurements have been published and little work has been completed on the explosive products of the volcano. Here, we study the largest known eruption of Cerro Machín volcano which occurred 3600 yr BP producing dacitic pyroclastic fall deposits that can be traced up to 40 km from the vent. Lapilli pumice clasts have a mineral assemblage of plagioclase, amphibole, quartz, and biotite phenocrysts, with accessory olivine, Fe-Ti oxides, and apatite. The occurrence of Fo_{89-92} olivine rimmed by high Mg# amphibole and the established high-water contents in the magma imply the presence of magma near or at water saturation at pressures >~500 MPa. Measurements of up to 10.7 wt% H_2O in melt inclusions hosted in plagioclase and quartz in the 3600 years BP eruption products support the idea that Cerro Machín is a remarkably water-rich volcanic system. Moreover, this is supported by measurements of ~103 – 161 ppm H_2O in plagioclase phenocrysts. The application of two parameterizations of water partitioning between plagioclase and silicate melt allows us to use our water in plagioclase measurements to estimate equilibrium melt water contents of 5 ± 1 – 11 ± 2 wt% H_2O, which are in good agreement with the water contents we measured in melt inclusions. Results of amphibole geobarometry are consistent with a magma reservoir stored in the mid-to-lower crust at a modal pressure of 700 ± 250 MPa, corresponding to a depth of ~25 km. Minor crystallization in the shallow crust is also recorded by amphibole barometry and calculated entrapment pressures in melt inclusions. Amphibole is present as unzoned and zoned crystals. Two populations of unzoned amphibole crystals are present, the most abundant indicate crystallization

conditions of 853 ± 26 °C (1 se; standard error), and the less abundant crystallized at an average temperature of 944 ± 24 °C (1 se). Approximately 18% of the amphibole crystals are normally or reversely zoned, providing evidence for a minor recharge event that could have been the trigger mechanism for the explosive eruption. Plagioclase crystals also show normal and reverse zoning. The moderate Ni concentrations (<1600 μg/g) in the high-Fo olivine xenocrysts suggest that Cerro Machín primary magmas are generated by inefficient interaction of mantle peridotite with a high-silica melt produced by slab melting of basaltic material. Some sediment input is also suggested by the high Pb/Th (>2.2), Th/La (0.3 – 0.4), and low La/Th (<13; relative to mantle array) ratios. Whole rock chemistry reveals heavy rare earth element (HREE) depletion and Sr enrichment that likely formed during the crystallization of garnet and amphibole in the upper part of the mantle or lower portion of the crust, promoting the formation of water-rich dacitic magma that was then injected into the middle-to-lower crust. Textural and compositional differences in the crystal cargo that erupted during dome-building and plinian events support the idea that large volumes of magma recharge lead to effusive eruptions, while only small recharge events are needed to trigger plinian eruptions at Cerro Machín.

Keywords: melt inclusions; plagioclase hygrometer; plinian eruption; storage condition; superhydrous melt

1. INTRODUCTION

Cerro Machín is a stratovolcano located in one of the most populated areas of Colombia (Méndez *et al.,* 2002) and is considered one of the most dangerous volcanoes in the country (Gómez *et al.*, 2021). Stratigraphic studies have revealed its highly explosive eruptive past including one vulcanian and five plinian to subplinian eruptions (VEI = 5; Rueda, 2005) of dacitic composition over the last 5000 years (Rueda, 2005). Seismic activity reported from 2007 – 2015 accompanied by variations in composition and temperatures of the hot springs, ground deformation, and radon outputs (Londoño, 2016; Inguaggiato *et al.*, 2017) suggest an active magmatic system. Prior work on the dome-building eruptions of Cerro Machín used amphibole chemistry to constrain the pre-eruptive magma water content (Laeger *et al.,* 2013); however, there are no direct measurements of magma volatile concentrations reported in the literature. In light of this, we performed water and carbon dioxide measurements in quartz- and plagioclase-hosted melt inclusions found in pumice clasts from the largest known plinian eruption (3600 yr BP). Surprisingly, our results suggest that Cerro Machín erupts dacitic magma containing up to 10.7 wt% H_2O (magmas containing >8 wt% H_2O have been previously defined as superhydrous magmas; Goltz *et al.*, 2020) that, according to amphibole barometry, is stored in a region that extends from lower- to mid-crustal pressures (with a 25th percentile of 550 ± 200 MPa and a 75th percentile of 700 ± 200 MPa using the Putirka, 2016 barometer).

The presence of superhydrous magma beneath a small number of continental arcs has been argued based on volatile measurements in lower crustal cumulates (Urann *et al.*, 2022), coexistence of high-Mg# (molar Mg/(Mg+Fe)) amphibole and forsterite in natural samples (Goltz *et al.*, 2020), the products of water-saturated phase equilibria experiments (Conrad *et al.*, 1988; Carmichael, 2002; Prouteau & Scaillet, 2003; Grove *et al.*, 2005; McCanta *et al.*, 2007; Krawczynski *et al.*,

2012; Lu *et al.*, 2015), calculations from volcanic and hydrothermal gas discharges (Fischer & Marty, 2005), and electron microprobe measurements of melt inclusions with analytical totals <92 % (Grove *et al.*, 2003). We have identified the presence of deep water-rich magma beneath Cerro Machín using multiple techniques including: (1) comparison of the mineral phase assemblage at Cerro Machín volcano (CMV) with phase equilibria experiments on similar magma compositions; (2) measurements of water in melt inclusions; and (3) measurements of water concentrations in plagioclase. We present these measurements and constraints of the water budget of the CMV system, and we consider the following possible origins of the water-rich nature of CMV magma: (1) interaction between hydrous high-Si melts, derived from the subducting plate, and peridotite in the overlying mantle wedge (Kelemen *et al.*, 2003; Yogodzinski *et al*., 2015); and (2) extensive fractionation of garnet and amphibole in the deep crust or upper mantle (Alonso-Perez *et al.,* 2009; Castillo, 2012; Blatter *et al.*, 2023).

2. GEOLOGICAL BACKGROUND

Cerro Machín volcano is located in the northern segment of the Central Cordillera of Colombia (latitude 4°29'N; longitude 75°23'W) and formed as the result of subduction of the Nazca Plate beneath the South American Plate (Fig. 1a). Along with eight other volcanoes, including Nevado del Ruiz volcano—Colombia's most active volcano, renowned for the 1985 eruption that claimed more than 20,000 lives—Cerro Machín belongs to the Cerro Bravo-Cerro Machín volcanic complex. Its edifice is located at the intersection between two major faults, the Cajamarca fault, a dominantly strike-slip fault with vertical displacement, and the Machín fault that is interpreted as a normal fault with dextral-lateral displacement (Mosquera *et al.*, 1982; Rueda, 2005; Murcia *et al.*, 2008).

Cerro Machín's volcanic edifice reaches an altitude of 2750 m.a.s.l and has a crater diameter of 2.4 km. It has been classified as a stratovolcano with a dacitic intra-crater lava-dome complex (Cepeda *et al.*, 1995; Arango Palacio, 2012). The volcanic sequence comprises at least six major events. Radiometric carbon dating suggests that these events occurred >5000, 4500, 3600, 2500, 1200, and 900 yr BP (Cepeda *et al.*, 1995; Méndez *et al.*, 2002; Rueda, 2005), suggesting that the repeat interval of VEI > 5 eruptions is ~900 years (Rueda, 2005). Given that the last event of this magnitude occurred ~900 years ago, it is particularly important to carefully consider any increasing activity at CMV. From 2007 to 2015, seismic activity in the Cerro Bravo-Cerro Machín Volcanic Complex was reported by the Colombian Geological Survey (Londoño, 2016), suggesting an active magmatic system. Since then, CMV activity has been designated as "level III" (yellow) by the Colombian Geological Survey, which means "changes in the volcanic activity in this case related to seismic events and fumarolic activity" (Colombian Geological Survey, 2023). In light of this, developing our understanding of the CMV volcanic system is time-sensitive and of crucial importance for assessing the likelihood and nature of future eruptions.

In this study, we focus on pyroclastic fall deposits associated with the third and most explosive event at ~3600 yr BP (designated event "P1" with a VEI of 5 by Rueda, 2005). We prioritized the study of this eruption because it is recognized as the most hazardous example of CMV activity and possibly the worst-case scenario for a future eruption. Moreover, the associated deposits constitute a marker horizon up to 40 km from the vent (Méndez *et al.*, 2002; Rueda, 2005) providing easy access for sampling and description. Close to the vent, we observed interlayering of clast-supported and matrix-supported layers that contained charcoal fragments and that were identified as pyroclastic flows. We avoid using these samples in order to minimize the possibility of post-eruptive water loss during their high-temperature emplacement. All samples were therefore

obtained at location CMV-008 (Fig. 1b) where no charcoal fragments were observed and where most of the other stratigraphic units were exposed (e.g., on Fig. 2a, the 5000 yr BP event is labeled "Espartillal", the 4500 yr BP event is labeled "P0" and the 3600 yr BP event is labeled "P1" following the unit names proposed by Rueda, 2005). The P1 deposit was divided into two lithofacies (designated *a* and *b*) based on their different sedimentary structures—massive versus laminated, and coarse- versus fine-grained (Fig. 2b). Single pumice clasts were collected from the massive lithofacies (*b*) which likely represents the climactic phase of the eruption (Paladio-Melosantos *et al*., 1996; Rosi *et al*., 2001). However, we acknowledge that there may have been other transient activity of this eruption that is not represented in this location. The size of the collected pumice clasts ranges from medium lapilli to coarse lapilli with diameters of 10 – 64 mm. We intentionally selected pumices from the relatively small lapilli grain-size fraction because such small clasts are quenched rapidly upon eruption, thereby minimizing the effects of diffusive water loss during post-eruptive cooling (Lloyd *et al.*, 2013).

3. METHODS

3.1. Sample preparation

We selected ten pumice clasts to cut in half, and one-half of each pumice clast was made into a thin section by Spectrum Petrographics, Inc. The remaining halves of these pumice clasts as well as some additional pumice clasts were lightly crushed and sieved for crystal picking. Plagioclase and quartz phenocrysts were separated by hand using a binocular microscope. Phenocrysts were immersed in isopropanol to increase the visibility of cracks, melt inclusions, and melt re-entrants (i.e. melt embayments) within the crystals. Selected crystals were mounted in Crystalbond and polished on two sides until melt inclusions were doubly or singly exposed. We chose melt inclusions that were wholly enclosed (i.e., no cracks or re-entrant features) regardless of their

position within the crystal (i.e., in the core or closer to the rim). We analyzed a total of 35 melt inclusions hosted in 27 different crystals by Fourier Transform Infrared Spectroscopy (FTIR; Section 3.2; Supplementary Table A1). All melt inclusions contained multiple small vapor bubbles, with a greater abundance of bubbles observed in the quartz-hosted melt inclusions. These bubbles unfortunately made it difficult to measure water concentration profiles in melt re-entrants.

After FTIR analysis, melt inclusions were placed in dental resin for electron microprobe (EPMA) analysis. Due to the fragility of some wafers, a total of 13 melt inclusions were lost and only 22 were measured by EPMA (Supplementary Table A1). Once hardened, mounts were polished with 0.3-μm diamond paste to remove any contaminants acquired during the preparation process (e.g., vacuum grease and resin). To corroborate our FTIR results, a set of eight melt inclusions hosted in quartz crystals were mounted in indium for analysis by secondary ion mass spectrometry (SIMS; Section 3.5).

A set of 17 plagioclase crystals with a size range between 1.5 and 7.6 mm were prepared for water content analysis by FTIR. Each crystal was cut in half and the two halves were polished into two mutually perpendicular slabs. Measurements were performed in both slabs in order to calculate total water content from three perpendicular axes, regardless of their optical direction (Johnson & Rossman, 2004). After their analysis by FTIR, crystals were placed in a 1-inch diameter dental resin plug for analysis by EPMA.

3.2. Fourier Transform Infrared Spectroscopy analyses of melt inclusions

Transmission infrared spectra of 35 plagioclase- and quartz-hosted melt inclusions were obtained using a Thermo Nicolet iN10 MX Fourier transform infrared spectrometer with a liquid nitrogen-cooled MCT detector at the University of Maryland. The sample and surroundings were continuously purged with dry, CO_2-free air to limit any contribution from atmospheric water and

carbon dioxide to the spectra. The width of the square aperture used to focus the infrared beam was adjusted to 10, 15, 20, 25, and 30 microns based on the size of each melt inclusion. Spectra from at least three different aperture sizes were measured per melt inclusion in order to calculate the uncertainty in the absorbance peak heights due to aperture size. Spectra were collected at 4 cm^{-1} resolution between a wavenumber range of 700 to 7000 cm^{-1} and 256 scans were averaged to reduce noise. Molecular water absorbs infrared light at frequencies of 5,200 cm^{-1} and 1,630 cm^{-1}, while hydroxyl absorbs infrared light at 4,500 cm^{-1} (Newman *et al.,* 1986). Both molecular water (H_2O_m) and hydroxyl (OH) contribute to the fundamental OH stretching vibration at 3,550 cm^{-1}. When melt inclusions showed a saturated 3,550 cm^{-1} peak, total water concentrations (H_2O_m + OH) were calculated from the heights of the 5,200 cm^{-1} and 4,500 cm^{-1} peaks using the calibration equations of Zhang *et al.* (1997). We additionally applied the molar absorption coefficients of Newman *et al.* (1986), Ohlhorst *et al.* (2001), and Nishimura *et al.* (2005) (see Supplementary Table A1). For these calibrations, water concentration was calculated from peak heights using the Beer-Lambert Law (Eq. 1)

$$C = \frac{(mw)*(A)}{\rho*d*\varepsilon} \quad (1)$$

where C is the concentration of water in weight fraction of the absorbing species, mw is the molecular weight (g/mol) of the volatile species (18.02 for total H_2O and 44.01 for CO_2), A is the absorbance peak height, ρ is the density of the glass (g/L), d is the inclusion thickness (cm), and ε is the molar absorption coefficient (L/mol·cm). The absorbance peak height was measured with the OMNIC software using a straight baseline in all cases. This approach was chosen due to the absence of pronounced curvature in the baselines of the spectra and the absence of adjacent overlapping peaks, making a linear baseline the most reproducible and easily defined method (e.g., Behrens *et*

188 *al.,* 1996; Ihinger *et al.,* 1999; Zhang, 1999; Von Aulock *et al.,* 2014; Chen *et al.,* 2015). In rhyolitic
189 compositions, glass densities strongly depend on total water concentration, therefore the use of an
190 iterative process is required to converge on appropriate values [Eq. 2 (Myers *et al.,* 2019; modified
191 from Skirius, 1990)]:

192 $$\rho = 2350 - 12.6\, C_{H_2O} \quad (2)$$

193 where ρ is the glass density (g/L), C_{H_2O} is the concentration of total dissolved H_2O in wt% for each
194 analytical spot. Carbon dioxide is present as molecular CO_2, which exhibits an absorbance peak at
195 2,350 cm^{-1}. The absorption coefficient (ε) for molecular CO_2 in rhyolitic glass is 1,214 L/mol·cm
196 (Behrens *et al.*, 2004). In Table 1, we report water contents calculated by the Zhang *et al.* (1997)
197 and Newman *et al.* (1986) calibrations and carbon dioxide calculated by the Behrens *et al.* (2004)
198 calibration.

199 Multiple methods were used to measure the thicknesses of the melt inclusions. Wafer
200 thicknesses of doubly exposed melt inclusions were measured using a calibrated stereo zoom lens
201 with a 1-mm objective on the Leica S9i Stereomicroscope. We turned the wafers on their sides such
202 that we could see the wafer edges when observed using the microscope (see Supplementary Figure
203 A3). The thickness of each wafer was measured in multiple places along the wafer edge using the
204 LASX software and these measurements were averaged for use in the following calculations.

205 Some of the melt inclusions were singly exposed. For these wafers, the method of Tollan *et*
206 *al.* (2019) was applied to estimate the proportion of melt versus quartz sampled by the FTIR beam.
207 The total wafer thicknesses of these samples were left thick enough that we could measure them
208 using a Mitutoyo digimatic indicator, a tool with a precision of approximately ± 3 μm, without
209 risking breakage or loss of the wafers. The proportion of melt versus quartz in the beam path can
210 then be estimated using the relative heights of the quartz overtone bands at ~2,136 cm^{-1} for analyses

measured through the melt inclusion, and through the quartz host at a location near the melt inclusion, by applying the following equation [Eq. 3 (Tollan *et al.*, 2019)]:

$$Thickness\ of\ MI\ (\mu m) = \frac{A_{Quartz} - A_{Quartz+MI}}{A_{Quartz}} \times\ measured\ wafer\ thickness\ (\mu m) \qquad (3)$$

where A_{Quartz} is the integrated absorbance of the 2,136 cm^{-1} overtone of pure quartz adjacent to the melt inclusion, $A_{Quartz+MI}$ is the integrated absorbance of the 2,136 cm^{-1} overtone band through the melt inclusion and measured wafer thickness is the total thickness of the quartz wafer.

Total water concentration was measured in 17 plagioclase crystals by FTIR using polarized transmission spectra in three orthogonal directions (X, Y, Z) that did not necessarily correspond to optical directions (Johnson & Rossman, 2004). Two perpendicular line traverses (referred to as North-South and East-West) were measured across both halves of the crystals to characterize variations in their water concentrations. Water concentrations in the plagioclase crystals were quantified using the Beer-Lambert Law with the following modifications:

$$C = \frac{A_{int}}{\rho * d * \varepsilon_{int}} \qquad (4)$$

where C is the concentration of water in weight ppm H_2O, A_{int} is the total integrated area of OH-related bands in the region 3,700 – 2,600 cm^{-1}; ρ is the density of plagioclase (2.65 g/cm^3); d is the thickness of the crystal section which was measured by a micrometer with ± 3 μm uncertainty; and ε_{int} is the integral absorbance coefficient for the hydrous species Type IIa OH in plagioclase (202,600 ± 20,260 $L \cdot mol^{-1}$ H_2O cm^{-2}; Mosenfelder *et al.,* 2020). Note that the water in plagioclase is thought to dissolve as hydroxyl; however, the concentration of water is quantified as weight ppm H_2O (Johnson & Rossman, 2004).

3.3. X-ray fluorescence (XRF)

Whole rock chemistry of five pumice clasts with different textures from P1 was measured by X-ray fluorescence (XRF) spectrometry at the Department of Earth & Environment at Franklin and Marshall College. A PANalytical Zetium X-ray fluorescence vacuum spectrometer was used to analyze bulk major and trace element compositions of the pumice clasts. Iron was measured by titration against standard $K_2Cr_2O_7$ solution in acid medium using sodium diphenylamine sulfonate as the indicator. Three replicate measurements of FeO in the NBS-688 basalt standard were used to calculate a correction factor for the batch of samples and the error percentage in the FeO measurements (0.1%). Moreover, %FeO (by titration) was used to calculate $\%Fe_2O_3$, Fe^{2+}, and Fe^{3+}. These values were used to estimate the whole rock Mg# and the oxygen fugacities of the samples (see Results section).

3.4. Electron probe microanalysis (EPMA)

Major element concentrations of minerals, melt inclusions, and matrix glass were analyzed using a JEOL 8900R electron probe microanalyzer (EPMA) at the Maryland Nanocenter, University of Maryland – College Park. The operating conditions for amphibole and plagioclase analyses were an accelerating voltage of 15 kV, a beam current of 20 nA, and a beam diameter of 10 μm. The same conditions were used for olivine analyses, but with a beam diameter of 1 μm. Quantitative analyses were made using well-characterized natural and synthetic standards. Amphibole standards include Kakanui Hornblende (USNM 143965) for Na_2O, K_2O, FeO, CaO, MgO, Al_2O_3, SiO_2, TiO_2, and Rhodonite (USGS PXBH) for MnO. For olivine analyses we used San Carlos Olivine (USNM 111312/444) for SiO_2, FeO, MgO and NiO; Bushveld Chromite for Cr_2O_3; Rhodonite (USGS PXBH) for MnO; Anorthite (USNM 137041) for CaO Al_2O_3; albite for Na_2O; microcline for K_2O; and ilmenite for TiO_2. Plagioclase standards include Lake County plagioclase for CaO, Al_2O_3, SiO_2; albite (USGS FSTA) for Na_2O; Kakanui Hornblende (USNM 143965) for TiO_2, MgO and

FeO; Rhodonite (USGS PXBH) for MnO; and microcline for K_2O. Concentrations were calculated from x-ray fluxes using a phi-rho-Z algorithm (Armstrong, 1988).

Melt inclusions and glass matrix were analyzed with operating conditions of 15 kV, an electron beam current of 2.5 nA, and a beam diameter of 10 μm. Low current was used to minimize diffusion of mobile species such as Na and H_2O. Accuracy was assessed by measuring 10 analyses of the Morgan & London (1996) hydrous glasses (Supplementary Table B1). Each melt inclusion was observed using back-scattered electron imaging (BSE) for signs of post-entrapment crystallization (PEC), cracks, and surface topography.

3.5. Secondary Ion Mass Spectrometry (SIMS)

Water concentrations (total H quantified as H_2O equivalents) in five melt inclusions were measured using the Cameca NanoSIMS 50L at the Carnegie Earth and Planets Laboratory, Washington D.C. The vacuum in the analysis chamber was maintained between 2.5 x 10^{-9} and 1.7 x 10^{-9} torr. Analyses were conducted using entrance slit (ES) 5 and aperture slit (AS) 4. A 15x15-μm area was chosen for each analysis which was subsequently pre-sputtered for ~3 min with a 2-nA Cs^+ primary beam to remove the Au coat and surface contamination. Following pre-sputtering, the raster size was reduced to a 10x10-μm area for the duration of the analytical counting time (7 min 10 s). Electronic gating and beam blanking further focused the ion collection to the central 5x5-μm region of the analytical area. Negatively charged $^{12}C^-$, $^{16}O^1H^-$, $^{19}F^-$, $^{30}Si^-$, $^{32}S^-$ and $^{35}Cl^-$ ions were simultaneously detected using electron multipliers with a mass resolving power of >8000 (MRP; as defined by Cameca), allowing discrimination of $^{16}O^1H^-$ from ^{17}O. The real-time imaging (RTI) function of the NanoSIMS 50L was used to generate heat maps of ion counts and check for hot spots (e.g., cracks) that represent sources of contamination. If hot spots were identified, the beam was moved to another area until a suitable analytical area was identified. The electron gun was used

to charge-compensate the sample surface due to the implantation of Cs^+ ions and the removal of negatively charged ions and electrons during analyses. Electron gun tuning followed the same procedure as Peterson *et al.* (2023). Counts of volatile ions ($^{12}C^-$, $^{16}O^1H^-$, $^{19}F^-$, $^{32}S^-$, and $^{35}Cl^-$) were ratioed against $^{30}Si^-$ to account for instrumental drift; e.g., due to variations in the primary beam and electron gun tuning. The data were then SiO_2-corrected by multiplying $^{30}Si^-$ normalized ion counts by the SiO_2 concentration of the target, as measured by electron microprobe, divided by 50 (e.g., $^{16}O^1H^-/^{30}Si^-$ x SiO_2/50). We note that the factor of 50 is applied for convenience because most geological materials contain ~50 wt% SiO_2, so adoption of this factor produces a SiO_2 correction factor close to 1; however, the choice of scalar does not affect the reported volatile concentrations. The SiO_2 correction was applied to account for variations in the SiO_2 content of the standards and samples that would otherwise produce variations in measured $^{30}Si^-$ normalized ion counts (e.g., Newcombe *et al*., 2020; Peterson *et al.*, 2023; Towbin *et al.,* 2023). No blank corrections and no secondary drift corrections were applied to the data.

Water concentrations were calibrated using FTIR measurements of a set of rhyolite glasses (71 – 73 wt% SiO_2) with 3 to 6 wt% of H_2O (see Supplementary Table C1 for references). Suprasil 3002 glass containing ~2 ppm H_2O (Newcombe, 2022) was used to monitor the analytical blank (2.7 ± 0.35 ppm; see Supplementary Table C1). Repeat measurements of standard N6 were used to assess the reproducibility of analyses of materials with high-water contents.

4. RESULTS

4.1. Petrography and mineral chemistry

Lapilli pumice clasts contain plagioclase, amphibole, quartz, and biotite phenocrysts, with accessory Fe-Ti oxides and apatite (listed by order of abundance). All of these mineral phases are

also present as microlites in the groundmass. Rare olivine (n=10) with a Mg# of 89–92 and orthopyroxene (n=1) with a Mg# of 92 were also observed.

Plagioclase is present as euhedral to subhedral phenocrysts (>2 mm), microphenocrysts (0.5 – 2 mm) and microcrysts (<0.5 mm) that can be grouped into three distinct textures (listed here in decreasing order of abundance): (1) low-An ($An_{24–38}$) crystals presenting oscillatory and patchy zoning with limited compositional variation from core (An_{24-34}) to rim (An_{28-38}); (2) oscillatory zoned crystals with an intermediate An core (An_{36-43}) and an euhedral rim (An_{30-35}) (Fig. 3a); and (3) rare anhedral zoned crystals with a rounded core (An_{28-34}), occasionally mantled by a reabsorbed rim, and an outermost higher An rim (An_{42-48}). The low-An crystals with limited compositional variation are by far the most abundant (~70%; see Fig. 4a).

Amphibole ranges from euhedral to anhedral microphenocrysts (0.5 – 2 mm) and microcrysts (<0.5 mm). Most amphiboles have magnesio-hastingsite compositions following the classification of Leake *et al.* (1997), while some are classified as pargasite. Analyses with low totals (<98 wt %) and deviations from the idealized stoichiometry were recognized using the amphibole formula of Ridolfi (2021) and Li *et al.* (2020). Four different populations of amphiboles can be distinguished on the basis of their mineral chemistry: (1) low-Mg unzoned amphiboles with a Mg# range of 53 – 62 (Fig. 3b); (2) high-Mg unzoned amphiboles with a Mg# of 66 – 76; (3) normally zoned amphiboles with a Mg-rich core (Mg# 61 – 77) and a Mg-depleted rim (Mg# 54 – 58) (Fig. 3c); and (4) reversely zoned crystals with Mg# 53 – 60 in their core, mantled by a Mg-rich rim with Mg# 65 – 76. The unzoned, low-Mg amphiboles are by far the most abundant (77%; Fig. 4b).

Quartz microphenocrysts (0.5 – 2 mm) and microcrysts (<0.5 mm) are anhedral, and frequently contain vapor-bubble-filled melt embayments/re-entrants. Biotite is present as euhedral to subhedral phenocrysts, microphenocrysts and microcrysts that are broken or deformed. Rounded

microcrysts and phenocrysts surrounded by plagioclase crystals were also observed. Fe-Ti oxides occur as inclusions in plagioclase, amphibole, and biotite or as microcrysts in the groundmass. Rare olivine occurs as microphenocrysts and microcrysts with a Mg# of 89 – 92. Rare olivine and orthopyroxene crystals are surrounded by allotriomorphic amphibole overgrowths with Mg# ranging from 73 – 80 (Fig. 3d).

4.2. Whole rock chemistry

Major and trace element concentrations in the lapilli pumice clasts show little variation in SiO_2 (Supplementary Table B2), regardless of their textural differences (white versus gray pumices). All samples are classified as medium-K, calc-alkaline dacites on a total alkalis versus silica (TAS) diagram, with SiO_2 contents ranging from 63.6 to 66.4 wt%, and total alkalis ranging from 5.9 to 6.4 wt% (Fig. 5a). Harker diagrams for Al_2O_3, TiO_2, FeO_T, P_2O_5, and CaO show negative correlations with SiO_2, which is consistent with fractional crystallization of plagioclase, pyroxene, apatite, and Fe-Ti oxides (see Supplementary Figure B1). Whole rock MgO is negatively correlated with SiO_2; however, this negative correlation is not observed in analyses of matrix glass or melt inclusions, which are found to have SiO_2 contents of 65.2 to 79.2 wt%. Whole rock K_2O is positively correlated with SiO_2 due to its incompatible behavior in the mineral phases present.

The calc-alkaline affinity of CMV dacites is supported by trace element distribution plots normalized to primitive mantle values (from Sun & McDonough, 1989). An enrichment of large ion lithophile elements (LILE; including the fluid-mobile trace elements K, Ba, Pb, Sr) and the presence of a negative Nb anomaly are typical features of arc-derived calc-alkaline magmas (Schmidt & Jagoutz, 2017).

The Cerro Machín Volcano (CMV) dacites can be classified as adakites based on their major and trace element composition (Samaniego *et al.,* 2005; Fig. 5b, c, d). Moreover, CMV

samples are characterized as high-silica adakites on a Cr/Ni vs. TiO_2 diagram (Fig. 5d; Martin *et al.*, 2005). The potential origins of this adakite signature and the distinctive major and trace element concentrations in CMV dacites are discussed in Section 5.5.

A Mg# range of 63 – 71 was calculated using FeO and MgO from the whole rock chemistry as molar $Mg/(Mg + Fe^{2+})*100$. Additionally, FeO and Fe_2O_3 calculated from whole rock chemistry analysis (see section 3.3), an average temperature of 866 °C ± 35 °C (using the Putirka (2016) amphibole-liquid thermometer; see section 4.5) and a modal pressure of 7 00 MPa (see section 4.5) were used to obtain oxygen fugacities (Kress & Carmichael, 1991) above the nickel–nickel oxide buffer (NNO) with ΔNNO between +0. 89 and +1.59.

4.3. Volatile concentrations in melt inclusions

Melt inclusions ranging in size from 27 to 137 μm are observed in plagioclase and quartz phenocrysts. The inclusions typically have spherical shapes but faceted melt inclusions with trigonal bipyramidal shapes are also observed (Fig. 6a). Most melt inclusions contain multiple vapor bubbles, and we observed a greater abundance of vapor bubbles in the quartz-hosted melt inclusions than the plagioclase-hosted melt inclusions (Fig. 6b). A total of 35 melt inclusions hosted in plagioclase (16) and quartz (19) were analyzed using FTIR. We applied several published calibrations to calculate the water concentrations in the melt inclusions (Supplementary Table A1; Zhang *et al.*, 1997; Ohlhorst *et al.*, 2001; Newman & Lowerstern, 2002; Nishimura *et al.*, 2005). Here we report water contents calculated using the Zhang *et al.* (1997) calibration (Table 1) as it is the most widely used for rhyolite melt inclusions; however, we recognize the considerable uncertainties associated with the high-water analyses (uncertainties among the different calibrations are ~1 wt% for melts containing ~10 wt% H_2O). The measured water and carbon dioxide concentrations range between 0.5 to 10.7 wt% H_2O using the Zhang *et al.* (1997) calibration

and 0 to 445 ppm of CO_2 using the Behrens *et al.* (2004) calibration (Fig. 6c). Most melt inclusions have H_2O contents between ~3 and ~ 6 wt% (25th and 75th percentiles, respectively). Regardless of the calibration used, our high-water melt inclusions are among the most water -rich ever reported (Borisova *et al*., 2006; Gavrilenko *et al.*, 2019), suggesting that Cerro Machín is a remarkably hydrous volcanic system.

We measured five of the quartz-hosted singly exposed melt inclusions by NanoSIMS. The calibration curve was based on FTIR measurements in rhyolite glasses with up to 6 wt% H_2O (Supplementary Table C1; Fig. 7a). We obtained concentrations from 5.8 wt% to 7.7 wt% H_2O (Fig. 7b) and most of the SIMS values overlap within one standard deviation of our FTIR measurements. Despite the agreement, we acknowledge the large uncertainties of our FTIR measurements that demonstrate the limitations of this technique. Melt inclusions d1-Qz2, d1-Qz5 and d1-Qz7 (for which the melt inclusion thicknesses are estimated to occupy 9%, 14% and 6%, respectively, of their total wafer thicknesses) provide evidence of good agreement between both approaches (Fig. 7b). We note that Tollan *et al.* (2019) recommend that melt inclusion thickness should range between ~15 and 50% of the total wafer thickness in order to minimize the uncertainty of the singly-exposed melt inclusion approach. Unfortunately, our melt inclusions are quite small compared to those analyzed by Tollan *et al.* (2019), and our wafers had melt inclusion thicknesses that occupied <15% of the total wafer thickness. The disparity observed between our NanoSIMS and FTIR data for d1-Qz3 and d1-Qz6 might be related to the low melt inclusion:quartz thickness ratios of these wafers (9 and 4% of the total quartz thickness, respectively) which places a significant uncertainty on the melt inclusion thickness estimates and ultimately, on the FTIR calculations (Table 1; Tollan *et al.*, 2019). The significant drop in precision for these two melt

391 inclusions highlights the limitations of the singly-exposed melt inclusion approach for small melt
392 inclusions.

393 We used our measured water and carbon dioxide concentrations to calculate melt inclusion
394 entrapment pressures (Wallace *et al.*, 1999). Saturation pressures were calculated based on the
395 Newman & Lowenstern (2002) model for rhyolitic melts (Fig. 6c) and the Papale *et al.* (2006)
396 model using SOWLCAD from EUROVOLC: Volcano Dynamics Computational Centre
397 (Supplementary Table A1). We find that melt inclusions with water contents <~5 wt% were trapped
398 at pressures lower than 200 MPa whereas melt inclusions with water contents between 6.3 – 10.7
399 wt% were trapped at pressures from 234 to 462 MPa (VolatileCalc model, Newman & Lowerstern,
400 2002) or up to 728 MPa (Papale, 2006 model). These results are in good agreement with our mineral
401 thermobarometry estimates, although there is a bias in the melt inclusion record towards lower
402 pressures. The origin of this bias is discussed in Section 5.1.1.

403 Isopleths of constant vapor compositions containing between 1 and 10 mol. % CO_2 (i.e., 99
404 to 90 mol. % H_2O) provide a good match to our melt inclusion data (Fig. 6c) suggesting that the
405 CMV magma was buffered by an aqueous supercritical fluid and was supersaturated up to pressures
406 of 462 MPa (applying the VolatileCalc model). Supersaturation of the CMV magma is further
407 supported by the persistent presence of bubbles in the melt inclusions. Vapor bubbles in melt
408 inclusions that occupy relatively small (typically <10 vol. %; Moore *et al.*, 2015) and
409 approximately constant volume fractions of the inclusions have been attributed to melt shrinkage
410 and post-entrapment crystallization during cooling—such vapor bubbles have been found to
411 sequester CO_2 such that the measured CO_2 concentration in the melt is much lower than the initial
412 trapped CO_2 concentration (Hartley *et al.*, 2014; Moore *et al.*, 2015; Rasmussen *et al.*, 2020). In
413 CMV melt inclusions, however, the vapor bubbles occupy large and variable volume fractions of

the melt inclusions (Fig. 6a, b ; Supplementary Table A2 and Supplementary Figures A1 and A2). This feature may indicate decrepitation of the melt inclusions during decompression (e.g., Bachmann *et al.,* 2010; Wallace *et al.*, 2021; Borisova *et al.,* 2005), or alternatively, the persistent presence of vapor bubbles may indicate that the bubbles were present in the magma during the initial entrapment of the melt inclusions (Steele-MacInnis *et al.*, 2017); i.e., the magma was saturated with a supercritical fluid. Modeling of melt inclusions containing co-entrapped vapor bubbles suggests that the co-entrapped vapor buffers CO_2 in the melt during cooling such that there is minimal loss of CO_2 into the vapor phase (Steele-MacInnis *et al.*, 2017). As such, it is not appropriate to apply corrections to our measured CO_2 concentrations for the diffusion of CO_2 into the vapor, and it is possible that our measured CO_2 concentrations are a robust estimate of the CO_2 concentration in the initially trapped magma. However, we also acknowledge that some portion of the CO_2 in each melt inclusion may have been sequestered into the vapor phase during post-entrapment modification, in which case our melt inclusion pressure estimates may represent lower bounds.

4.4. Water concentration and partitioning in plagioclase

Nominally anhydrous minerals (NAMs) have been proposed as a powerful tool for estimating pre-eruptive water contents of magmas (e.g. Urann *et al.*, 2022). Reported concentrations of water in volcanic feldspar range up to hundreds of ppm H_2O (by weight) (Caseres *et al.*, 2018; Hamada *et al.*, 2011; Johnson & Rossman, 2004; Seaman *et al.*, 2006) and have been used to constrain the water content of their host melts by applying Henrian partition coefficients (Hamada *et al.*, 2013; Caseres *et al.*, 2017, 2018). We analyzed water concentrations in 17 plagioclase crystals with maximum diameters ranging between 1.5 and 7.6 mm and a compositional range of An_{28} to An_{40}. Crystals show oscillatory zoning with occasional melt inclusions; minimal and restricted evidence

of re sorption or disequilibrium features was observed. To calculate total water, FTIR spectra were measured in three perpendicular directions, and the thickness-normalized hydroxyl peak areas were summed. These measurements required the preparation of two mutually perpendicular slabs from each crystal (Fig. 8a). In the majority of the crystals, we obtained approximately uniform water contents (edge to edge) indicating the absence of observable water gradients associated with diffusive processes (Fig. 8b). We note that such gradients may be present within the outer few 10s of microns of the crystals, but if present, these gradients are not resolvable by our FTIR measurements. In order to constrain the diffusive length scale for water in the plagioclase crystals, we estimate the timescale of magma ascent based on the lack of observable breakdown rims on CMV amphibole crystals, and we calculate the characteristic diffusion length scale of water in plagioclase (x) during this magma ascent timescale (t) using the simplified equation $x = \sqrt{Dt}$, where D is the diffusivity of water in plagioclase. Using constraints on the time required for amphibole breakdown rims to develop (Rutherford & Hill, 1993), we estimate that CMV magma likely ascended from its storage region to the surface in less than ~3 days. Using the Arrhenius relationship provided by Johnson & Rossman (2013) at a temperature of 851 ℃ (obtained from amphibole thermobarometry), we obtain a diffusivity of water in plagioclase of $1.0 \times 10^{-14} m^2/s$. Therefore, applying the equation $x = \sqrt{Dt}$, we calculate a characteristic diffusion length scale for water in the plagioclase crystals of ~50 microns. This calculation suggests that the centers of the plagioclase crystals (which range in size from 1.5 to 7.6 mm) likely preserve the pre-eruptive water contents (i.e., the water contents they had in the magma storage region in the weeks to months preceding the eruption). To further support our assumption that the measured water concentrations represent their pre-eruptive storage values without syneruptive diffusive modification, we plotted

plagioclase crystal size versus water content. We did not find any relationship, supporting a lack of diffusional control on the central water concentrations of the CMV plagioclase crystals (Fig. 8c).

Currently and to the extent of our knowledge, there are no experimental studies of water partitioning between plagioclase and felsic melts relevant to CMV, and only one study for basaltic to basaltic-andesite melts under terrestrial conditions has been reported (Hamada *et al.*, 2013). The Hamada *et al*. (2013) study found evidence for non-Henrian behavior of water partitioning between plagioclase and melt. They fit their partitioning data to two constant partition coefficients, one for low-water (<1 wt% H_2O) melts and one for high-water (> 4 wt% H_2O) melts. Other studies calculated a partition coefficient (defined as $K_d = \frac{Concentration\ of\ water\ in\ plagioclase\ (wt\%)}{Concentration\ of\ water\ in\ melt\ (wt\%)}$) of ~0.002 (Mosenfelder *et al.,* 2020) based on plagioclase-melt inclusion pairs from dacitic-rhyolitic systems such as Mt. Saint Helens (Johnson, 2005), Mt. Hood (Caseres *et al.*, 2018), Mt. Mazama (Mosenfelder *et al.*, 2018) and the Huckleberry Ridge Tuff, Yellowstone (Rappoccio *et al.*, 2020). Partitioning data from Hamada *et al.* (2013) and Caseres *et al.* (2018) are compiled and plotted in Fig. 9.

The observation by Hamada *et al.* (2013) and Xu *et al.* (2024) that water concentrations in plagioclase may be a nonlinear function of the water concentration in the equilibrium melt suggests that the application of Henrian partition coefficients to water concentrations in plagioclase crystals is likely inappropriate. We note that hydrogen exists predominantly as hydroxyl and molecular water in silicate melts (Stolper, 1982; Dixon *et al.,* 1995) and predominantly as hydroxyl (or equivalently, protons associated with the oxygen lattice) in nominally anhydrous minerals (Rossman, 1996; Keppler & Bolfan-Casanova, 2006). The complex speciation of hydrogen in melts and minerals makes it unlikely that its partitioning is independent of water concentration because

the activity of molecular water and hydroxyl in silicate melts (and potentially in minerals) is known to vary non-linearly with total water concentration (e.g., Stolper, 1982).

In light of the complex speciation behavior of water in melts and minerals, thermodynamic models of partitioning and solubility in NAMs (i.e., nominally anhydrous minerals) have been developed (Kohlstedt & Mackwell, 1998; Keppler & Bolfan-Casanova, 2006; Adam *et al.,* 2016; Mitchell *et al*., 2017). Such models consider activity-composition relations of water in silicate melts and also account for different OH dissolution mechanisms in minerals. For example, the following reaction describes the dissolution of water in plagioclase as two independent hydroxyl groups (Keppler & Bolfan-Casanova, 2006):

$$H_2O^{fluid} + O^{plagioclase} = 2OH^{plagioclase} \quad (5)$$

in which H_2O^{fluid} is a hydrous fluid, $O^{plagioclase}$ is an unprotonated oxygen in the plagioclase structure and $OH^{plagioclase}$ is a hydroxyl group dissolved into the plagioclase structure (likely charge balanced by a vacancy or another trace element defect). The equilibrium constant for this reaction (K_1) can be approximated as follows:

$$K_1 = \frac{X_{OH}^{plagioclase^2}}{X_O^{mineral}.f_{H_2O}} \quad (6)$$

where $X_{OH}^{plagioclase}$ is the mole fraction of OH in plagioclase, $X_O^{plagioclase}$ is the mole fraction of unprotonated oxygens in plagioclase (a large enough reservoir that this quantity can be considered constant) and f_{H_2O} is the fugacity of water. Rearranging for $X_{OH}^{plagioclase}$, we find that the mole fraction of OH in plagioclase is expected to be proportional to the square root of water fugacity:

$$X_{OH}^{plagioclase} \propto \sqrt{f_{H2O}} \quad (7)$$

Water dissolves into silicate melts as both molecular water (H_2O_m) and hydroxyl (OH), via the following reactions (Stolper, 1982):

$$H_2O^{fluid} = H_2O_m^{melt} \quad (8)$$

$$H_2O_m^{melt} + O^{melt} = 2OH^{melt} \quad (9)$$

Combining these reactions, the equilibrium constant for the combined reaction (K_2) can be approximated as follows:

$$K_2 \cong \frac{X_{OH}^{melt2}}{X_O^{melt}.f_{H2O}} \quad (10)$$

At low total water concentrations, water dissolves in silicate melts predominantly as OH, and the dissolution of small quantities of water results in a negligible change in X_O^{melt}, such that X_O^{melt} can be assumed to be constant, and the following relationship holds (Newcombe *et al.,* 2017):

$$X_{OH}^{melt} \propto \sqrt{f_{H2O}} \quad (11)$$

This suggests that, in the low-pressure limit, $X_{OH}^{melt} \propto X_{OH}^{plagioclase} \propto \sqrt{f_{H2O}}$, which would indicate a constant melt-plagioclase partition coefficient for OH ; however, this treatment may not extrapolate to higher fH$_2$O, where the assumption of constant X_O^{melt} will be violated and the pressure dependence of the equilibrium constants may become significant. Notably, VolatileCalc (Newman & Lowenstern, 2002) predicts a maximum OH solubility in rhyolitic melt of ~2 wt%. Applying a constant OH partition coefficient of 0.006 [determined by applying the absorption coefficient for water in plagioclase of Mosenfelder *et al.* (2015) to the OH partitioning data of Hamada *et al.* (2013)], this implies a maximum dissolved OH in plagioclase of ~120 ppm. Our CMV plagioclase crystals contain water concentrations up to ~161 ppm, indicating that a constant OH partition coefficient cannot be accurately extrapolated to the high-water concentrations measured at CMV.

523 In the absence of high-pressure experiments to examine the partitioning behavior of water
524 between plagioclase and melt under conditions relevant to CMV, we fit the partitioning data of
525 Hamada *et al.* (2013) and Caseres *et al.* (2018) to a square root relationship between water in
526 plagioclase and water in melt. This empirical approach provides a good fit to the data across the
527 studied range of melt water contents (up to ~6 wt% H_2O; Fig. 9). By applying a least-squares
528 minimization to the existing experimental data (see caption to Fig. 9), we propose that the following
529 relationship can be used to calculate the water concentration of plagioclase in equilibrium with
530 basaltic to dacitic melt containing up to ~6 wt% H_2O:

531 $$C_{H_2O}^{plagioclase}(ppm) = 48\sqrt{C_{H_2O}^{melt}(wt\%)}, \quad (12)$$

532 where $C_{H_2O}^{plagioclase}$ is the concentration of water in plagioclase in wt ppm H_2O, and $C_{H_2O}^{melt}$ is the
533 total concentration of water in melt calculated as wt% H_2O.

534 Notably, the application of equation 12 to CMV magma containing > 6 wt% H_2O requires
535 extrapolation beyond the experimentally constrained water concentration range. Furthermore, at
536 high-water concentrations, the shape of the square root function means that small changes in the
537 measured water concentration of plagioclase result in large changes in the calculated water
538 concentration of the equilibrium melt; e.g., an increase in plagioclase water concentration from 150
539 to 160 ppm results in an increase in the calculated equilibrium melt water content from 10 to 11
540 wt% H_2O.

541 By applying equation 12 to the range of water concentrations that we measured in the
542 plagioclase crystals (103 – 161 ppm H_2O; Table 2), we calculate equilibrium melt water contents
543 from 5 ± 1 to 11 ± 2 wt% H_2O (with a 25th percentile of 6 wt% H_2O and a 75th percentile of 8 wt%
544 H_2O), which are in good agreement with the water contents we measured in melt inclusions (Fig.
545 10a). Alternatively, application of a constant partition coefficient of 0.002 (Mosenfelder *et al.,*

546 2020) results in a range of equilibrium melt water contents from 5 to 8 wt%. We note that further
547 experiments are required to determine whether equation 12 is adequate to describe water
548 partitioning between silicate melts and plagioclase crystals, or whether additional terms are
549 required to account for dependences on melt and/or crystal composition, temperature, pressure, or
550 oxygen fugacity (e.g., Lin *et al.* 2019).

551 Finally, we applied the plagioclase-liquid hygrometer of Waters & Lange (2015). This
552 model is calibrated up to 350 MPa and down to a minimum temperature of 750 °C. Since we have
553 evidence that the CMV system extends to pressures >350 MPa, most of the CMV system is outside
554 the calibration range of the Waters & Lange (2015) model (shown as dashed curves in Fig. 10b).
555 Notably, magmatic water concentrations calculated using this model show minimal sensitivity to
556 pressure but significant sensitivity to temperature (Fig. 10b). In light of the minimal pressure
557 sensitivity, we have applied the model beyond its calibrated range, and note that the results should
558 be interpreted with caution. We considered a range of anorthite contents from An_{20} to An_{40}, a range
559 of melt compositions from dacite (corresponding to the average CMV whole rock composition) to
560 rhyolite (corresponding to the average composition of the melt inclusions), and a pressure range of
561 200 – 1000 MPa. We found that pressure exerts little influence on the results (<~0.3 wt% H_2O) so
562 we fixed the pressure to 350 MPa (the maximum pressure that the model is calibrated to) in Fig.
563 10b. If we assume a temperature of 820 °C from plagioclase-liquid thermometry (Putirka, 2008;
564 see section 4.5.3) and 866 °C from amphibole-liquid thermometry (Putirka, 2016; see section
565 4.5.2), we obtain maximum water contents between 5.1 and 6.2 wt% H_2O (Fig. 10a). To match the
566 highest measured water concentrations in CMV melt inclusions (10.7 wt% H_2O), extrapolation of
567 the Waters and Lange model suggests that lower temperatures of ~70 0 °C would be required (Fig.
568 10b; see discussion in sections 4.5.3 and 5.2).

569 ### 4.5. Pressure, temperature and melt composition

570 The high-water contents recorded by melt inclusions and plagioclase-hygrometry indicate high
571 pressures for magma crystallization and storage. Here, we present pre-eruptive magmatic pressures
572 and temperatures calculated from analyses in the core and rim of amphibole and plagioclase crystals
573 in pumice clasts. For crystals across which transects were measured, we used an average
574 composition for core and rim. We report pressure estimates using amphibole geobarometers
575 formulated by linear regression (Ridolfi, 2021), linear least-squares regression with a
576 thermodynamic basis (Putirka, 2008; Putirka, 2016), and random forest machine learning (Higgins
577 *et al.*, 2022). Results are provided in Supplementary Table D1 and Fig. 11.

578 #### *4.5.1. Amphibole-only geothermobarometry*

579 The amphibole-only geothermobarometer of Ridolfi (2021) indicates a cluster of pressures between
580 196 ± 24 and 404 ± 48 MPa for both the unzoned and zoned amphibole crystals, consistent with
581 the storage pressure of 360 ± 43 MPa obtained using this method for the 900 yr BP dome-building
582 eruption of CMV (Laeger *et al.*, 2013). A single high-pressure value of 773 ± 93 MPa was also
583 recorded by using this barometer. The high-Mg amphiboles formed at higher temperatures (916 ±
584 22 °C on average) than the more abundant low-Mg amphiboles (851 ± 22 °C on average). Normally
585 zoned amphiboles have cores formed at 899 – 923 °C mantled by rims formed at 839 – 858 °C,
586 while the compositions of the reversely zoned amphiboles reflect lower temperatures at their cores
587 (841 – 874 °C) than their rims (870 – 929 °C).

588 We applied an amphibole-only geobarometer-hygrometer from Krawczynski *et al.* (2012)
589 to our high Mg# amphiboles (Mg# 70 – 80). Our results suggest pressures from 280 MPa to 598
590 MPa with an uncertainty of ± 94 MPa. Higher pressures are found for amphibole overgrowths
591 around olivine crystals. Experiments performed by Krawczynski *et al.* (2012) suggest that the

592 coexistence of amphibole and olivine only occurs in a narrow temperature window between 915
593 and 1050 ˚C.

594 *4.5.2. Amphibole-liquid geothermobarometry*

595 We tested our amphibole-only geothermobarometry results against the amphibole-liquid
596 geothermobarometer of Putirka (2016). Equilibrium conditions between amphibole crystals and
597 whole-rock composition, average melt composition, and glass matrix were determined using the
598 $K_D = 0.28 \pm 0.11$ criterion (Putirka, 2016). The low-Mg amphibole crystals (Mg# <64) were found
599 to be in equilibrium with the average glass composition, whereas the high-Mg amphiboles (Mg# >
600 64) did not meet the criteria. Results are detailed in Supplementary Table E1. Our melt inclusion
601 data indicate that the magma was saturated with a water-rich fluid, so when applying the hydrous
602 version of the amphibole-melt barometer (equation 7a of Putirka, 2016), water concentrations were
603 increased iteratively until the maximum water able to dissolve at each pressure (i.e., water-
604 saturation) was reached. The resulting pressure estimates are higher than those obtained using the
605 Ridolfi (2021) calibration, ranging from 320 to 1040 MPa with an uncertainty of ± 200 MPa and a
606 mode of ~670 MPa. Temperature estimates are consistent with the amphibole-only
607 geothermobarometry results (Fig. 11).

608 Finally, we obtained a wide range of crystallization pressures from 200 ± 25 to 1000 ± 320
609 MPa using a machine learning approach (Higgins *et al.,* 2022) with a mode of 700, and a barometry
610 uncertainty of 250 MPa which overlaps with the results obtained by the Putirka (2016)
611 thermobarometer. The single-phase thermobarometer calibration of Higgins *et al*. (2022) uses an
612 experimental data set that was used to train regression models with the extraTrees v1.0.5 package
613 (Simm *et al.,* 2014) in R. The extraTrees package involves a classification and regression machine
614 learning approach that uses a set of independent decision trees to make a prediction output (P, T)

by analyzing input data (mineral chemistry of the selected phase). Temperatures of amphibole crystallization determined by the Higgins *et al.* (2022) thermometer are in good agreement with the Putirka (2016) and Ridolfi (2021) thermometers (Fig. 11).

There is a clear discrepancy in our amphibole barometry estimates between the Ridolfi (2021) amphibole-only barometer and the amphibole-liquid barometers of Putirka (2016) and Higgins *et al.* (2022). This discrepancy can be attributed to the experimental amphibole database used to produce the calibration equations of Ridolfi & Renzulli (2012), and updated in Ridolfi (2021). The Ridolfi database lacks data for silica-rich magmas at relatively high pressure as pointed out by Erdmann *et al.* (2014), and this may be biasing our CMV results.

Notably, additional constraints from the coexistence of olivine and high-Mg amphibole (Krawczynski *et al.*, 2012) indicate magma storage pressures higher than those obtained using the Ridolfi (2021) amphibole barometer. In light of this, we suggest that the Putirka (2016) and Higgins *et al.* (2022) amphibole-liquid barometers are likely providing more robust estimates of magma storage pressure at CMV.

4.5.3. Plagioclase-melt thermometry

We compare temperature calculations from amphibole thermometry with the plagioclase-melt thermometer of Putirka (2005, 2008) for which we supplied X_{An}, average glass composition (note that we checked for plagioclase-melt equilibrium using the equilibrium constant for albite (Ab) and anorthite (An) exchange between plagioclase (pl) and melt (liq) expressed as $K_D(An\text{-}Ab)^{pl\text{-}liq} = 0.1 \pm 0.05$ criterion), an average H_2O content (6 ± 1 wt%) estimated using the equilibrium partition coefficient 0.002 of water in plagioclase (see Table 2 and Supplementary Table E2; the uncertainties in partition coefficients in plagioclase are discussed in section 4.4) and the modal pressure of 7 00 MPa. We obtained an average temperature of 820 ± 48 °C (see Supplementary

Table D2), which is slightly lower than the temperature obtained from amphibole thermometry but still similar within uncertainty (851 ± 22 °C; obtained by Ridolfi, 2021). We obtained even lower temperatures (708 – 727 ± 48 °C) using the maximum H_2O content estimated from melt inclusions (10.7 wt%) in the pressure range 200 – 1000 MPa (extreme values obtained from the Higgins *et al*. (2022) amphibole barometry). This temperature range is consistent with the range indicated by the Waters & Lange (2015) plagioclase hygrometer (section 4.4) for the range of water concentrations measured in the melt inclusions (Fig. 10b), although we note that pressures >350 MPa and temperatures <750 °C extend beyond the calibrated range of this hygrometer.

4.5.4. Amphibole-only chemometry

To obtain information about the major element composition of the melts in equilibrium with the mineral phases present at the time of crystallization, we calculated melt composition parameters using amphibole chemometry (i.e., the application of machine learning techniques to constrain melt composition from analyses of amphibole; Higgins *et al.*, 2022). The corresponding melts calculated from the low-Mg amphiboles indicate dacitic or rhyolitic composition whereas melt composition calculated from the high-Mg population of amphiboles is suggestive of andesitic parental melts (Fig. 12).

4.5.5. Summary of thermobarometry and chemometry constraints:

- The low-Mg unzoned amphiboles (Mg# 53 – 62) in equilibrium with the average glass composition record crystallization at a temperature of ~866 ± 35 °C (Amp-liquid by Putirka, 2016) or ~851 ± 22 °C by Ridolfi (2021), and 853 ± 26 °C by Higgins *et al.* (2022; Amp-only). Plagioclase phenocrysts record similar temperatures regardless of the phenocrysts population, with an average of ~820 ± 48 °C (assuming 6 ± 1 wt% H_2O) or ~708 °C ± 48 °C (assuming 10.7 wt% H_2O).

- The small population (~5%) of high-Mg unzoned amphiboles (Mg# 61 – 77) that were not in equilibrium with the average glass composition record crystallization from a higher temperature magma (~950 ± 24 °C).
- Approximately 18% of amphiboles are normally or reversely zoned, reflecting the interaction between these high and low temperature magmas. The observed coexistence of high-Mg amphibole and olivine suggests that the primitive magma temperature was likely between 915 and 1050 ˚C (Krawczynski *et al.*, 2012).
- Amphibole chemometry indicates a predominantly dacitic magma reservoir at 700 ± 250 MPa that is supported by the remarkably homogeneous composition of CMV erupted materials, even from other eruptions (Méndez *et al.,* 2002; Laeger *et al.,* 2013) (see Fig. 5a). However, a few crystals suggest the presence of andesitic melt compositions in the shallower magma storage region (from ~220 – 470 MPa; using the Higgins *et al.,* 2022 geothermobarometer). Melt inclusions and matrix glasses preserve evidence of rhyolitic magma in the shallow storage region (<500 MPa) beneath CMV, but the andesitic melts recorded by amphibole chemometry appear to have been erased.

5. DISCUSSION

5.1. Evidence for the presence of superhydrous magma at CMV

Multiple lines of evidence point to the presence of superhydrous magma (containing >8 wt% H_2O) at CMV: (1) Direct measurements of water concentrations >8 wt% in quartz-hosted melt inclusions; (2) Measurements of high-water concentrations in plagioclase crystals; (3) co-existence of high-forsterite olivine and high-Mg# amphibole, and other equilibrium phase relationships that will be discussed in more detail below.

683 ### *5.1.1. H_2O concentrations in plagioclase- and quartz-hosted melt inclusions*

684 Of the 35 melt inclusions analyzed by FTIR, two quartz-hosted melt inclusions were found to
685 contain >8 wt% H_2O (using the Zhang *et al.,* 1997 calibration; other calibrations produce even
686 higher concentrations). NanoSIMS analyses of a subset of quartz-hosted melt inclusions indicate
687 water concentrations of up to 7.7 wt% H_2O. If 'superhydrous melt' is defined as melt containing
688 >8 wt% H_2O (e.g., Goltz *et al.,* 2020), then our FTIR results indicate that we can directly measure
689 superhydrous melt. Measurements of such high-water concentrations in melts are rare in the
690 literature (Borisova *et al*., 2006; Gavrilenko *et al.,* 2019). Several processes make it difficult to
691 preserve high-water contents in quenched melts: high-water contents reduce the quenchability of
692 silicate melts (Gavrilenko *et al.,* 2019); rapid diffusion of H in minerals and melts means that water
693 can be rapidly lost from melt inclusions by post-entrapment diffusion during magma ascent (Barth
694 *et al.,* 2023); and stability limitations on melt inclusion host minerals may bias the melt inclusion
695 record [e.g., adiabatic ascent of magma can result in resorption of crystals that formed in the deep
696 crust (Annen *et al.,* 2006), and large pressure drops during magma ascent can trigger melt inclusion
697 rupture (Borisova *et al*. 2005; Bachmann *et al.* 2010; Maclennan, 2017; Wallace *et al.,* 2021)]. For
698 these reasons, it is perhaps unsurprising that the melt inclusion record at CMV is biased towards
699 lower water concentrations; however, the presence of even two melt inclusions containing >8 wt%
700 H_2O (B1 Qz5 and d1 Qz10 in Table 1) indicates that CMV is a remarkably water-rich system.

701 ### *5.1.2. H_2O concentrations measured in plagioclase*

702 In section 4.4, we describe how water concentrations in plagioclase crystals can be used to estimate
703 the pre-eruptive water concentration of CMV magma. The lack of water gradients in the 17
704 plagioclase crystals analyzed indicates that any diffusive water loss experienced by the crystals
705 during their ascent in a degassing magma was confined to the outer ~50 μm of the crystals and was

therefore unresolvable by our FTIR measurements. We can therefore assume that the water concentrations measured in the crystal cores reflect equilibrium conditions with the pre-eruptive melt just prior to the final ascent. Assuming a square root relationship between the water in the plagioclase crystals and the water in the coexisting melt (Equation 12), the plagioclase crystals containing 103 – 161 ppm H_2O are in equilibrium with a melt containing 5 to 11 wt% H_2O, which agrees with our melt inclusions measurements (Fig. 10) and supports the presence of superhydrous melt at CMV. Notably, the wide range of water concentrations obtained for the plagioclase crystals might be related to minor crystallization as the magma ascended through the crust recording multiple depths of crystallization in a water-saturated system. The major element composition of CMV plagioclase also supports the presence of melts with relatively high-water contents. Experimental constraints show that plagioclase with An_{27-66} crystallizes close to or at water saturation (~7 wt% at ~220 MPa) within the temperature range 750 – 900 °C (Rutherford & Devine, 1996; Scaillet & Evans, 1999; Prouteau & Scaillet, 2003), which applies to shallow crystallization of the CMV system.

5.1.3. Coexistence of high-forsterite olivine and high-Mg# amphibole

Experimental phase equilibrium studies of primitive magnesian andesites and high-Mg basalts have shown that amphibole coexists with high-Mg olivine under water-saturated conditions at pressures in excess of 500 MPa, suggestive of water contents in excess of 10 wt% (Grove *et al.,* 2003; Krawczynski *et al.*, 2012). The observation of coexisting high-forsterite olivine and high-Mg# amphibole in arc magmas is regarded as a hallmark of superhydrous magmatic systems (e.g., Goltz *et al.,* 2020). High-Mg amphibole crystals are observed in CMV pumices to form overgrowths on rare olivine crystals and a single orthopyroxene crystal. The coexistence of amphibole (Mg# 73 – 80) and olivine (Mg# 89 – 92) crystals at CMV supports the presence of superhydrous magma.

729 In addition to the above lines of evidence for the presence of superhydrous magma at CMV,
730 we note that superhydrous systems have been inferred elsewhere using geophysical techniques. In
731 the South American Andes, the presence of silicic water-rich melts (> 8 wt%) in the mid-to-lower
732 crust of the Andean magmatic arc has been inferred by magnetotelluric studies which reveal a broad
733 conduction zone associated with a low-velocity region at >20 km depth (equivalent to ~700 MPa)
734 (Yuan *et al.*, 2000; Brasse *et al.*, 2002; Schilling *et al.*, 2006; Laumonier *et al.*, 2017). This
735 conduction zone in the upper mantle-lower crust region (25 – 40 km equivalent to ~800 – 1400
736 MPa) also has been observed in geophysical studies in the Bolivian Altiplano in the Central Andes,
737 the Altiplano-Puna, Southern Washington Cascades volcanic arc (USA), and the Taupo Volcanic
738 Zone (New Zealand) (Brasse *et al.*, 2002; Laumonier *et al.*, 2017). Application of such techniques
739 to the CMV region would be an interesting avenue of future research.

740 **5.2. Composition and distribution of magma in the crust beneath CMV**

741 In order to constrain storage conditions of the largest eruption of Cerro Machín volcano (event P1,
742 Rueda, 2005), we applied several petrologic thermometers, barometers and hygrometers.
743 Uncertainties from the barometry models do not provide enough support to distinguish between a
744 transcrustal reservoir or multiple discrete regions of magma through the crustal column. However,
745 given that most of the pressures from the barometry are between ~550 and ~700 MPa (25^{th} and 75^{th}
746 percentiles, respectively), we interpret that the magma reservoir is mostly located in the mid-to-
747 lower crust corresponding to depths of ~15 – 23 km, assuming a crustal density beneath CMV of
748 2,900 kg/m3 (Pedraza *et al.,* 2022). This is also supported by the presence of amphibole coexisting
749 with high-Mg olivine which indicates pressures in excess of 500 MPa. Some crystallization might
750 have occurred in the shallow crust at a depth of < ~12 km (< 500 MPa) as recorded by some
751 amphibole crystals, and by entrapment pressures calculated from melt inclusions.

Notably, seismic activity from 2000 to 2008, mainly concentrated in the main dome inside the crater, became deeper from 2009 to 2015 with up to 8500 volcano-tectonic earthquakes (VT) reported at depths between 15 and 30 km to the southeast of the crater (Londoño, 2016). These seismic events are consistent with a CMV magma reservoir at a depth that matches the range of pressures obtained by geobarometry (Fig. 13). This shift in the seismicity spatial distribution was interpreted as new magmatic activity, also supported by an increase in helium isotopic signature ($^3He/^4He$) and a decrease in log $C/^3He$ between 2011 and 2013 (Inguaggiato *et al.*, 2017).

A small population of high-Mg amphibole phenocrysts (n=4) formed at higher temperatures than the main dacitic reservoir. Amphibole chemometry indicates that these phenocrysts crystallized from andesitic melts (Fig. 12). Surprisingly, these crystals indicate pressures of <400 ± 250 MPa (Fig. 12), while the main dacitic reservoir (green-yellowish magma body in Fig. 13) was at a pressure of ~700 ± 250 MPa. This suggests that andesitic melts were intruded into the shallow-to-mid crustal storage region, bypassing the lower crustal dacite. The lower SiO_2 in this hypothetical andesite recharge magma (green-orangish magma injection in Fig. 13) may have aided the magma ascent to the mid-to-shallow crust, since silica-poor magmas are less viscous than their silica-rich counterparts (e.g., Collins *et al.*, 2020). This high-temperature melt replenishment resulted in the growth of high-Mg rims on the reversely zoned crystals. However, the low abundance of high-Mg and reversely zoned amphiboles (see Fig. 4b) implies that only a small quantity of andesitic magma was injected into the main dacitic reservoir such that it did not drastically change the average crystallization conditions, as evidenced by the rim composition of normal zoned amphibole crystals.

In addition to constraints from amphibole and plagioclase thermobarometry, we can also constrain the magmatic architecture beneath CMV using experimentally determined phase relations

obtained from volcanoes with a similar composition to CMV. The equilibrium mineral assemblage for the main CMV dacitic magma includes plagioclase (with relatively low An content), amphibole (Mg# 53 – 62), quartz and biotite phenocrysts, with accessory Fe-Ti oxides and apatite, and rare olivine (n=10) and orthopyroxene (n=1) mantled by amphibole. Normal and reverse-zoned plagioclase and amphibole crystals as well as high-Mg amphiboles indicate disequilibrium conditions in the main dacitic reservoir that may represent a magma recharge event. A literature survey of other calc-alkaline dacite systems with this equilibrium mineral assemblage [Ruapehu volcano, New Zealand (Gamble *et al.,* 1999; Conway *et al.,* 2020), Taupo, New Zealand (Conrad *et al.,* 1988), Pinatubo, Phillipines (Borisova *et al.,* 2005; Rutherford & Devine, 1996), Mt. Shasta, California (Grove, *et al.,* 2005), Trans-Mexican Volcanic Belt (Crabtree & Lange, 2011; Gómez-Tuena *et al*., 2007), Black Butte, California (McCanta *et al.,* 2007), Mt. Pelee, Lesser Antilles Arc (Pichavant *et al*., 2002)] reveals that the lack of pyroxene and the abundance of hornblende and biotite make CMV assemblage relatively rare, the most similar system being Pinatubo (Table 3). The major element composition of Pinatubo dacite is similar to CMV dacites whereas Cr, Ni, Sr and La tend to be higher in CMV dacites (Table 3) consistent with their classification as high-silica adakites (see section 5.4). In addition to its petrography, CMV is also similar to Pinatubo in terms of being water-rich (Pinatubo melt inclusions contain up to 8.79 wt% H_2O; Borisova *et al.,* 2006) and oxidized (fO_2 of Pinatubo magma is NNO+3; Rutherford & Devine, 1996).

Herein, we compare with stable phase equilibria experiments on Pinatubo and Taupo dacites to constraint P-T conditions of CMV. These experiments have been performed over a pressure range from 100 to 960 MPa, at water-saturated and undersaturated conditions (Conrad *et al.*, 1988; Rutherford & Devine, 1996; Scaillet & Evans, 1999; Prouteau & Scaillet, 2003). Results of these experiments suggest the following:

- To the extent that Pinatubo and Taupo can be considered analogous to CMV, the lack of pyroxene in CMV magma likely constrains the water content to >10.5 wt% in the deep crust. In order to avoid orthopyroxene or clinopyroxene crystallization, the melt should contain >7 wt% H_2O at 400 MPa and >~10.5 wt% H_2O at 960 MPa (Prouteau & Scaillet, 2003). Alternatively, pyroxene may be consumed in a peritectic reaction with melt and hornblende at low pressure; however, this may not apply to the CMV system, given that hornblende crystallized at a modal pressure of ~700 MPa (using the Putirka (2016) and Higgins *et al*. (2022) geothermobarometers) with no breakdown rims, suggesting that a significant portion of CMV magma was sourced from the mid-to-deep crust and was transported rapidly enough that there would not be enough time for pyroxene crystals to dissolve. [Notably, we do observe a single orthopyroxene crystal, but the high Mg# of that crystal suggests that it may be a mantle xenocryst.]
- In a water-saturated system, hornblende is the liquidus silicate phase, crystallizing at ~910 °C at 960 MPa. This is broadly consistent with our amphibole thermobarometry results that indicate the majority of amphiboles crystallized from dacitic melt at temperatures <~900 °C (Fig. 11).
- Our plagioclase-liquid thermometry results suggest that plagioclase (low An content) began crystallizing at ~815 °C at CMV (See Supplementary Table D2). Plagioclase is the first tectosilicate to crystallize, at a temperature of ~800 °C at 960 MPa (Fig. 14), at water-saturated conditions (Prouteau & Scaillet, 2003). If CMV is saturated with a water-rich fluid, as is suggested by our melt inclusion data, then plagioclase saturation at 820 °C (average temperature obtained using Putirka, 2008 thermometer, see Supplementary Table

D2) implies a plagioclase crystallization from a pressure of ~900 MPa (Prouteau & Scaillet, 2003), simultaneous with amphibole crystallization.

- Our measurements of >9 wt% H_2O in two quartz-hosted melt inclusions suggest that some quartz phenocrysts formed in the mid-to-deep crust. According to the results of Prouteau & Scaillet (2003), stabilization of quartz at ~960 MPa under water-rich and/or water-saturated conditions likely requires that some portion of the magma cooled to <750 °C in the mid-to-deep crust. This is in agreement with our water in plagioclase measurements that are consistent with temperatures of ~700 °C according to the model of Waters & Lange (2015) (see Fig. 10b), although we note that this temperature is beyond the calibrated range of that model.
- Quartz and biotite coexist over a pressure range between ~185 – 200 MPa and 1000 MPa (Conrad *et al.* 1988; Borisova *et al*., 2005; Rutherford & Devine, 1996) and temperatures <~830 °C.
- The lack of cummingtonite at CMV, unlike at Pinatubo, supports storage pressures of >300 MPa and temperatures >800 °C (Rutherford & Devine, 1996).

Assuming that CMV magma is close enough in composition to Pinatubo for the phase equilibria described above to apply, phase relations observed in CMV pumices indicate that the 3600 yr BP eruption of CMV tapped a relatively homogeneous dacite reservoir containing up to 10.7 wt% H_2O in the deep crust. Amphibole chemometry provides evidence for a small quantity of andesitic recharge magma to explain the stabilization of amphibole to ~950 °C. Overall, thermobarometry and phase equilibria constraints indicate that the CMV magmatic system is mature – the dacitic reservoir exhibits limited evidence for chemical variability or magma mixing (e.g., mafic enclaves are not observed at CMV).

5.3. Origin of superhydrous magma at CMV: Crustal control?

CMV magmas contain among the highest water concentrations ever reported for dacite and rhyolite (Fig. 15) and, as discussed in section 5.1.3, the coexistence of high-forsterite olivine and high-Mg# amphibole suggests that the primary magma was likely superhydrous and saturated with a water-rich fluid to pressures >500 MPa. A recent study by Rasmussen *et al.* (2022) found that the storage depths of Aleutian arc magmas correspond to the pressure of water saturation in the magmas, suggesting that the initial water content of magma exerts a primary control on shallow-to-mid crustal magma storage depths. In light of this, the evidence at CMV for magma saturation with a water-rich fluid to pressures >500 MPa (a higher pre-eruptive storage depth than is typical for arc magma; Popa *et al.,* 2021; Rasmussen *et al.,* 2022) suggests that the high-water content of CMV magma is likely inherited at least in part from the primary magma, rather than simply being a product of extensive fractional crystallization.

5.4. Mantle melting and the origin of the adakite signature at CMV

If the high-water concentration of CMV magma is a feature of the primary mantle melt, we must consider the mantle processes that could lead to the production of water-rich magma beneath CMV. Water concentrations of primitive magmas from volcanic arcs typically range from ~2 to ~6 wt% which has been proposed to result from a compensatory relationship between melt fraction and water in the mantle wedge (Plank *et al.,* 2013). However, experimental work suggests that under certain conditions, primary mantle-derived arc magmas may have higher water contents (>10 wt%) when separated at the top of the mantle wedge (Carmichael, 2002; Grove *et al.*, 2003; McCanta *et al.*, 2007; Grove *et al.*, 2012; Krawczynski *et al.*, 2012; Müntener *et al*., 2021). These high-water contents result from hydrous flux melting of the mantle (Kelemen, 1986; Kelemen *et al.,* 1990; Grove *et al.,* 2002, 2006). The major and trace element composition of CMV magma

indicates a geochemical signature typical of high-silica adakites (Fig. 5c and d). High-silica adakites (SiO_2 >60 wt%) are considered to form by the melting of hydrated basaltic material at a pressure high enough to stabilize garnet. Calculations by Martin *et al*. (2005) indicate that 15 to 25 % of partial melting of a typical basalt containing 100 to 200 ppm of Sr leaves a plagioclase-free residue with no more than 1100 ppm Sr, so melting of oceanic crust (basalt in eclogite facies + oceanic sediment) beneath CMV is supported by measurements of Sr <1100 ppm in the erupted materials. Moreover, low Nb in CMV dacites might be the result of residual rutile during basalt melting (Plank, 2014). Additionally, high Pb/Th (>2.2), Th/La (0.3 – 0.4) and low La/Th (<13; relative to mantle array) ratios are indicative of melted sediment and, to a lesser extent, fluids from the slab (Fig. 16a and b; Supplementary Figure B2a). The resulting slab melts might have interacted with mantle peridotite as evidenced by the high concentration of MgO (0.45 to 4 wt%), $CaO+Na_2O$ <11 wt%, Mg# 63 – 71, and Cr/Ni ratios of 0.5 – 4.5 wt% (Stern & Kilian, 1996; Rapp *et al.*, 1999; Martin *et al.,* 2005).

The low Y (<18 ppm), low Yb (<1.03 ppm), Sr/Y = 49 – 52, Dy/Yb = 2.3 – 2.4, and high La/Yb = 17 – 25 (Yb and Dy data from Laeger *et al*., 2013) may be produced by fractionation of garnet (see Supplementary Figure B2b) from water-rich magma in the deep crust or upper mantle (Rooney *et al.*, 2011; Castillo, 2012; Laeger *et al.*, 2013; Bissig *et al.,* 2017; Blatter *et al.*, 2023). Fractionation of garnet is supported by the observed depletion of HREEs (Fig. 16c). Additionally, we calculated REE "shape coefficients" (SCs) λ_1 and λ_2 in order to clarify the interplay between garnet crystallization and source compositions in generating the REE patterns. Following the model of Gao *et al.* (2023), ~1–5% fractional crystallization of garnet following 10% partial melting of the UOC source provides a good match to the CMV data (Fig. 16d). Given that garnet stability

888 increases in silicate liquids with high dissolved water contents (Alonso-Perez *et al.,* 2009), its
889 presence in the source supports water -rich conditions at CMV.

890 An alternative model to explain the generation of silicic melts in the mantle wedge is the
891 mélange diapir model. This model suggests that sediments or a 'mélange' of sediments and other
892 materials ascend in diapirs and mix with the mantle wedge prior to wedge melting (Nielsen &
893 Marschall, 2017; Parolari et al., 2021), as opposed to the classic metasomatized mantle model,
894 which supports the melting of slab materials before their interaction with the mantle wedge. A
895 corollary of the mélange diapir model is that mélange material entrained in a diapir is expected to
896 reach higher temperatures in the mantle wedge than it would at the slab surface, resulting in higher
897 expected melt fractions and potentially the generation of adakite-type, high-silica magmatism
898 (Castro & Gerya, 2008); however, we note that this model is a topic of debate, with some studies
899 arguing that it is unable to reproduce trends in the major elements, trace element ratios and
900 abundances, and isotopic compositions of typical volcanic arc magmas (e.g., Turner & Langmuir,
901 2022a; Turner & Langmuir, 2022b).

902 **5.5. Origin and composition of the primitive melt: primary dacite or high-Mg andesite?**

903 The juvenile material of Cerro Machín products has a dacitic composition containing 64 – 67 wt%
904 SiO_2, 4.42 – 4.94 wt% CaO, 2.04 – 2.10 wt% K_2O and Mg# 63 – 71. The lack of basaltic and
905 andesitic compositions in Cerro Machín tephra and the high Mg# of the dacite leads us to consider
906 whether CMV could be fed by dacitic primary magma.

907 Primary, mantle-derived dacitic melts have been hypothesized to form via multiple episodes
908 of melt-rock reaction at the slab-mantle interface between peridotite and hydrous-silicic slab partial
909 melts (Sobolev *et al.*, 2005; Straub *et al.*, 2011; Rebaza *et al.*, 2023), which produces olivine-free
910 secondary pyroxenites. The melting of secondary pyroxenite produces high-Ni primary melts

911 (because Ni is less compatible in pyroxene than in olivine) that explains the presence of high-Ni
912 olivines in some arc magmas (Hauri, 1996; Kogiso *et al.,* 2004; Sobolev *et al.*, 2005; Zellmer *et*
913 *al.,* 2015). However, the moderate Ni content of CMV olivines argues against a pyroxenite source
914 and instead indicates equilibrium with a peridotite source (Fig. 17a). Evidence for the interaction
915 of high silica slab melts with mantle peridotite was presented in section 5.4 and it is also supported
916 here by the CMV olivine compositions that were used to constrain X_{Mg} of the parental liquid based
917 on equilibrium relationships between olivine and basaltic liquid (Roeder & Emslie, 1970). Using a
918 value for $K_D(Fe–Mg)^{ol–liq}$ (Fe-Mg distribution coefficient between olivine and liquid) of 0.3
919 (Roeder & Emslie, 1970; Putirka, 2008), the measured olivine compositions of Fo_{89-92} indicates
920 that the Mg# of the primary melt ranged between 0.71 and 0.76. These values indicate equilibrium
921 conditions with at least one of the bulk dacites (Fig. 17b) suggesting the possibility of a primary
922 origin for the CMV dacites. However, when plotted on a FeO*/MgO versus SiO_2 diagram, the trend
923 outlined by the CMV dacites suggests they have fractionated from a high-Mg andesitic primary
924 melt composition (Fig. 17c). Furthermore, trace element evidence for garnet and amphibole
925 crystallization in the deep crust or upper mantle suggests that the primary melt underwent
926 significant fractional crystallization prior to its injection into the shallow-to-mid crust beneath
927 CMV. In this scenario, the idea that the CMV primary magma was a water-rich, high-Mg# andesite,
928 similar to that proposed to feed the Shasta volcanic system (e.g., Grove *et al.,* 2012; Krawczynski,
929 *et al.,* 2012), is more appropriate. This is also supported by amphibole chemometry results that
930 suggest the presence of andesitic melt beneath CMV, even though the erupted products are
931 uniformly dacitic.

932 **5.6. Triggering mechanism for the largest plinian eruption of CMV**

Commonly cited eruption triggering mechanisms include magma recharge events and 'second boiling' (in which crystallization drives an undersaturated magma to vapor saturation, thereby increasing overpressure). We consider second boiling (i.e., exsolution of volatiles induced by protracted crystallization) to be an unlikely eruption trigger at CMV because there is extensive evidence that the magma was saturated with a supercritical fluid in the mid-to-deep crust (i.e., prior to shallow-crustal crystallization). Instead, insights into the possible triggering mechanism for the 3600 yr BP eruption of Cerro Machín volcano come from the chemical diversity and textures of the crystal phases present in the eruptive products. Chemical and textural variabilities in phenocrysts from arc magmas have been proposed to be the result of reheating events caused by the injection of a hotter (recharge) magma into the main reservoir (Barclay *et al.*, 1998; Murphy *et al.*, 1998; Holtz *et al.*, 2005; Borisova *et al.,* 2014; Conway *et al.*, 2020). Possible evidence of this process at Cerro Machín include: (1) plagioclase crystals with normal and reverse zoning (Fig. 4a); (2) unzoned amphibole crystals with high and low Mg# as well as the presence of zoned crystals with low and high Mg# rims (Fig. 4b); and (3) resorbed plagioclase crystals, rounded biotites, and rounded quartz crystals that could reflect reheating by a recharge magma – although these features could also be related to latent heat produced during decompression-driven crystallization (Blundy & Cashman, 2001).

Notably, evidence for recharge (i.e., crystals with resorption textures and/or chemical zoning) is not widely present in the eruptive products of this plinian eruption, but such features were commonly observed by Laeger *et al.* (2013) in products of the ~900 yr BP dome-building eruption of Cerro Machín. The variability in eruptive styles from the same dacitic composition at CMV might be related to the volume of the magma injection events that preceded the eruptions (Ruprecht & Bachmann, 2010). Explosive eruptions are thought to be preceded by volumetrically

minor recharge events compared to effusive eruptions (~30 vol% for the 1846 – 1847 eruption of Quilatoa volcano; Ruprecht & Bachmann, 2010), as minor injections of hotter magma do not provide sufficient heat to reduce silicic magma viscosity that might enable an effusive eruption; however, they are able to destabilize the system by increasing magma overpressure and allowing conduits to open (Prouteau & Scaillet, 2003; Ruprecht & Bachmann, 2010). The small volume of magma recharge (illustrated as a red-greenish magma injection in Fig. 13) for the Cerro Machín plinian eruption is supported by the presence of relatively few crystals of amphibole with high Mg# (Fig. 4b) and the minor quantity of plagioclase with high An content or reverse zoning (Fig. 4a). The minor difference in temperature (20 °C) between the two populations of amphibole crystals (Mg# ~55 and Mg# ~77) suggests that magma mixing between two similar composition magmas with small temperature differences can drive very explosive eruptions at Cerro Machín volcano, highlighting the high hazard potential posed by this volcano. Recent work by Popa *et al.* (2021) suggested that vapor-saturated, water-rich systems (containing >~5.5 wt% H_2O) are less likely to produce highly explosive eruptions, due to the ability of the vapor to compress during recharge events, thereby reducing overpressure. Our results suggest that this is not the case for CMV, where supersaturated magma containing > 5 wt% H_2O has produced plinian eruptions at this volcano.

6. CONCLUDING REMARKS

The largest known plinian eruption of Cerro Machín volcano with a VEI of 5 (Rueda, 2005) produced a pyroclastic fall deposit that was recognized from proximal to distal areas for presenting two distinctive lithofacies (*a* and *b*). Crystals from lapilli pumice clasts from the lithofacies *b* — interpreted to represent the climactic event — were analyzed in order to unravel the pre-eruptive conditions. Evidence for a dacitic magma reservoir beneath Cerro Machín volcano at the base of the crust (reported to be <35 km in Colombia; Schaefer, 1995) to mid-upper crustal pressures is

supported by amphibole barometry, calculated saturation pressures of volatiles in melt inclusions, and mineral phase relations. Studies have suggested the presence of superhydrous magmas (> 8 wt% H_2O) beneath certain arcs (Goltz *et al.*, 2020; Laumonier *et al.*, 2017) but superhydrous melts have not been previously supported by FTIR or SIMS measurements of melt inclusions possibly due to re-equilibration processes (Plank *et al.*, 2013; Barth & Plank, 2021) or quenchability limitations (Gavrilenko *et al.*, 2019). We present direct evidence for superhydrous conditions at Cerro Machín: we measured 0.5 – 10.7 wt% H_2O in quartz- and plagioclase-hosted melt inclusions, and we measured 10 3 – 161 ppm of water in plagioclase crystals that are estimated to have crystallized in melts with 5 – 11 wt% H_2O. Superhydrous conditions are also supported by the co-existence of high-Fo olivine and amphibole (Krawczynski *et al.*, 2012).

Trace element characteristics indicate an adakite signature for CMV magmas that may have been produced by fractionation of garnet and amphibole from primitive hydrous high-Mg andesites near the Moho. Amphibole chemometry and chemical zoning patterns of amphibole and feldspar crystals suggest that a small replenishment of fresh H_2O-rich magma with an andesitic composition may have triggered magma mixing and facilitated the largest known plinian eruption of Cerro Machín volcano.

ACKNOWLEDGEMENTS

We would like to thank Dr. P. Ruprecht, Dr. M. Krawczynski and Dr. A. Borisova for providing thoughtful reviews that led to significant improvements to this manuscript. We also thank Dr. M. Reid for her helpful comments and editorial handling. We are grateful to Professor Stanley Mertzman for his help with the whole-rock analysis and for answering our questions regarding the sample preparation process. We also thank Jianhua Wang for his support during the NanoSIMS sessions. We thank Ricardo Méndez and Gloria Patricia Cortés (Colombian Geological Survey)

and Dr. Natalia Pardo (Los Andes University, Colombia) for their help and support in the planning work of the field campaigns conducted in Cerro Machín area in 2020. We are grateful to Professor Luca Caricchi for insightful conversations about amphibole thermobarometry and chemometry. We thank Professor John Stix for providing a glass standard for the FTIR measurements. We acknowledge the support of the Maryland Nanocenter and the Advanced Imaging and Microscopy Lab at the University of Maryland. Castilla acknowledges Fulbright Colombia - Pasaporte a la Ciencia scholarship for their support to contribute to the "Foco-reto país Colombia: Society" by providing new information about Cerro Machin volcano eruptive behavior, useful to hazard evaluation of the territories around the volcano. Newcombe acknowledges support from NSF grant 2237994.

DATA AVAILABILITY STATEMENT

The data underlying this article are available in EarthChem Library, at https://doi.org/10.60520/IEDA/113201. and in its online supplementary material. The sample used in this study is registered in SESAR database by the IGNS code 10.58052/IE7070001.

REFERENCES

Adam, J., Turner, M., Hauri, E. H., & Turner, S. (2016). Crystal/melt partitioning of water and other volatiles during the near-solidus melting of mantle peridotite: Comparisons with non-volatile incompatible elements and implications for the generation of intraplate magmatism. *American Mineralogist*, *101*(4), 876-888.

Alonso-Perez, R., Müntener, O., & Ulmer, P. (2009). Igneous garnet and amphibole fractionation in the roots of island arcs: experimental constraints on andesitic liquids. *Contributions to Mineralogy and Petrology*, *157*(4), 541-558.

Armstrong, J.T. (1988) Quantitative analysis of silicate and oxide materials: Comparison of Monte Carlo, ZAF and φ(ρz) procedures. In *Microbeam Analysis*, D.E. Newbury (ed.), San Francisco Press, p. 239-246.

1027 Anenburg, M., & Williams, M. J. (2022). Quantifying the tetrad effect, shape components, and
1028 Ce–Eu–Gd anomalies in rare earth element patterns. *Mathematical Geosciences*, *54*(1), 47-70.

1029 Annen, C., Blundy, J. D., & Sparks, R. S. J. (2006). The genesis of intermediate and silicic
1030 magmas in deep crustal hot zones. *Journal of Petrology*, 47(3), 505-539.

1031 Arango Palacio, E. (2012). *Morfología, petrografía y geoquímica de los domos intracratéricos*
1032 *del volcán Cerro Machín, Colombia*. [Bachelor thesis, Universidad de Caldas].

1033 Aubaud, C., Withers, A. C., Hirschmann, M. M., Guan, Y., Leshin, L. A., Mackwell, S. J., &
1034 Bell, D. R. (2007). Intercalibration of FTIR and SIMS for hydrogen measurements in glasses and
1035 nominally anhydrous minerals. *American Mineralogist*, 92(5-6), 811-828.

1036 Bacon, C. R., Newman, S., & Stolper, E. M. (1992). Water, CO_2, Cl, and F in melt inclusions in
1037 phenocrysts from three Holocene explosive eruptions, Crater Lake, Oregon. *American*
1038 *Mineralogist*, *77*(9-10), 1021-1030.

1039 Barclay, J., Rutherford, M. J., Carroll, M. R., Murphy, M. D., Devine, J. D., Gardner, J., &
1040 Sparks, R. S. J. (1998). Experimental phase equilibria constraints on pre-eruptive storage
1041 conditions of the Soufriere Hills magma. *Geophysical Research Letters*, 25(18), 3437- 3440.

1042 Barth, A., & Plank, T. (2021). The ins and outs of water in olivine-hosted melt inclusions:
1043 hygrometer vs. speedometer. *Frontiers in Earth Science*, *9*, 614004.

1044 Barth, A., Plank, T., & Towbin, H. (2023). Rates of dehydration in hydrous, high-Fo, magmatic
1045 olivines. *Geochimica et Cosmochimica Acta*, *342*, 62-73.

1046 Bachmann, O., Wallace, P. J., & Bourquin, J. (2010). The melt inclusion record from the rhyolitic
1047 Kos Plateau Tuff (Aegean Arc). *Contributions to Mineralogy and Petrology*, *159*, 187-202.

1048 Behrens, H., Romano, C., Nowak, M., Holtz, F., & Dingwell, D. B. (1996). Near-infrared
1049 spectroscopic determination of water species in glasses of the system MAlSi3O8 (M= Li, Na, K):
1050 an interlaboratory study. *Chemical Geology*, 128(1-4), 41-63.

1051 Behrens, H., Tamic, N., & Holtz, F. (2004). Determination of the molar absorption coefficient for
1052 the infrared absorption band of CO_2 in rhyolitic glasses. *American Mineralogist*, *89*(2-3), 301-
1053 306.

1054 Bissig, T., Leal-Mejía, H., Stevens, R. B., & Hart, C. J. (2017). High Sr/Y magma petrogenesis
1055 and the link to porphyry mineralization as revealed by garnet-bearing I-type granodiorite
1056 porphyries of the middle Cauca Au-Cu belt, Colombia. *Economic Geology*, *112*(3), 551-568.

Blatter, D. L., Sisson, T. W., & Hankins, W. B. (2023). Garnet stability in arc basalt, andesite, and dacite—an experimental study. *Contributions to Mineralogy and Petrology*, *178*(6), 33.

Blundy, J., & Cashman, K. (2001). Ascent-driven crystallization of dacite magmas at Mount St Helens, 1980–1986. *Contributions to Mineralogy and Petrology*, *140*, 631-650.

Borisova, A. Y., Pichavant, M., Beny, J. M., Rouer, O., & Pronost, J. (2005). Constraints on dacite magma degassing and regime of the June 15, 1991, climactic eruption of Mount Pinatubo (Philippines): new data on melt and crystal inclusions in quartz. *Journal of Volcanology and Geothermal Research*, 145(1-2), 35-67.

Borisova, A. Y., Pichavant, M., Polvé, M., Wiedenbeck, M., Freydier, R., & Candaudap, F. (2006). Trace element geochemistry of the 1991 Mt. Pinatubo silicic melts, Philippines: Implications for ore-forming potential of adakitic magmatism. *Geochimica et Cosmochimica Acta,* 70(14), 3702-3716.

Borisova, A. Y., Toutain, J. P., Dubessy, J., Pallister, J., Zwick, A., & Salvi, S. (2014). H_2O–CO_2–S fluid triggering the 1991 Mount Pinatubo climactic eruption (Philippines). *Bulletin of Volcanology*, 76, 1-9.

Bourdon, E., Eissen, J. P., Monzier, M., Robin, C., Martin, H., Cotten, J., & Hall, M. L. (2002). Adakite-like lavas from Antisana Volcano (Ecuador): evidence for slab melt metasomatism beneath Andean Northern Volcanic Zone. *Journal of Petrology*, *43*(2), 199-217.

Brasse, H., Lezaeta, P., Rath, V., Schwalenberg, K., Soyer, W., & Haak, V. (2002). The Bolivian altiplano conductivity anomaly. *Journal of Geophysical Research: Solid Earth*, 107(B5), EPM-4.

Carmichael, I. S. (2002). The andesite aqueduct: perspectives on the evolution of intermediate magmatism in west-central (105–99 W) Mexico. *Contributions to Mineralogy and Petrology*, 143(6), 641-663.

Caseres, J., Mosenfelder, J. L., & Hirschmann, M. M. (2017). Partitioning of hydrogen and fluorine between feldspar and melt under the conditions of lunar crust formation. *48th Annual Lunar and Planetary Science Conference*, 1964, 2303

Caseres, J., Mosenfelder, J. L., & Hirschmann, M. M. (2018). H_2O and F contents in Mt. Hood magmas recorded by plagioclase phenocrysts. *AGU Fall Meeting Abstracts*, 2018, V43I-0249.

Castillo, P. R. (2012). Adakite petrogenesis. *Lithos*, *134*, 304-316.

Castro, A., & Gerya, T. V. (2008). Magmatic implications of mantle wedge plumes: Experimental study. *Lithos*, 103(1-2), 138-148.

1088 Cepeda, H., Murcia, L. A., Monsalve, M. L., Méndez, R. A., & Núñez, A. (1995). Volcán Cerro
1089 Machín, Departamento del Tolima, Colombia: Pasado, Presente y Futuro. INGEOMINAS,
1090 Informe Interno.

1091 Chen, Y., Zou, C., Mastalerz, M., Hu, S., Gasaway, C., & Tao, X. (2015). Applications of micro-
1092 fourier transform infrared spectroscopy (FTIR) in the geological sciences—a review.
1093 *International Journal of Molecular Sciences*, 16(12), 30223-30250.

1094 Collins, W. J., Murphy, J. B., Johnson, T. E., & Huang, H. Q. (2020). Critical role of water in the
1095 formation of continental crust. *Nature Geoscience*, 13(5), 331-338.

1096 Colombian Geological Survey. (2023). Generalidades Volcán Cerro Machín
1097 https://www2.sgc.gov.co/sgc/volcanes/VolcanCerroMachin/Paginas/generalidades-volcan-
1098 cerromachin.aspx#:~:text=Est%C3%A1%20conformado%20por%20un%20edificio,m%20y%20
1099 150%20m%20de%20altura (accessed 8 August 2023).

1100 Conrad, W. K., Nicholls, I. A., & Wall, V. J. (1988). Water-saturated and-undersaturated melting
1101 of metaluminous and peraluminous crustal compositions at 10 kb: evidence for the origin of
1102 silicic magmas in the Taupo Volcanic Zone, New Zealand, and other occurrences. *Journal of*
1103 *Petrology*, 29(4), 765-803.

1104 Conway, C. E., Chamberlain, K. J., Harigane, Y., Morgan, D. J., & Wilson, C. J. (2020). Rapid
1105 assembly of high-Mg andesites and dacites by magma mixing at a continental arc stratovolcano.
1106 *Geology*, 48(10), 1033-1037.

1107 Coogan, L. A., Saunders, A. D., & Wilson, R. N. (2014). Aluminum-in-olivine thermometry of
1108 primitive basalts: Evidence of an anomalously hot mantle source for large igneous provinces.
1109 *Chemical Geology*, 368, 1-10.

1110 Crabtree, S. M., & Lange, R. A. (2011). Complex phenocryst textures and zoning patterns in
1111 andesites and dacites: evidence of degassing-induced rapid crystallization?. *Journal of Petrology*,
1112 *52*(1), 3-38.

1113 Davidson, J., Turner, S., Handley, H., Macpherson, C., & Dosseto, A. (2007). Amphibole
1114 "sponge" in arc crust?. *Geology*, 35(9), 787-790.

1115 Defant, M. J., & Drummond, M. S. (1990). Derivation of some modern arc magmas by melting of
1116 young subducted lithosphere. *Nature*, *347*(6294), 662-665.

1117 Dixon, J. E., Stolper, E. M., & Holloway, J. R. (1995). An experimental study of water and
1118 carbon dioxide solubilities in mid-ocean ridge basaltic liquids. Part I: calibration and solubility
1119 models. *Journal of Petrology*, *36*(6), 1607-1631.

Drummond, M. S., Defant, M. J., & Kepezhinskas, P. K. (1996). Petrogenesis of slab-derived trondhjemite–tonalite–dacite/adakite magmas. *Earth and Environmental Science Transactions of the Royal Society of Edinburgh*, *87*(1-2), 205-215.

Erdmann, S., Martel, C., Pichavant, M., & Kushnir, A. (2014). Amphibole as an archivist of magmatic crystallization conditions: problems, potential, and implications for inferring magma storage prior to the paroxysmal 2010 eruption of Mount Merapi, Indonesia. *Contributions to Mineralogy and Petrology*, *167*, 1-23.

Fischer, T. P., & Marty, B. (2005). Volatile abundances in the sub-arc mantle: insights from volcanic and hydrothermal gas discharges. *Journal of Volcanology and Geothermal Research*, 140(1-3), 205-216.

Gamble, J. A., Wood, C. P., Price, R. C., Smith, I. E. M., Stewart, R. B., & Waight, T. (1999). A fifty year perspective of magmatic evolution on Ruapehu Volcano, New Zealand: verification of open system behaviour in an arc volcano. *Earth and Planetary Science Letters*, 170(3), 301-314.

Gao, Y., O'Neill, H. S. C., & Mavrogenes, J. A. (2023). Garnet versus amphibole: Implications for magmatic differentiation and slab melting. *Geology*. *52*(2), 125-129.

Gavrilenko, M., Krawczynski, M., Ruprecht, P., Li, W., & Catalano, J. G. (2019). The quench control of water estimates in convergent margin magmas. *American Mineralogist*, *104*(7), 936-948.

Goltz, A. E., Krawczynski, M. J., Gavrilenko, M., Gorbach, N. V, & Ruprecht, P. (2020). Evidence for superhydrous primitive arc magmas from mafic enclaves at Shiveluch volcano, Kamchatka. *Contributions to Mineralogy and Petrology*, 175(12), 1–26.

Gómez, D., López, C., Monsalve, M. L., Agudelo, A., Cortés Jímenez, G. P., Calvache, M. C. (2021). Active volcanism in Colombia and the role of the Servicio Geológico Colombiano. *Volcanica* 4.S1: 113-139.

Gómez-Tuena, A., Orozco-Esquivel, M. T., & Ferrari, L. (2007). Igneous petrogenesis of the Transmexican Volcanic Belt. *Boletín de la Sociedad Geológica Mexicana*, 57(3), 227-283.

Grove, T. L., Baker, M. B., Price, R. C., Parman, S. W., Elkins-Tanton, L. T., Chatterjee, N., & Müntener, O. (2005). Magnesian andesite and dacite lavas from Mt. Shasta, northern California: products of fractional crystallization of H_2O-rich mantle melts. *Contributions to Mineralogy and Petrology*, 148(5), 542-565.

Grove, T. L., Chatterjee, N., Parman, S. W., & MÚdard, E. (2006). The influence of H_2O on mantle wedge melting. *Earth and Planetary Science Letters*, *249*(1-2), 74-89.

1152 Grove, T. L., Elkins-Tanton, L. T., Parman, S. W., Chatterjee, N., Müntener, O., & Gaetani, G. A.
1153 (2003). Fractional crystallization and mantle-melting controls on calc-alkaline differentiation
1154 trends. *Contributions to Mineralogy and Petrology*, 145(5), 515-533.

1155 Grove, T. L., Till, C. B., & Krawczynski, M. J. (2012). The role of H_2O in subduction zone
1156 magmatism. *Annual Review of Earth and Planetary Sciences*, *40*, 413-439.

1157 Grove, T., Parman, S., Bowring, S., Price, R., & Baker, M. (2002). The role of an H_2O-rich fluid
1158 component in the generation of primitive basaltic andesites and andesites from the Mt. Shasta
1159 region, N California. *Contributions to Mineralogy and Petrology*, 142(4), 375- 396.

1160 Hamada, M., Kawamoto, T., Takahashi, E., & Fujii, T. (2011). Polybaric degassing of island arc
1161 low-K tholeiitic basalt magma recorded by OH concentrations in Ca-rich plagioclase. *Earth and*
1162 *Planetary Science Letters*, *308*(1-2), 259-266.

1163 Hamada, M., Ushioda, M., Fujii, T., & Takahashi, E. (2013). Hydrogen concentration in
1164 plagioclase as a hygrometer of arc basaltic melts: Approaches from melt inclusion analyses and
1165 hydrous melting experiments. *Earth and Planetary Science Letters*, *365*, 253-262.

1166 Hartley, M. E., Maclennan, J., Edmonds, M., & Thordarson, T. (2014). Reconstructing the deep
1167 CO_2 degassing behavior of large basaltic fissure eruptions. *Earth and Planetary Science Letters*,
1168 *393*, 120-131.

1169 Hauri, E. H. (1996). Major-element variability in the Hawaiian mantle plume. *Nature*, *382*(6590),
1170 415-419.

1171 Hauri, E., Wang, J., Dixon, J. E., King, P. L., Mandeville, C., & Newman, S. (2002). SIMS
1172 analysis of volatiles in silicate glasses: 1. Calibration, matrix effects and comparisons with FTIR.
1173 *Chemical Geology,* 183(1-4), 99-114.

1174 Higgins, O., Sheldrake, T., & Caricchi, L. (2022). Machine learning thermobarometry and
1175 chemometry using amphibole and clinopyroxene: a window into the roots of an arc volcano
1176 (Mount Liamuiga, Saint Kitts). *Contributions to Mineralogy and Petrology*, *177*(1), 10.

1177 Holtz, F., Sato, H., Lewis, J., Behrens, H., & Nakada, S. (2005). Experimental petrology of the
1178 1991–1995 Unzen dacite, Japan. Part I: phase relations, phase composition and pre-eruptive
1179 conditions. *Journal of Petrology*, 46(2), 319-337.

1180 Ihinger P.D. Zhang Y. Stolper E.M. (1999) The speciation of dissolved water in rhyolitic melt.
1181 *Geochimica et Cosmochimica Acta*, 63, 3567–3578.

Inguaggiato, S., Londoño, J. M., Chacón, Z., Liotta, M., Gil, E., & Alzate, D. (2017). The hydrothermal system of Cerro Machín volcano (Colombia): New magmatic signals observed during 2011–2013. *Chemical Geology*, 469, 60–68.

Johnson, E. A. (2005). Magmatic water contents recorded by hydroxyl concentrations in plagioclase phenocrysts from Mount St. Helens, 1980-1981. *Geochimica et Cosmochimica* Acta Supplement, 69(10), A743.

Johnson, E. A., & Rossman, G. R. (2004). A survey of hydrous species and concentrations in igneous feldspars. *American Mineralogist*, *89*(4), 586-600.

Johnson, E. A., & Rossman, G. R. (2013). The diffusion behavior of hydrogen in plagioclase feldspar at 800–1000 C: Implications for re-equilibration of hydroxyl in volcanic phenocrysts. *American Mineralogist*, *98*(10), 1779-1787.

Kelemen, P. B. (1986). Assimilation of ultramafic rock in subduction-related magmatic arcs. *The Journal of Geology*, 94(6), 829-843.

Kelemen, P. B., Hanghøj, K., & Greene, A. R. (2003). One view of the geochemistry of subduction-related magmatic arcs, with an emphasis on primitive andesite and lower crust. *Treatise on Geochemistry*, *3*, 659.

Kelemen, P. B., Johnson, K. T. M., Kinzler, R. J., & Irving, A. J. (1990). High-field-strength element depletions in arc basalts due to mantle–magma interaction. *Nature*, 345(6275), 521-524

Kelley, K. A., & Cottrell, E. (2009). Water and the oxidation state of subduction zone magmas. *Science*, *325*(5940), 605-607.

Keppler, H., & Bolfan-Casanova, N. (2006). Thermodynamics of water solubility and partitioning. *Reviews in Mineralogy and Geochemistry*, *62*(1), 193-230.

Kogiso, T., Hirschmann, M. M., & Pertermann, M. (2004). High-pressure partial melting of mafic lithologies in the mantle. *Journal of Petrology*, *45*(12), 2407-2422.

Kohlstedt, D. L., & Mackwell, S. J. (1998). Diffusion of hydrogen and intrinsic point defects in olivine. *Zeitschrift für physikalische Chemie*, *207*(1-2), 147-162.

Krawczynski, M. J., Grove, T. L., & Behrens, H. (2012). Amphibole stability in primitive arc magmas: effects of temperature, H_2O content, and oxygen fugacity. *Contributions to Mineralogy and Petrology*, 164(2), 317–339.

Kress, V. C., & Carmichael, I. S. (1991). The compressibility of silicate liquids containing Fe 2 O 3 and the effect of composition, temperature, oxygen fugacity and pressure on their redox states. *Contributions to Mineralogy and Petrology*, *108*, 82-92.

Laeger, K., Halama, R., Hansteen, T., Savov, I. P., Murcia, H., Cortés, G. P., & GarbeSchönberg, D. (2013). Crystallization conditions and petrogenesis of the lava dome from the~ 900 years BP eruption of Cerro Machín Volcano, Colombia. *Journal of South American Earth Sciences*, 48, 193–208.

Laumonier, M., Gaillard, F., Muir, D., Blundy, J., & Unsworth, M. (2017). Giant magmatic water reservoirs at mid-crustal depth inferred from electrical conductivity and the growth of the continental crust. *Earth and Planetary Science Letters*, 457, 173–180.

Le Bas, M. J., Le Maitre, R. W., Streckeisen, A., & Zanettin, B. (1986). A chemical classification of volcanic rocks based on the total alkali – silica diagram. *Journal of Petrology*, 27(3), 745–750.

Leake, B. E., Woolley, A. R., Arps, C. E., Birch, W. D., Gilbert, M. C., Grice, J. D., Hawthorne, F. C., Kato, A., Kisch, H. J., Krivovichev, V. G., Linthout, K., Laird, J., Mandarino, J., Maresch, W. V., Nickel, E. H., Schumaker, J. C., Smith, D. C., Stephenson, N. C. N., Ungaretti, L., Whittaker, E. J. W., & Youzhi, G. (1997). Nomenclature of amphiboles; report of the subcommittee on amphiboles of the International Mineralogical Association, Commission on New Minerals and Mineral Names. *The Canadian Mineralogist*, *35*(1), 219-246.

Li, X., Zhang, C., Behrens, H., & Holtz, F. (2020). Calculating amphibole formula from electron microprobe analysis data using a machine learning method based on principal components regression. *Lithos*, *362*, 105469.

Lin, Y. H., Hui, H., Li, Y., Xu, Y., & Van Westrenen, W. (2019). A lunar hygrometer based on plagioclase-melt partitioning of water. *Geochemical Perspectives Letters*, *10*, 14-19.

Lloyd, A. S., Plank, T., Ruprecht, P., Hauri, E. H., & Rose, W. I. (2013). Volatile loss from melt inclusions in pyroclasts of differing sizes. *Contributions to Mineralogy and Petrology*, 165(1), 129–153.

Londoño, J. M. (2016). Evidence of recent deep magmatic activity at Cerro Bravo-Cerro Machín volcanic complex, central Colombia. Implications for future volcanic activity at Nevado del Ruiz, Cerro Machín and other volcanoes. *Journal of Volcanology and Geothermal Research*, 324, 156–168.

Lu, Y. J., Loucks, R. R., Fiorentini, M. L., Yang, Z. M., & Hou, Z. Q. (2015). Fluid flux melting generated postcollisional high Sr/Y copper ore–forming water-rich magmas in Tibet. *Geology*, 43(7), 583-586.

Maclennan, J. (2017). Bubble formation and decrepitation control the CO_2 content of olivine-hosted melt inclusions. *Geochemistry, Geophysics, Geosystems*, *18*(2), 597-616.

Martin, H., Smithies, R. H., Rapp, R., Moyen, J. F., & Champion, D. (2005). An overview of adakite, tonalite–trondhjemite–granodiorite (TTG), and sanukitoid: relationships and some implications for crustal evolution. *Lithos*, *79*(1-2), 1-24.

McCanta, M. C., Rutherford, M. J., & Hammer, J. E. (2007). Pre-eruptive and syn-eruptive conditions in the Black Butte, California dacite: Insight into crystallization kinetics in a silicic magma system. *Journal of Volcanology and Geothermal Research*, 160(3–4), 263– 284.

Méndez, R. A., Cortés, G. P., & Cepeda, H. (2002). Catálogo de las unidades litoestratigráficas de Colombia: Formación Machí n. In Memoria explicativa INGEOMINAS (p. 10).

Mitchell, A. L., Gaetani, G. A., O'leary, J. A., & Hauri, E. H. (2017). H_2O solubility in basalt at upper mantle conditions. *Contributions to Mineralogy and Petrology*, 172, 1-16.

Miyashiro, A. (1974). Volcanic rock series in island arcs and active continental margins. *American Journal of Science*, *274*(4), 321-355.

Moore, G., & Carmichael, I. S. E. (1998). The hydrous phase equilibria (to 3 kbar) of an andesite and basaltic andesite from western Mexico: constraints on water content and conditions of phenocryst growth. *Contributions to Mineralogy and Petrology*, *130*(3), 304-319.

Moore, L. R., Gazel, E., Tuohy, R., Lloyd, A. S., Esposito, R., Steele-MacInnis, M.,... & Bodnar, R. J. (2015). Bubbles matter: An assessment of the contribution of vapor bubbles to melt inclusion volatile budgets. *American Mineralogist*, *100*(4), 806-823.

Morgan G., B., London, D. (1996). Optimizing the electron microprobe analysis of hydrous alkali aluminosilicate glasses. *American Mineralogist*, 81 (9-10): 1176–1185. doi: https://doi.org/10.2138/am-1996-9-1016

Mosenfelder, J. L., Andrys, J. L., von der Handt, A., Kohlstedt, D. L., & Hirschmann, M. M. (2020). Hydrogen incorporation in plagioclase. *Geochimica et Cosmochimica Acta*, *277*, 87-110.

Mosenfelder, J. L., Caseres, J. R., Andrys, J., Wright, H. M. N., & Hirschmann, M. M. (2018). Trace H and F Concentrations in Feldspar as Monitors of Volatile Processes in the Earth and Moon. In *AGU Fall Meeting Abstracts* (Vol. 2018, pp. MR23B-0085).

Mosenfelder, J. L., Rossman, G. R., & Johnson, E. A. (2015). Hydrous species in feldspars: A reassessment based on FTIR and SIMS. *American Mineralogist*, *100*(5-6), 1209-1221.

Mosquera, D., Núñez, A., & Vesga, C. (1982). Mapa Geologico de la plancha 244-Ibague. Escala 100.000. Revista Ingeominas.

Moyen, J. F. (2009). High Sr/Y and La/Yb ratios: the meaning of the "adakitic signature". *Lithos*, *112*(3-4), 556-574.

Müntener, O., Ulmer, P., & Blundy, J. D. (2021). Superhydrous arc magmas in the Alpine context. *Elements*, 17(1), 35-40.

Murcia, H., Hurtado, B., Cortés, G. P., Macías, J. L., & Cepeda, H. (2008). The ~2500 yr B.P. Chicoral non-cohesive debris flow from Cerro Machín Volcano, Colombia. *Journal of Volcanology and Geothermal Research*, 171(3), 201–214.

Murphy, M. D., Sparks, R. S. J., Barclay, J., Carroll, M. R., Lejeune, A. M., Brewer, T. S., Macdonald, R., Black, S., & Young, S. (1998). The role of magma mixing in triggering the current eruption at the Soufriere Hills volcano, Montserrat, West Indies. *Geophysical Research Letters*, 25(18), 3433-3436.

Myers, M. L., Wallace, P. J., & Wilson, C. J. (2019). Inferring magma ascent timescales and reconstructing conduit processes in explosive rhyolitic eruptions using diffusive losses of hydrogen from melt inclusions. *Journal of Volcanology and Geothermal Research*, *369*, 95-112.

Newcombe, M. E., Plank, T., Barth, A., Asimow, P. D., & Hauri, E. (2020). Water-in-olivine magma ascent chronometry: Every crystal is a clock. *Journal of Volcanology and Geothermal Research*, *398*, 106872.

Newcombe, M. E., Brett, A., Beckett, J. R., Baker, M. B., Newman, S., Guan, Y., Eiler, J. M., & Stolper, E. M. (2017). Solubility of water in lunar basalt at low pH_2O. *Geochimica et Cosmochimica Acta*, *200*, 330-352.

Newcombe, M.E. (2022). SIMSblank. https://doi.org/10.5281/zenodo.7093278.

Newman, S., & Chesner, C. (1989). Volatile compositions of glass inclusions from the 75Ka Toba Tuff, Sumatra. *Geological Society of America, Abstracts with Programs 21, 271.*

Newman, S., & Lowenstern, J. B. (2002). VolatileCalc: a silicate melt–H_2O–CO_2 solution model written in Visual Basic for excel. *Computers & Geosciences*, *28*(5), 597-604.

Newman, S., Stolper, E. M., & Epstein, S. (1986). Measurement of water in rhyolitic glasses; calibration of an infrared spectroscopic technique. *American Mineralogist*, *71*(11-12), 1527-1541.

Nielsen, S. G., & Marschall, H. R. (2017). Geochemical evidence for mélange melting in global arcs. *Science advances*, 3(4), e1602402.

Nishimura, K., Kawamoto, T., Kobayashi, T., Sugimoto, T., & Yamashita, S. (2005). Melt inclusion analysis of the Unzen 1991–1995 dacite: implications for crystallization processes of dacite magma. *Bulletin of Volcanology*, *67*, 648-662.

Ohlhorst, S., Behrens, H., & Holtz, F. (2001). Compositional dependence of molar absorptivities of near-infrared OH-and H_2O bands in rhyolitic to basaltic glasses. *Chemical Geology*, *174*(1-3), 5-20.

Paladio-Melosantos, M. L. O., Solidum, R. U., Scott, W. E., Quiambao, R. B., Umbal, J. V., Rodolfo, K. S., Tubianosa, B. S., Delos Reyes, P. J., Alonsa, R. A., & Ruelo, H. B. (1996). Tephra falls of the 1991 eruptions of Mount Pinatubo. In: Newhall, C. G. & Punongbayan, R. S. (eds) *Fire and Mud. Eruptions and Lahars of Mount Pinatubo, Philippines.* Seattle: University of Washington Press, pp. 513-535.

Papale, P., Moretti, R., & Barbato, D. (2006). The compositional dependence of the saturation surface of H_2O+ CO_2 fluids in silicate melts. *Chemical Geology*, *229*(1-3), 78-95.

Parolari, M., Gómez-Tuena, A., Errázuriz-Henao, C., & Cavazos-Tovar, J. G. (2021). Orogenic andesites and their link to the continental rock cycle. *Lithos*, 382, 105958.

Pedraza, N. F., Velazquez, J. D., Molina, I., & Pedraza, A. (2022). Gravity Studies at Cerro Machín Volcano, Colombia. *Boletín Geológico*, 49(1), 55-65.

Peterson, L. D., Newcombe, M. E., Alexander, C. M. D., Wang, J., Sarafian, A. R., Bischoff, A., & Nielsen, S. G. (2023). The H_2O content of the ureilite parent body. *Geochimica et Cosmochimica* Acta, 340, 141-157.

Pichavant, M., Martel, C., Bourdier, J. L., & Scaillet, B. (2002). Physical conditions, structure, and dynamics of a zoned magma chamber: Mount Pelée (Martinique, Lesser Antilles Arc). *Journal of Geophysical Research: Solid Earth*, *107*(B5), ECV-1.

Plank, T. (2014) The chemical composition of subducting sediments. In: Holland H. D. & Turekian K. K. (eds) *Treatise on Geochemistry*, 2nd ed. Elsevier, pp.607–629.

Plank, T., Kelley, K. A., Zimmer, M. M., Hauri, E. H., & Wallace, P. J. (2013). Why do mafic arc magmas contain~ 4 wt% water on average?. *Earth and Planetary Science Letters*, *364*, 168-179.

Popa, R. G., Bachmann, O., & Huber, C. (2021). Explosive or effusive style of volcanic eruption determined by magma storage conditions. *Nature Geoscience*, 14(10), 781-786.

Prouteau, G., & Scaillet, B. (2003). Experimental constraints on the origin of the 1991 Pinatubo dacite. *Journal of Petrology*, 44(12), 2203-2241.

Putirka, K. (2016). Amphibole thermometers and barometers for igneous systems and some implications for eruption mechanisms of felsic magmas at arc volcanoes. *American Mineralogist*, *101*(4), 841-858.

Putirka, K. D. (2005). Igneous thermometers and barometers based on plagioclase+ liquid equilibria: Tests of some existing models and new calibrations. *American Mineralogist*, *90*(2-3), 336-346.

Putirka, K. D. (2008). Thermometers and barometers for volcanic systems. *Reviews in Mineralogy and Geochemistry*, *69*(1), 61-120.

Rapp, R. P., Shimizu, N., Norman, M. D., & Applegate, G. S. (1999). Reaction between slab-derived melts and peridotite in the mantle wedge: experimental constraints at 3.8 GPa. *Chemical Geology*, *160*(4), 335-356.

Rappoccio, R., Johnson, E. A., Myers, M., Wallace, P. J., & Wilson, C. J. N. (2020). Hydroxyl in Quartz and Feldspar Phenocrysts from the Bishop Tuff, CA, and the Huckleberry Ridge Tuff, Yellowstone. *AGU Fall Meeting Abstracts*, 2020, V003-0005.

Rasmussen, D. J., Plank, T. A., Roman, D. C., & Zimmer, M. M. (2022). Magmatic water content controls the pre-eruptive depth of arc magmas. *Science*, *375*(6585), 1169-1172.

Rasmussen, D. J., Plank, T. A., Wallace, P. J., Newcombe, M. E., & Lowenstern, J. B. (2020). Vapor-bubble growth in olivine-hosted melt inclusions. *American Mineralogist*, *105*(12), 1898-1919.

Rebaza, A. M., Mallik, A., & Straub, S. M. (2023). Multiple episodes of rock-melt reaction at the slab-mantle interface: Formation of high silica primary magmas in intermediate to hot subduction zones. *Journal of Petrology*, *64*(3), egad011.

Régnier, A. (2015). *Cerro Machín, Colombia: A highly explosive volcano showing signs of unrest*. [Master Thesis, Université de Genève].

Richards, J. P., & Kerrich, R. (2007). Special paper: adakite-like rocks: their diverse origins and questionable role in metallogenesis. *Economic Geology*, *102*(4), 537-576.

Ridolfi, F. (2021). Amp-TB2: an updated model for calcic amphibole thermobarometry. *Minerals*, *11*(3), 324.

Ridolfi, F., & Renzulli, A. (2012). Calcic amphiboles in calc-alkaline and alkaline magmas: thermobarometric and chemometric empirical equations valid up to 1,130° C and 2.2 GPa. *Contributions to Mineralogy and Petrology*, 163(5), 877–895.

Ridolfi, F., Renzulli, A., & Puerini, M. (2010). Stability and chemical equilibrium of amphibole in calc-alkaline magmas: an overview, new thermobarometric formulations and application to subduction-related volcanoes. *Contributions to Mineralogy and Petrology*, 160(1), 45–66.

Roeder, P. L., & Emslie, R. (1970). Olivine-liquid equilibrium. *Contributions to Mineralogy and Petrology*, *29*(4), 275-289.

Roman, D. C., Cashman, K. V., Gardner, C. A., Wallace, P. J., & Donovan, J. J. (2006). Storage and interaction of compositionally heterogeneous magmas from the 1986 eruption of Augustine Volcano, Alaska. *Bulletin of Volcanology*, *68*, 240-254.

Rooney, T. O., Franceschi, P., & Hall, C. M. (2011). Water-saturated magmas in the Panama Canal region: a precursor to adakite-like magma generation?. *Contributions to Mineralogy and Petrology*, *161*, 373-388.

Rosi, M., Paladio-Melosantos, M., Di Muro, A., Leoni, R., & Bacolcol, T. (2001). Fall vs flow activity during the 1991 climactic eruption of Pinatubo Volcano (Philippines). *Bulletin of Volcanology*, 62, 549-566.

Rossman, G. R. (1996). Studies of OH in nominally anhydrous minerals. *Physics and Chemistry of Minerals*, *23*(4-5), 299-304.

Rueda, H. (2005). *Erupciones Plinianas del Holoceno en el Volcán Cerro Machín, Colombia. Estratigrafía, petrografía y dinámica eruptiva*. [MSc Thesis. Universidad Nacional Autónoma de México] México

Ruprecht, P., & Bachmann, O. (2010). Pre-eruptive reheating during magma mixing at Quizapu volcano and the implications for the explosiveness of silicic arc volcanoes. *Geology*, *38*(10), 919-922.

Ruprecht, P., & Plank, T. (2013). Feeding andesitic eruptions with a high-speed connection from the mantle. *Nature*, *500*(7460), 68-72.

Rutherford, M. J., & Devine, J. D. (1996). Pre-eruption pressure-temperature conditions and volatiles in the 1991 dacitic magma of Mount Pinatubo. In: Newhall, C. G. & Punongbayan, R. S. (eds) *Fire and Mud. Eruptions and Lahars of Mount Pinatubo, Philippines.* Seattle: University of Washington Press, pp. 751–766.

Rutherford, M. J., & Hill, P. M. (1993). Magma ascent rates from amphibole breakdown: an experimental study applied to the 1980–1986 Mount St. Helens eruptions. *Journal of Geophysical Research: Solid Earth*, *98*(B11), 19667-19685.

Saito, G., Kazahaya, K., Shinohara, H., Stimac, J., & Kawanabe, Y. (2001). Variation of volatile concentration in a magma system of Satsuma-Iwojima volcano deduced from melt inclusion analyses. *Journal of Volcanology and Geothermal Research*, *108*(1-4), 11-31.

Samaniego, P., Martin, H., Monzier, M., Robin, C., Fornari, M., Eissen, J. P., & Cotten, J. (2005). Temporal evolution of magmatism in the Northern Volcanic Zone of the Andes: the geology and petrology of Cayambe Volcanic Complex (Ecuador). *Journal of Petrology*, 46(11), 2225-2252.

Scaillet, B., & Evans, B. W. (1999). The 15 June 1991 eruption of Mount Pinatubo. I. Phase equilibria and pre-eruption P–T–f O_2–f H_2O conditions of the dacite magma. *Journal of Petrology*, *40*(3), 381-411.

Schaefer, S. J. (1995). *Nevado del Ruiz volcano, Colombia: magmatic system and evolution.* [Doctoral dissertation, Arizona State University].

Schilling, F. R., Trumbull, R. B., Brasse, H., Haberland, C., Asch, G., Bruhn, D.,... & Vietor, T. (2006). Partial melting in the Central Andean crust: a review of geophysical, petrophysical, and petrologic evidence. *The Andes*, 459-474.

Schmidt, M. W., & Jagoutz, O. (2017). The global systematics of primitive arc melts. *Geochemistry, Geophysics, Geosystems*, 18(8), 2817-2854.

Schmitt, A. K. (2001). Gas-saturated crystallization and degassing in large-volume, crystal-rich dacitic magmas from the Altiplano-Puna, northern Chile. *Journal of Geophysical Research: Solid Earth*, *106*(B12), 30561-30578.

Seaman, S. J., Dyar, M. D., Marinkovic, N., & Dunbar, N. W. (2006). An FTIR study of hydrogen in anorthoclase and associated melt inclusions. *American Mineralogist*, *91*(1), 12-20.

Shimizu, K., Ushikubo, T., Kuritani, T., Hirano, N., & Yamashita, S. (2022). Modification for the matrix effect in SIMS-derived water contents of silicate glasses. *Geochemical Journal*, 56(6), 223-230.

Simm, J., De Abril, I. M., & Sugiyama, M. (2014). Tree-based ensemble multi-task learning method for classification and regression. *IEICE TRANSACTIONS on Information and Systems*, *97*(6), 1677-1681.

Sisson, T. W., & Grove, T. L. (1993). Experimental investigations of the role of H_2O in calc-alkaline differentiation and subduction zone magmatism. *Contributions to Mineralogy and Petrology*, *113*, 143-166.

Skirius, C. M. (1990). *Pre-eruptive H_2O and CO_2 content of plinian and ash-flow Bishop Tuff magma.* [Doctoral dissertation, University of Chicago].

Sobolev, A. V., Hofmann, A. W., Sobolev, S. V., & Nikogosian, I. K. (2005). An olivine-free mantle source of Hawaiian shield basalts. *Nature*, *434*(7033), 590-597.

Steele-MacInnis, M., Esposito, R., Moore, L. R., & Hartley, M. E. (2017). Heterogeneously entrapped, vapor-rich melt inclusions record pre-eruptive magmatic volatile contents. *Contributions to Mineralogy and Petrology*, *172*, 1-13.

Stolper, E. (1982). The speciation of water in silicate melts. *Geochimica et Cosmochimica Acta*, *46*(12), 2609-2620.

Stern, C. R., & Kilian, R. (1996). Role of the subducted slab, mantle wedge and continental crust in the generation of adakites from the Andean Austral Volcanic Zone. *Contributions to Mineralogy and Petrology*, *123*, 263-281.

Straub, S. M., Gomez-Tuena, A., Stuart, F. M., Zellmer, G. F., Espinasa-Perena, R., Cai, Y., & Iizuka, Y. (2011). Formation of hybrid arc andesites beneath thick continental crust. *Earth and Planetary Science Letters*, *303*(3-4), 337-347.

Straub, S. M., Zellmer, G. F., Gómez-Tuena, A., Espinasa-Pereña, R., Martin-del Pozzo, A. L., Stuart, F. M., & Langmuir, C. H. (2014). A genetic link between silicic slab components and calc-alkaline arc volcanism in central Mexico. *Geological Society, London, Special Publications*, *385*(1), 31-64.

Sun, S. S., & McDonough, W. F. (1989). Chemical and isotopic systematics of oceanic basalts: implications for mantle composition and processes. *Geological Society, London, Special Publications*, *42*(1), 313-345.

Tollan, P., Ellis, B., Troch, J., & Neukampf, J. (2019). Assessing magmatic volatile equilibria through FTIR spectroscopy of unexposed melt inclusions and their host quartz: a new technique and application to the Mesa Falls Tuff, Yellowstone. *Contributions to Mineralogy and Petrology*, *174*, 1-19.

Towbin, H. W., Plank, T., Klein, E., & Hauri, E. (2023). Measuring H_2O concentrations in olivine by secondary ion mass spectrometry: Challenges and paths forward. *American Mineralogist*, *108*(5), 928-940.

Turner, S. J., & Langmuir, C. H. (2022a). An evaluation of five models of arc volcanism. *Journal of Petrology*, 63(3), egac010.

Turner, S. J., & Langmuir, C. H. (2022b). Sediment and ocean crust both melt at subduction zones. *Earth and Planetary Science Letters*, 584, 117424.

Urann, B. M., Le Roux, V., Jagoutz, O., Müntener, O., Behn, M. D., & Chin, E. J. (2022). High water content of arc magmas recorded in cumulates from subduction zone lower crust. *Nature Geoscience*, 1-8.

Von Aulock, F. W., Kennedy, B. M., Schipper, C. I., Castro, J. M., Martin, D. E., Oze, C., Watkins, J. M., Wallace, P. J., Puskar, L., Bégué, F., Nichols, A. R. L. & Tuffen, H. (2014). Advances in Fourier transform infrared spectroscopy of natural glasses: From sample preparation to data analysis. *Lithos*, 206, 52-64.

Wade, J. A., Plank, T., Melson, W. G., Soto, G. J., & Hauri, E. H. (2006). The volatile content of magmas from Arenal volcano, Costa Rica. *Journal of Volcanology and Geothermal Research*, *157*(1-3), 94-120.

Wallace, P. J. (2005). Volatiles in subduction zone magmas: concentrations and fluxes based on melt inclusion and volcanic gas data. *Journal of Volcanology and Geothermal Research*, *140*(1-3), 217-240.

Wallace, P. J., & Gerlach, T. M. (1994). Magmatic vapor source for sulfur dioxide released during volcanic eruptions: evidence from Mount Pinatubo. *Science*, *265*(5171), 497-499.

Wallace, P. J., Anderson Jr, A. T., & Davis, A. M. (1999). Gradients in H_2O, CO_2, and exsolved gas in a large-volume silicic magma system: Interpreting the record preserved in melt inclusions from the Bishop Tuff. *Journal of Geophysical Research: Solid Earth*, 104(B9), 20097-20122.

Wallace, P. J., Plank, T., Bodnar, R. J., Gaetani, G. A., & Shea, T. (2021). Olivine-hosted melt inclusions: a microscopic perspective on a complex magmatic world. *Annual Review of Earth and Planetary Sciences*, *49*, 465-494.

Waters, L. E., & Lange, R. A. (2015). An updated calibration of the plagioclase-liquid hygrometer-thermometer applicable to basalts through rhyolites. *American Mineralogist*, *100*(10), 2172-2184.

Wei, S. S., Ruprecht, P., Gable, S. L., Huggins, E. G., Ruppert, N., Gao, L., & Zhang, H. (2021). Along-strike variations in intermediate-depth seismicity and arc magmatism along the Alaska Peninsula. *Earth and Planetary Science Letters*, 563, 116878.

Xu, Y., Lin, Y., Zheng, H., & van Westrenen, W. (2024). Non-Henrian behavior of hydrogen in plagioclase–basaltic melt partitioning. *Chemical Geology*, 661, 122153.

Yogodzinski, G. M., Brown, S. T., Kelemen, P. B., Vervoort, J. D., Portnyagin, M., Sims, K. W., Hoernle, K., Jicha, B. R.& Werner, R. (2015). The role of subducted basalt in the source of island arc magmas: Evidence from seafloor lavas of the western Aleutians. *Journal of Petrology*, *56*(3), 441-492.

Yuan, X., Sobolev, S. V., Kind, R., Oncken, O., Bock, G., Asch, G., Schurr, B., Graeber, F., Rudloff, A., Hanka, W., Wylegalla, K., Tibi, R., Haberland, Ch., Rietbrick, A., Giese, P., Wigger, P., Rower, P., Zandt, G., Beck, S., Wallace, T., Pardo, M., & Comte, D. (2000). Subduction and collision processes in the Central Andes constrained by converted seismic phases. *Nature*, *408*(6815), 958-961.

Zellmer, G. F., Edmonds, M., & Straub, S. M. (2015). Volatiles in subduction zone magmatism. *Geological Society, London, Special Publications*, *410*(1), 1-17.

Zhang Y. (1999) H_2O in rhyolitic glasses and melts: Measurement, speciation, solubility and diffusion. *Reviews of Geophysics,* 37, 493–516.

Zhang, Y., Belcher, R., Ihinger, P. D., Wang, L., Xu, Z., & Newman, S. (1997). New calibration of infrared measurement of dissolved water in rhyolitic glasses. *Geochimica et Cosmochimica Acta*, 61(15), 3089–3100.

Figure captions

Figure 1. Location of Cerro Machín volcano, Colombia. (a) Neotectonic map of Colombia including the volcanic chain. (b) Digital elevation model of the outcrop locations (blue dots). Samples from location CMV-008 (represented by a yellow star) were selected for geochemical analysis. Isopachs indicating deposit thickness in cm are shown in black. Towns and roads are shown in dark grey.

Figure 2. Proximal outcrops of the study eruption units ~3 km from the vent at location CMV-008. (a) Photograph of different eruptive units identified at location CMV-008: El Espartillal unit (>5000 yr BP), P0 unit (4500 yr BP), and P1 unit (3600 yr BP). The white arrow points to the P1 deposit that was sampled for this study. (b) Close-up image of the P1 deposit to the right of the shovel in panel a. Lithofacies *a* and *b* are separated by a sharp contact marked in this image by a fine dashed white line for visibility. Lithofacies *a* is fine-grained and laminated. It likely represents the opening phase of the eruption, which may have been phreatomagmatic. Lithofacies *b* is coarse-grained and massive. Pumice clasts were handpicked from this lithofacies from the bottom, middle

1520 and upper portion of P1. The deposit fines upwards and is thought to represent the climactic phase
1521 of the eruption.

1522 Figure 3. Photomicrographs of the different textures identified in plagioclase (Pl), amphibole
1523 (Amp), and olivine (Ol) crystals. Each panel shows plane-polarized and cross-polarized light
1524 images. The cross-polarized light segments of each image can be identified by their black
1525 backgrounds (composed of vesicles and isotropic glass). (a) Photomicrograph of zoned and
1526 euhedral plagioclase with similar anorthite content from core to rim. (b) Photomicrograph of
1527 amphibole phenocryst with invariant Mg# from core to rim. (c) Photomicrograph of amphibole
1528 microphenocryst with normal zoning. (d) Anhedral microphenocryst of olivine surrounded by a
1529 rim of amphibole.

1530 Figure 4. Populations of plagioclase and amphibole crystals analyzed in nine thin sections. Crystals
1531 were picked based on textural observations under the microscope. Different crystal sizes were
1532 analyzed from each textural group. (a) Histogram showing the frequency of different plagioclase
1533 textures. Light gray represents plagioclase with An_{24-38} and dark gray with An_{42-48}. (b) Histogram
1534 showing the frequency of different amphibole textures. Yellow represents amphiboles with Mg# =
1535 53 – 62 and red with Mg# = 66 – 76.

1536 Figure 5. Whole rock chemistry of CMV samples (orange triangles). CMV data available in the
1537 literature are also plotted (grey triangles; from Laeger *et al.*, 2013; Régnier, 2015). (a) Total alkalis
1538 vs. silica (TAS) diagram (after Le Bas *et al.*, 1986). Melt inclusions (orange circles) and glass (pink
1539 circles) measurements are also plotted (Supplementary Table B3). (b) Sr/Y versus Y. The typical
1540 arc magmatic rocks and the adakite fields are defined by Defant & Drummond (1990). (c) MgO
1541 versus SiO_2 diagram (Martin *et al.,* 2005) discriminating high-silica adakites (HSA) from low-silica

1542 adakites (LSA). (d) Cr/Ni vs. TiO_2 diagram (Martin *et al.*, 2005) discriminating high-silica adakites
1543 (HSA) from low-silica adakites (LSA).

1544 Figure 6. Volatiles in melt inclusions hosted in plagioclase and quartz. (a) Photomicrograph of
1545 trigonal bipyramidal melt inclusion hosted in quartz. Note the halo of small inclusions around this
1546 melt inclusion, which may have formed during rupture and re-sealing of the inclusion (e.g., Wallace
1547 *et al.,* 2021). (b) Photomicrograph of quartz-hosted melt inclusion filled with bubbles. The
1548 inclusion likely ruptured and decrepitated during decompression (e.g., Bachmann *et al.*, 2010). (c)
1549 Concentrations of H_2O and CO_2 in quartz- and plagioclase-hosted melt inclusions. Isobars, open-
1550 and closed-system degassing paths and vapor isopleths for 1, 10 20 and 40% CO_2 were calculated
1551 using VolatileCalc (Newman & Lowenstern, 2002). Uncertainties are shown in Fig. 9.

1552 Figure 7. (a) Calibration curve for H_2O (total H quantified as H_2O equivalents) in rhyolite glasses
1553 by SIMS. (b) Comparison of water contents obtained by NanoSIMS and FTIR for five singly-
1554 exposed quartz-hosted melt inclusions. Error bars are one standard deviation. Error bars on FTIR
1555 data account for uncertainties in sample thickness, absorption peak height, and propagating
1556 uncertainties on the Zhang *et al.* (1997) fit parameters. The sample thickness estimates are the
1557 largest source of error. Error bars on the NanoSIMS data are due to the reproducibility of the
1558 analysis based on replicate measurements on N6-glass (8% uncertainty) (See Supplementary Table
1559 C2).

1560 Figure 8. FTIR measurements of water in plagioclase crystals. (a) Polarized FTIR spectra measured
1561 along three perpendicular directions in a plagioclase crystal. (b) Total water concentrations
1562 measured in three plagioclase crystals (from 17 plagioclase crystals analyzed) representing the full
1563 range of measured water concentrations. Note that all crystals have approximately uniform water

concentrations from core to rim. Profile lengths are shorter than the initial crystal size because crystals were cut in half for FTIR measurements. (c) Water in plagioclase versus crystal size for 17 plagioclase crystals. Notably, no relationship between size and water content is observed.

Figure 9. Water concentration (weight ppm H_2O) of hydrated plagioclase versus total H_2O concentration of coexisting basaltic andesitic glass from Hamada *et al.* (2013), MORB from Hamada *et al.* (2013) and dacites from Mt. Hood from Caseres *et al.* (2018). The partition coefficient proposed by Hamada *et al.* (2013) for melts with >4 wt% H_2O is shown in blue and a partition coefficient of 0.002 (Caseres *et al.*, 2018; Mosenfelder *et al.,* 2020) is shown in purple. We fit a square root relationship (Equation 7; shown as a black curve) to the Hamada *et al.* (2013) and Caseres *et al.* (2018) data by applying least-squares minimization. Note that the Hamada *et al.* (2013) data are recalculated using the FTIR absorption coefficient provided by Mosenfelder *et al.* (2015). Shaded areas correspond to an error of 10%.

Figure 10. (a) Comparison of total water measured in melt inclusions by FTIR and SIMS, and estimates of total water in CMV melt based upon measured water concentrations in plagioclase (section 4.4). For the water-in-plagioclase partitioning calculations, we assume a partition coefficient of 0.002 (Mosenfelder *et al.*, 2020) and we also apply the square root function proposed in this study (Equation 12). (b) Plagioclase hygrometry model of Waters & Lange (2015) run at a range of anorthite contents from An_{20} to An_{40}, a range of melt compositions from dacite (corresponding to the average CMV whole rock composition) to rhyolite (corresponding to the average composition of the melt inclusions), and a pressure of 350 MPa (the maximum pressure that the model is calibrated to). Dashed lines denote extrapolation of the model to temperatures lower than 750 °C. (c) Density plots for the water data in panel a.

Figure 11. Pressures and temperatures of crystallization. (a) Constraints from equilibrium amphibole-liquid pairs using Putirka (2016) in yellow, Ridolfi (2021) in gray, and Higgins *et al.* (2022) in blue. Data points represent measurements in the rim (open circles) and core (filled circles) of individual crystals. (b) Probability density estimates of temperature. (c) Temperatures obtained by plagioclase-liquid equilibrium pairs using Putirka (2008). (d) Probability density estimates of pressure. (e) Saturation pressures of melt inclusions calculated by VolatileCalc (Newman & Lowenstern, 2002; see section 4.3).

Figure 12. Melt composition based on amphibole chemometry of Higgins *et al.* (2022). Amphiboles crystallizing from a rhyolitic and dacitic magma are plotted as light and dark red circles, respectively. Amphiboles crystallizing from an andesitic magma are plotted as black circles.

Figure 13. Summary schematic diagram representing the combined geochemical and seismic datasets. Crystallization conditions calculated from amphibole, plagioclase, and melt inclusions overlap with seismicity depths at CMV from 2009 – 2015 and CO_2 isotope measurements from 2013 – 2014 campaigns (Inguaggiato *et al.*, 2017). The main dacitic reservoir is represented in green-yellowish whereas the andesitic magma recharge is in green-orangish.

Figure 14. Phase diagram for Pinatubo dacite based on the experiments of Conrad *et al.* (1988), Prouteau & Scaillet (2003) and Rutherford & Devine (1996). Plagioclase and hornblende stability curves are shown for water-saturated magma and magma containing 7 wt% H_2O. Biotite and quartz stability curves are taken from Rutherford & Devine (1996). The dashed line for the quartz stability curve is extrapolated using Prouteau & Scaillet (2003) experiments on Pinatubo dacite at 960 MPa and 400 MPa at water saturation conditions (indicated as "x"). The dashed line for the biotite stability curve is extrapolated using Conrad *et al*. (1988) experiments on Taupo dacite at 1000 MPa

at water saturation conditions (indicated as "x"). Water concentration was calculated using the VolatileCalc solubility curve for rhyolite (Newman & Lowestern, 2002). Water concentration was projected for pressures >500 MPa. CMV amphibole thermobarometry results are plotted using the same color code as Fig. 12. The P-T region in which quartz, biotite, plagioclase and hornblende are all stable is shaded in red.

Figure 15. Compilation of H_2O vs CO_2 measurements in dacites and rhyolites from various volcanic arcs (modified from Wallace, 2005). Data are shown for the Satsuma-Iwojima (Saito *et al.,* 2001), Altiplano-Puna, Northern Chile (Schmitt, 2001), Augustine (Roman *et al.,* 2006), Toba Tuff (Newman & Chesner, 1989), Pinatubo (Wallace & Gerlach, 1994), and Mt. Mazama (Bacon *et al.,* 1992). Note that Borisova *et al.* (2006) report concentrations in experimentally rehomogenized Pinatubo melt inclusions up to 8.79 wt% H_2O (by SIMS), but that study did not report CO_2 concentrations, so the data are not plotted here. Isobars for 100, 200 and 500 MPa were calculated using VolatileCalc (Newman & Lowenstern, 2002).

Figure 16. (a) Pb/Th vs. Th/La and (b) Ba/Th vs. La/Th diagrams support the role of melting sediments in adakite genesis. (c) Multi-element diagram normalized to primitive mantle (Sun & McDonough, 1989). Whole-rock geochemical CMV samples are orange triangles. For comparison CMV data available in the literature are also plotted (gray triangles; Laeger *et al.,* 2013; Régnier, 2015). Samples that do not exhibit a garnet signature are plotted for comparison (N-MORB, E-MORB from Sun & McDonough, 1989; the Mexican Volcanic Belt (MVB) from Straub *et al.,* 2014). (d) Petrogenetic process vectors (PPVs) of Gao *et al.* (2023) are shown to explain the origin of CMV adakites from the rare earth element (REE) perspective. The PPVs connect the shape coefficients (λ_1 and λ_2; calculated using Anenburg & Williams, 2022 - BLambdaR program) of the upper oceanic crust (UOC) with the observed shape coefficients of CMV dacites. Approximately

1631 ~5% fractional crystallization of garnet following 10% partial melting of the UOC source provides
1632 a good match to the CMV data.

1633 Figure 17. (a) Ni and forsterite contents in olivine phenocrysts. Green and red fields are olivines
1634 calculated to be in equilibrium with pyroxenite and peridotite source compositions (fields and
1635 shallow crystallization lines are taken from Rupretch & Plank, 2013 and Straub *et al.*, 2011). (b)
1636 The Rhodes diagram as a test of olivine-liquid equilibrium (olivine Mg# vs whole-rock Mg#). The
1637 envelope of olivine–liquid Fe–Mg distribution coefficient (K_D) of 0.30 ± 0.03 is drawn after Roeder
1638 & Emslie (1970). One whole rock composition is in chemical equilibrium with olivine. (c)
1639 FeO*/MgO versus SiO_2 diagram showing the calc-alkaline (CA) and tholeiitic (TH) dividing line
1640 of Miyashiro (1974). Primary melts defining the mantle melting array are taken from Grove *et al.*
1641 (2012). Fractional crystallization paths in H_2O magma suites are shown for three different starting
1642 compositions: basaltic, primitive basaltic andesite (compiled from Sisson & Grove, 1993), and
1643 primitive magnesian andesite (from Mt. Shasta, California, Grove *et al.*, 2003). The crystallization
1644 path for CMV dacites projects toward high -SiO_2 andesitic primary mantle melt composition.
1645 Modified after Grove *et al.* (2012).

1646 **Tables**

1647 Table 1. Water and carbon dioxide concentrations measured by FTIR (in 35 melt inclusions) and
1648 NanoSIMS (in 5 melt inclusions).

1649 Table 2. Water in melt calculated using a partition coefficient of 0.002 as calculated for natural
1650 plagioclase-melt pairs from a dacitic system (Mt. Hood; Caseres *et al.*, 2018; Mosenfelder *et al.*,
1651 2020) and the square root parameterization of the plagioclase-melt partition coefficients (section
1652 4.4) reported by Hamada *et al.* (2013) and Caseres *et al.* (2018).

Table 3. Compositions of Cerro Machín and Pinatubo dacites (Prouteau & Scaillet, 2003), the high-Mg andesite of Mt. Shasta (Grove *et al.,* 2005), and average Cenozoic adakites (Drummond *et al*., 1996).

Supplementary data

Supplementary Table A1. Concentration of volatiles in melt inclusions as determined by FTIR and NanoSIMS. Estimated saturation entrapment pressures from the Newman & Lowestern (2002) and Papale *et al.* (2006) models.

Supplementary Table A2. Volume occupied by bubbles in the melt inclusions.

Supplementary Table A3. Spectra data for melt inclusions B1 Qz5 and d1 Qz10.

Supplementary Figure A1. Photomicrographs of some melt inclusions used for calculations of the bubble volumes. Melt inclusions are highlighted by a red arrow. Multiple bubbles from the same crystal were considered for calculations. Results are tabulated in Supplementary Table A2.

Supplementary Figure A2. Melt inclusion volumes vs. Bubble volumes diagram. Volumes were calculated assuming spherical geometries for the melt inclusions and bubbles. An average of three diameter measurements was used to calculate the radius. When multiple bubbles were observed within the melt inclusion, all bubbles were summed together to calculate the total volume occupied by bubbles.

Supplementary Figure A3. FTIR data. (a) Photomicrograph taken by the FTIR of B1 Qz5 melt inclusion with 10.7 wt% H_2O. Inset: Magnified image of the melt inclusion. The red cross denotes the center of the pictures. (b) Picture of the wafer thickness for crystal B1 Qz5 under the binocular. Red arrows indicate where the thickness was measured. (c) Thickness-normalized spectra for two crystals B1 Qz5, and d1 Qz10 with 10.7 and 9.6 wt% H_2O, respectively. Raw data is in Supplementary Table A3.

Supplementary Table B1. Electron microprobe analyses of Morgan glasses.

Supplementary Table B2. Whole rock analyses of five pumice clasts.

Supplementary Table B3. Electron microprobe analyses of glass and melt inclusions.

Supplementary Figure B1. Whole-rock geochemical plots of the analyzed samples. CMV data available in the literature are also plotted (whole rock chemistry: gray triangles, glass: gray circles; Laeger *et al.*, 2013; Régnier, 2015). A. Total Alkalis vs. Silica (TAS) diagram (after Le Bas *et al.*, 1986); (B-J) variation diagrams of the main major oxides. Arrows indicate samples trends in the data.

Supplementary Figure B2. (a) Pb/Th versus Nd/Th support the role of sediment melting in CMV dacites genesis. MORB, eclogite melt and sediment melt fields are taken from Wei *et al.* (2021). (b) Dy/Yb versus SiO_2 diagram to show expected fractionation effects with differentiation. The schematic inset shows expected fractionation effects. Vectors represent example suites that have fractionated garnet and amphibole from a different parent composition (vectors taken from Davidson *et al.,* 2007). CMV samples (data taken from Laeger *et al*., 2013; Régnier, 2015) are consistent with variable amounts of garnet fractionation. Legend is the same as Supplementary Figures B1.

Supplementary Table C1. NanoSIMS standards from Carnegie Earth and Planets Laboratory.

Supplementary Table C2. Repeat analyses of NanoSIMS standard N6.

Supplementary Table C3. Raw SIMS data.

Supplementary Figure C1. Photomicrographs of the five melt inclusions measured by NanoSIMS. The first column shows the indium mounts containing the quartz crystals analyzed. Red arrows point to the melt inclusion analyzed in each crystal.

Supplementary Table D1. Summary of temperature and pressure conditions calculated from amphibole compositions using the Higgins *et al.* (2022), Ridolfi (2021) (temperature ± 22 °C, pressure ± 12% MPa) and Putirka (2016) (temperature ± 30 °C, pressure ± 200 MPa) geothermobarometers. High-Mg amphibole crystals, cores of normally zoned crystals and rims of reversed zoned crystals did not meet the equilibrium conditions ($K_D = 0.28 \pm 0.11$ criterion) for Putirka (2016) geothermobarometer.

Supplementary Table D2. Summary of temperature conditions calculated from plagioclase composition using the Putirka (2008) (temperature ± 48 °C) geothermometer.

Supplementary Table E1. Electron Microprobe analyses of amphibole. Data was filtered using anomalies in total values, Al_2O_3, FeO and MgO. Also, data was filtered using amphibole formula of Li *et al.* (2020). The Fe-Mg exchange coefficients yield K_D(Fe-Mg) Amp-liq = 0.28 ± 0.11 (Mg# <65) (Putirka, 2008), using average glass composition.

Supplementary Table E2. Electron Microprobe analyses of plagioclase. Data was filtered using anomalies in total values, Al_2O_3, CaO and Na_2O. The An-Ab exchange coefficients yield $K_D(An\text{-}Ab)^{pl\text{-}liq} = 0.1 \pm 0.05$ (Putirka, 2008), using average glass composition.

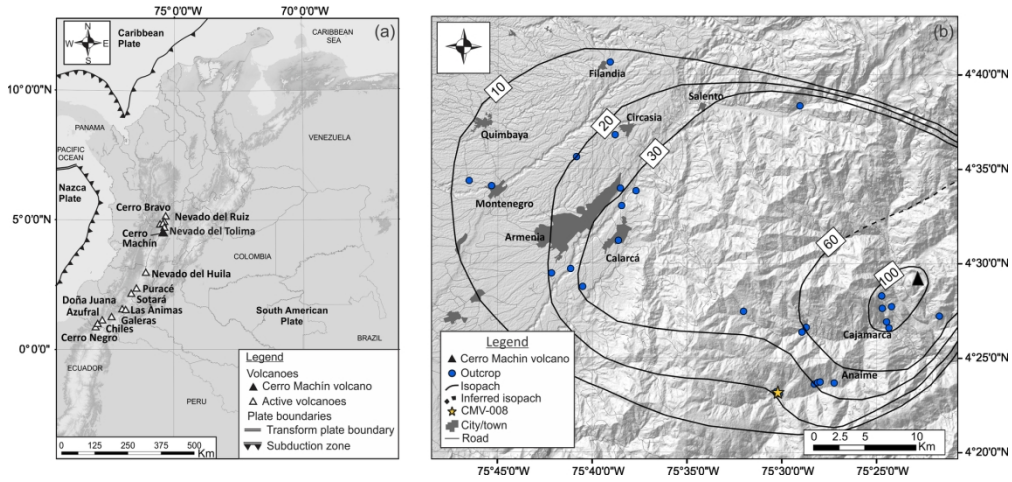

Figure 1. Location of Cerro Machín volcano, Colombia. (a) Neotectonic map of Colombia including the volcanic chain. (b) Digital elevation model of the outcrop locations (blue dots). Samples from location CMV-008 (represented by a yellow star) were selected for geochemical analysis. Isopachs indicating deposit thickness in cm are shown in black. Towns and roads are shown in dark grey.

178x98mm (300 x 300 DPI)

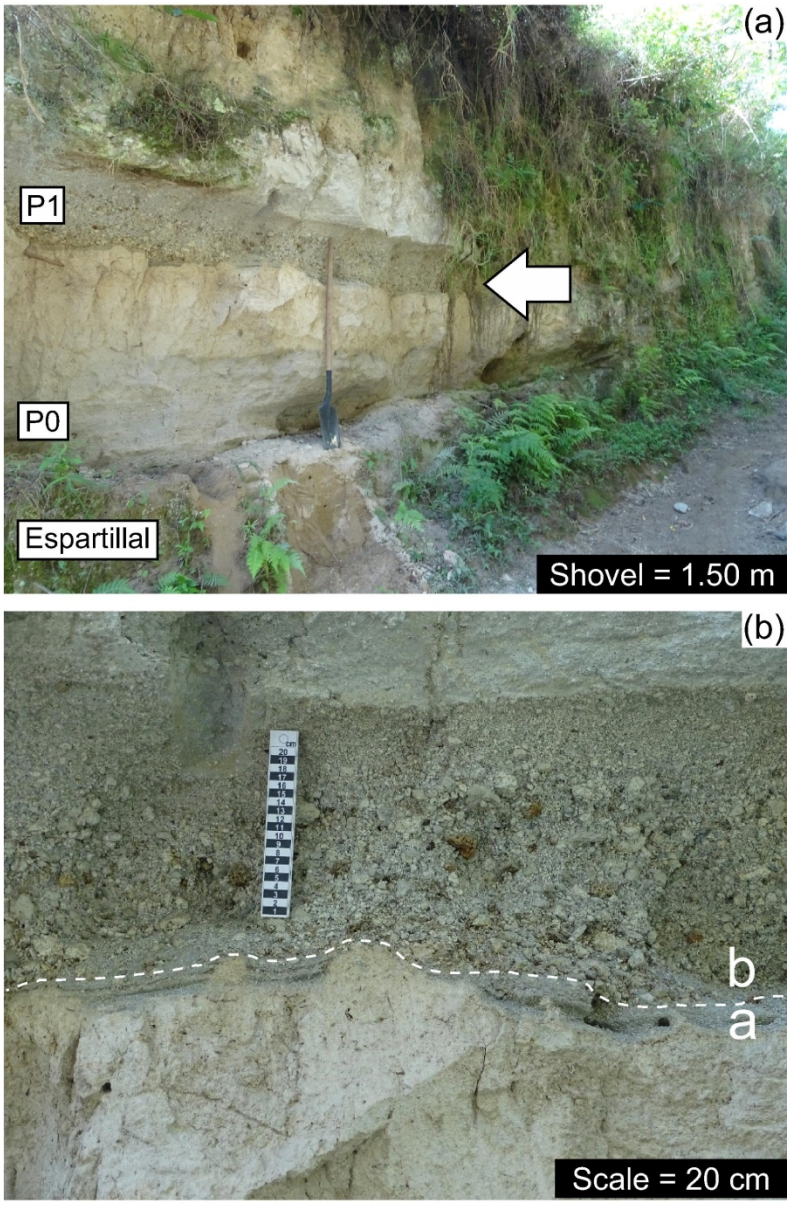

Figure 2. Proximal outcrops of the study eruption units ~3 km from the vent at location CMV-008. (a) Photograph of different eruptive units identified at location CMV-008: El Espartillal unit (>5000 yr BP), P0 unit (4500 yr BP), and P1 unit (3600 yr BP). The white arrow points to the P1 deposit that was sampled for this study. (b) Close-up image of the P1 deposit to the right of the shovel in panel a. Lithofacies *a* and *b* are separated by a sharp contact marked in this image by a fine dashed white line for visibility. Lithofacies *a* is fine-grained and laminated. It likely represents the opening phase of the eruption, which may have been phreatomagmatic. Lithofacies *b* is coarse-grained and massive. Pumice clasts were handpicked from this lithofacies from the bottom, middle and upper portion of P1. The deposit fines upwards and is thought to represent the climactic phase of the eruption.

80x122mm (600 x 600 DPI)

Table 1: Water and carbon dioxide concentrations measured by FTIR (in 35 melt inclusions) and NanoSIMS (in 5 melt inclusions).

No.	Pumice	Crystal	FTIR		NanoSIMS	Thickness (microns)	Size MI (microns)
			H_2O (wt.%)	CO_2 (ppm)	H_2O (wt.%)		
1	B1	Pl7	3.5 ± 0.8	59 ± 15		24 ± 2	48
2	B1	Pl9	3.2 ± 0.2	b.d.l.		21 ± 1	51
3	B1	Qz5	10.7 ± 1.4	185 ± 32		24 ± 2	94
4	B2	Pl5	4.1 ± 1.3	110 ± 23		27 ± 3	50
5	B2	Pl6	6.3 ± 0.6	87 ± 12		19 ± 1	52
6	B2	Pl8M1	4.9 ± 1.1	70 ± 21		20 ± 3	43
7	B2	Pl8M2	4.8 ± 1.0	90 ± 17		20 ± 3	49
8	B2	Qz6	2.5 ± 1.0	230 ± 59		16 ± 2	43
9	M1	Qz1	6.9 ± 1.2	136 ± 17		24 ± 2	49
10	M1	Pl1*	1.6 ± 0.5	b.d.l.		12 ± 2	27
11	M1	Pl2M1*	1.4 ± 0.3	b.d.l.		17 ± 3	44
12	M1	Pl2M2*	1.1 ± 0.2	b.d.l.		17 ± 3	53
13	M1	Pl2M3*	1.5 ± 0.3	b.d.l.		17 ± 3	42
14	M8	Pl2*	1.6 ± 0.3	b.d.l.		16 ± 1	62
15	M8	Pl3	3.0 ± 0.5	b.d.l.		24 ± 1	43
16	M8	Pl5	2.1 ± 0.4	b.d.l.		21 ± 3	54
17	M8	Qz1	4.3 ± 0.4	130 ± 19		23 ± 1	42
18	T7	Pl11	1.9 ± 0.4	69 ± 13		32 ± 3	48
19	T7	Pl12	2.7 ± 0.4	21 ± 3		174 ± 1	96
20	T7	Pl9P	1.7 ± 0.4	b.d.l.		29 ± 1	55
21	T7	Qz2M1	4.1 ± 1.4	105 ± 41		28 ± 1	40
22	T7	Qz2M2	3.7 ± 0.8	99 ± 39		28 ± 1	46
23	T7	Qz2M3	3.5 ± 1.2	91 ± 38		28 ± 1	44
24	T9	Qz1	3.2 ± 0.6	126 ± 28		39 ± 3	77
25	T9	Qz3	4.6 ± 0.5	109 ± 14		36 ± 3	52
26	d1	Qz2**	8.2 ± 4.9	289 ± 24	7.1 ± 0.6+	21 ± 14	72
27	d1	Qz3**	2.2 ± 2.0	49 ± 6	5.8 ± 0.5+	52 ± 57	84
28	d1	Qz4**	4.5 ± 2.1	167 ± 23		21 ± 9	66
29	d1	Qz5**	6.8 ± 1.1	155 ± 16	7.7 ± 0.6+	54 ± 9	125
30	d1	Qz6**	10.3 ± 5.8	445 ± 119	6.1 ± 0.5+	15 ± 8	72
31	d1	Qz7**	7.9 ± 1.9	428 ± 81	7.4 ± 0.6+	30 ± 7	70
32	d1	Qz8**	0.5 ± 0.1	b.d.l.		40 ± 7	56
33	d1	Qz9	7.4 ± 0.5	184 ± 19		57 ± 3	107
34	d1	Qz10	9.6 ± 2.2	377 ± 122		41 ± 9	137
35	d1	Qz11	7.3 ± 0.7	59 ± 9		35 ± 3	107

Uncertainties calculated using Monte Carlo simulation.
** Singly exposed melt inclusions. Note the relatively large error bars on these measurements. Quantifications of these uncertainties are discussed in section 4.3.

* Melt inclusions in which ~3550 cm^{-1} peak was used for water calculations. Molar absorbance coefficient was taken from Newman *et al.* (1986).
+ Uncertainties (1σ) calculated using replicate measurements of the high-water standard N6 (Withers and Behrens, 2002).
b.d.l. = below detection limit.
Melt inclusions measured in the same crystal are noted as M1, M2, M3 in the "Crystal" column.

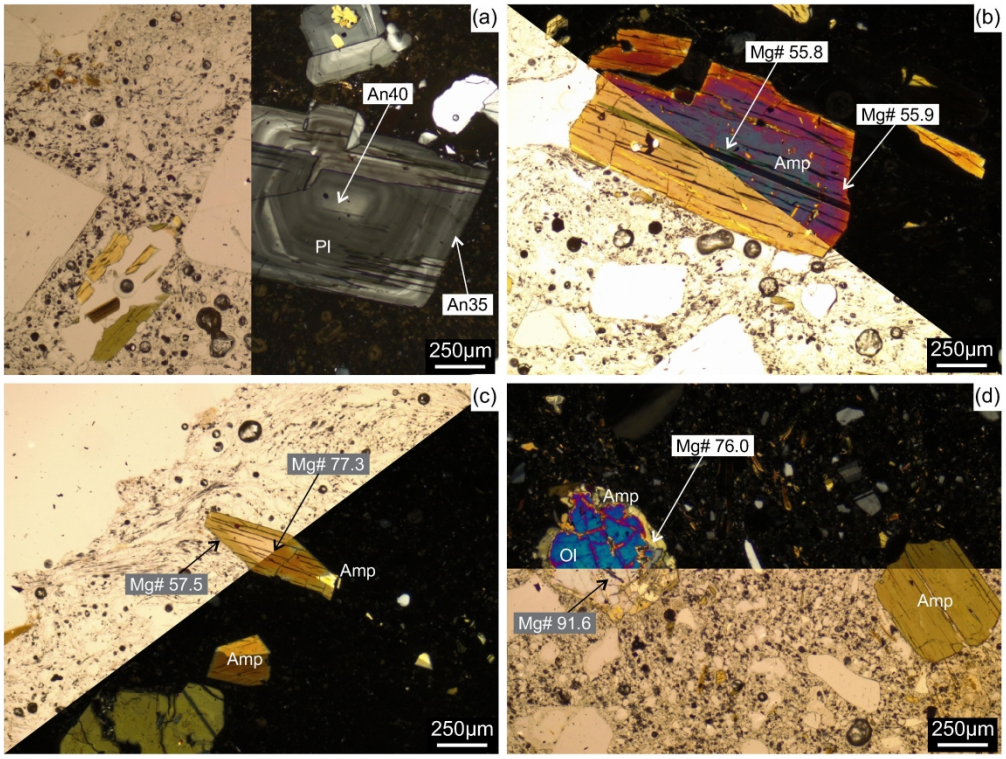

Figure 3. Photomicrographs of the different textures identified in plagioclase (Pl), amphibole (Amp) and olivine (Ol) crystals. Each panel shows plane-polarized and cross-polarized light images. The cross-polarized light segments of each image can be identified by their black backgrounds (composed of vesicles and isotropic glass). (a) Photomicrograph of zoned and euhedral plagioclase with similar anorthite content from core to rim. (b) Photomicrograph of amphibole phenocryst with invariant Mg# from core to rim. (c) Photomicrograph of amphibole microphenocryst with normal zoning. (d) Anhedral microphenocryst of olivine surrounded by a rim of amphibole.

168x136mm (600 x 600 DPI)

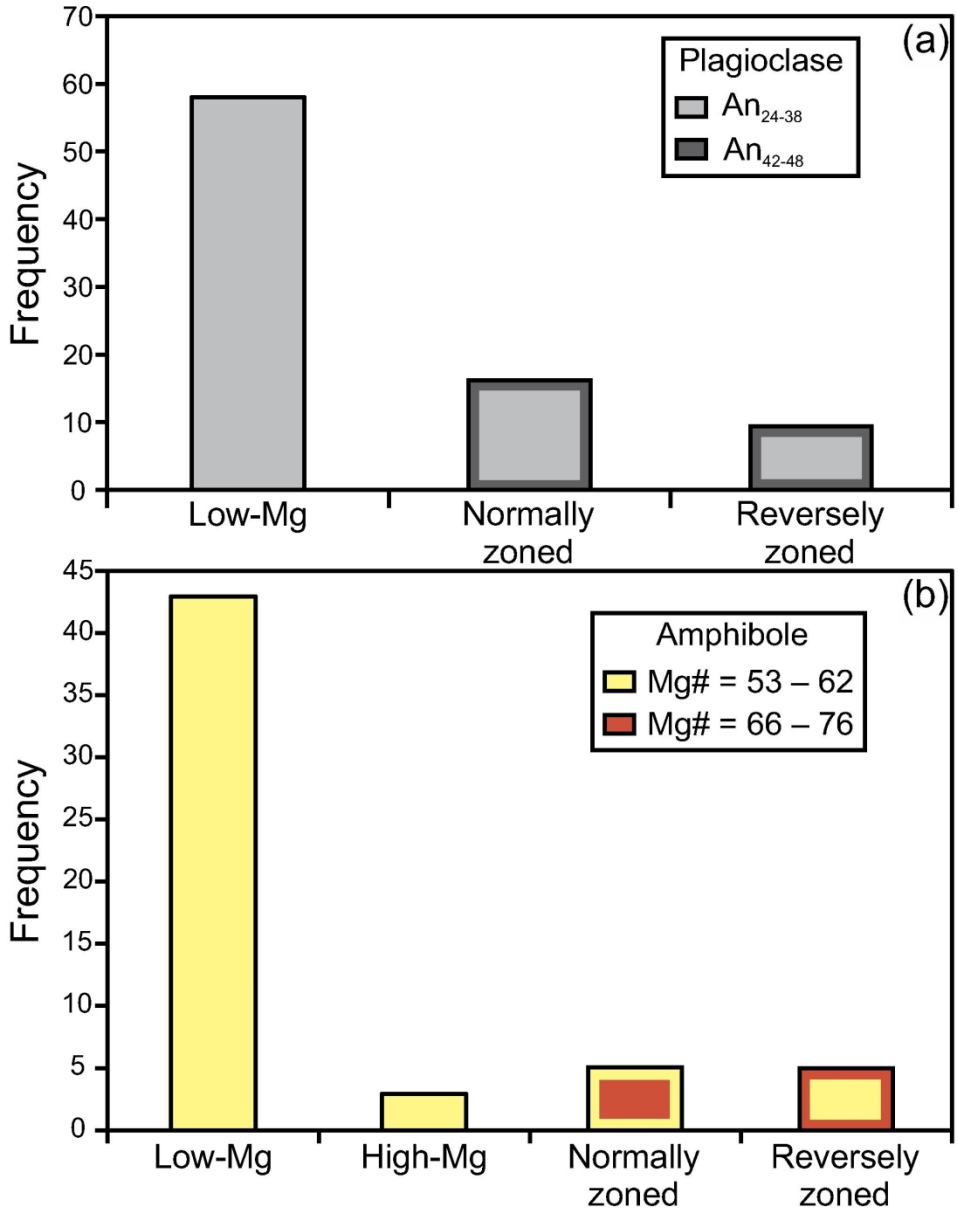

Figure 4. Populations of plagioclase and amphibole crystals analyzed in nine thin sections. Crystals were picked based on textural observations under the microscope. Different crystal sizes were analyzed from each textural group. (a) Histogram showing the frequency of different plagioclase textures. Light gray represents plagioclase with An_{24-38} and dark gray with An_{42-48}. (b) Histogram showing the frequency of different amphibole textures. Yellow represents amphiboles with Mg# = 53 – 62 and red with Mg# = 66 – 76.

85x107mm (600 x 600 DPI)

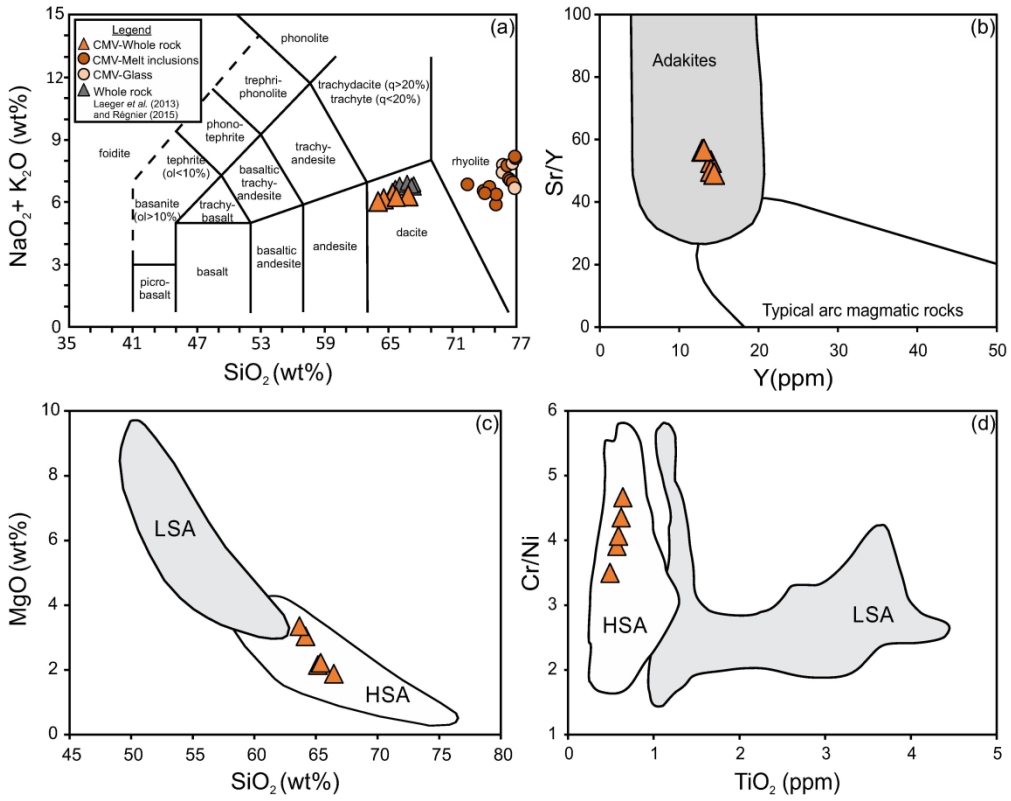

Figure 5. Whole rock chemistry of CMV samples (orange triangles). CMV data available in the literature are also plotted (grey triangles; from Laeger *et al.*, 2013; Régnier, 2015). (a) Total alkalis vs. silica (TAS) diagram (after Le Bas *et al.*, 1986). Melt inclusions (orange circles) and glass (pink circles) measurements are also plotted (Supplementary Table B3). (b) Sr/Y versus Y. The typical arc magmatic rocks and the adakite fields are defined by Defant & Drummond (1990). (c) MgO versus SiO2 diagram (Martin et al.,2005) discriminating high-silica adakites (HSA) from low-silica adakites (LSA). (d) Cr/Ni vs. TiO_2 diagram (Martin *et al.*, 2005) discriminating high-silica adakites (HSA) from low-silica adakites (LSA).

170x134mm (600 x 600 DPI)

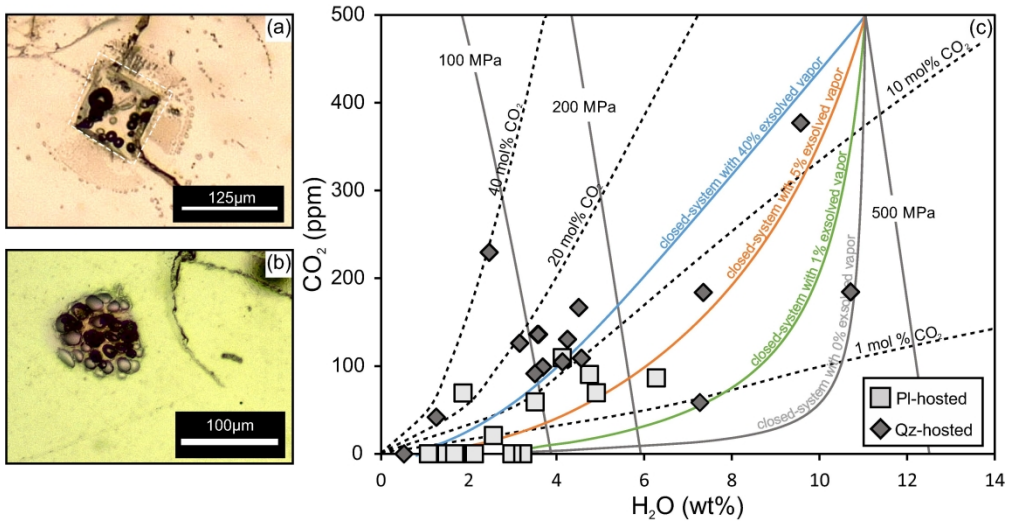

Figure 6. Volatiles in melt inclusions hosted in plagioclase and quartz. (a) Photomicrograph of trigonal bipyramidal melt inclusion hosted in quartz. Note the halo of small inclusions around this melt inclusion, which may have formed during rupture and re-sealing of the inclusion (e.g., Wallace *et al.,* 2021). (b) Photomicrograph of quartz-hosted melt inclusion filled with bubbles. The inclusion likely ruptured and decrepitated during decompression (e.g., Bachmann *et al.,* 2010). (c) Concentrations of H_2O and CO_2 in quartz- and plagioclase-hosted melt inclusions. Isobars, open- and closed-system degassing paths and vapor isopleths for 1, 10 20 and 40% CO_2 were calculated using VolatileCalc (Newman & Lowenstern, 2002). Uncertainties are shown in Fig. 9.

171x88mm (600 x 600 DPI)

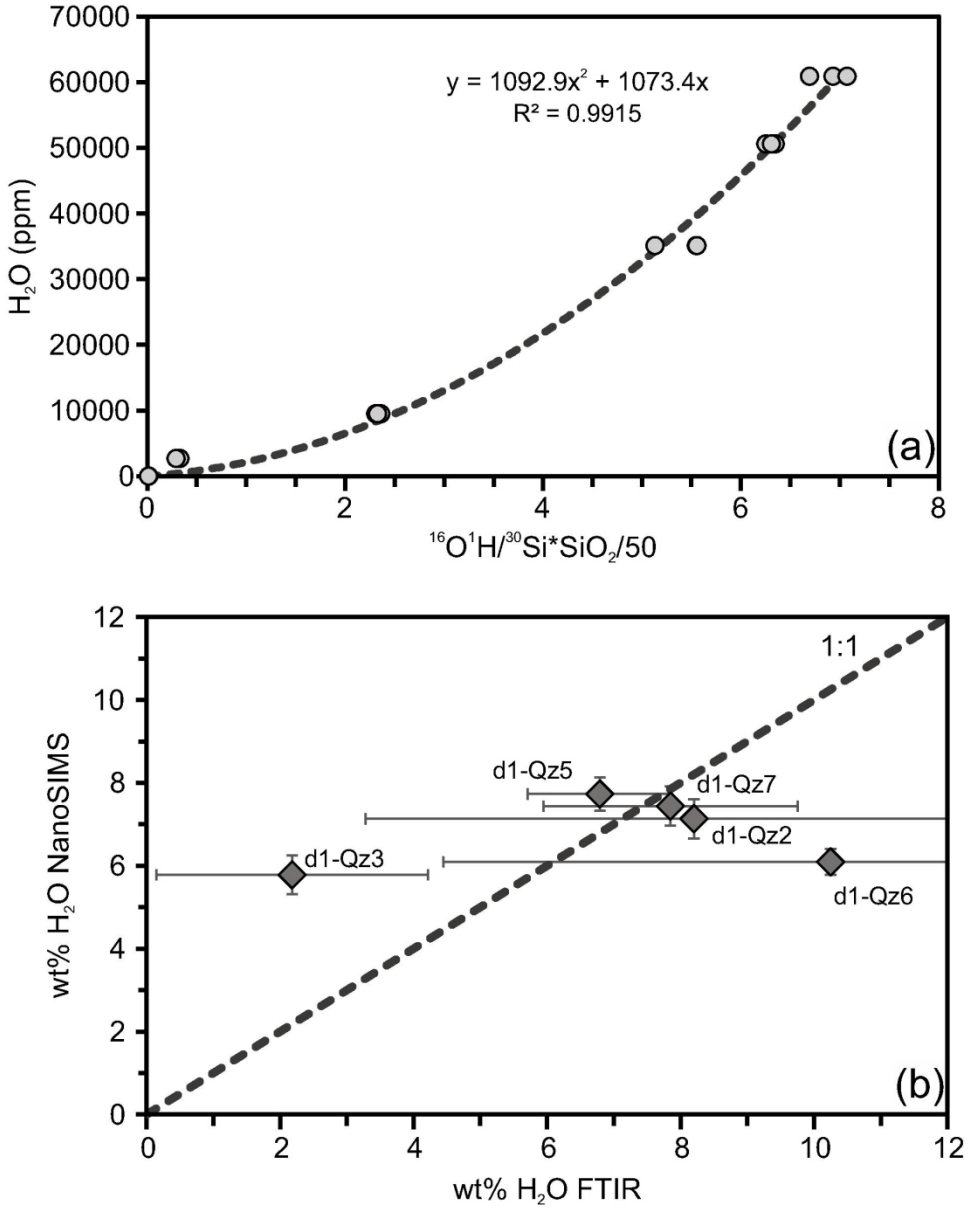

Figure 7. (a) Calibration curve for H_2O (total H quantified as H_2O equivalents) in rhyolite glasses by SIMS. (b) Comparison of water contents obtained by NanoSIMS and FTIR for five singly-exposed quartz-hosted melt inclusions. Error bars are one standard deviation. Error bars on FTIR data account for uncertainties in sample thickness, absorption peak height, and propagating uncertainties on the Zhang *et al*. (1997) fit parameters. The sample thickness estimates are the largest source of error. Error bars on the NanoSIMS data are due to the reproducibility of the analysis based on replicate measurements on N6-glass (8% uncertainty) (See Supplementary Table C2).

81x102mm (600 x 600 DPI)

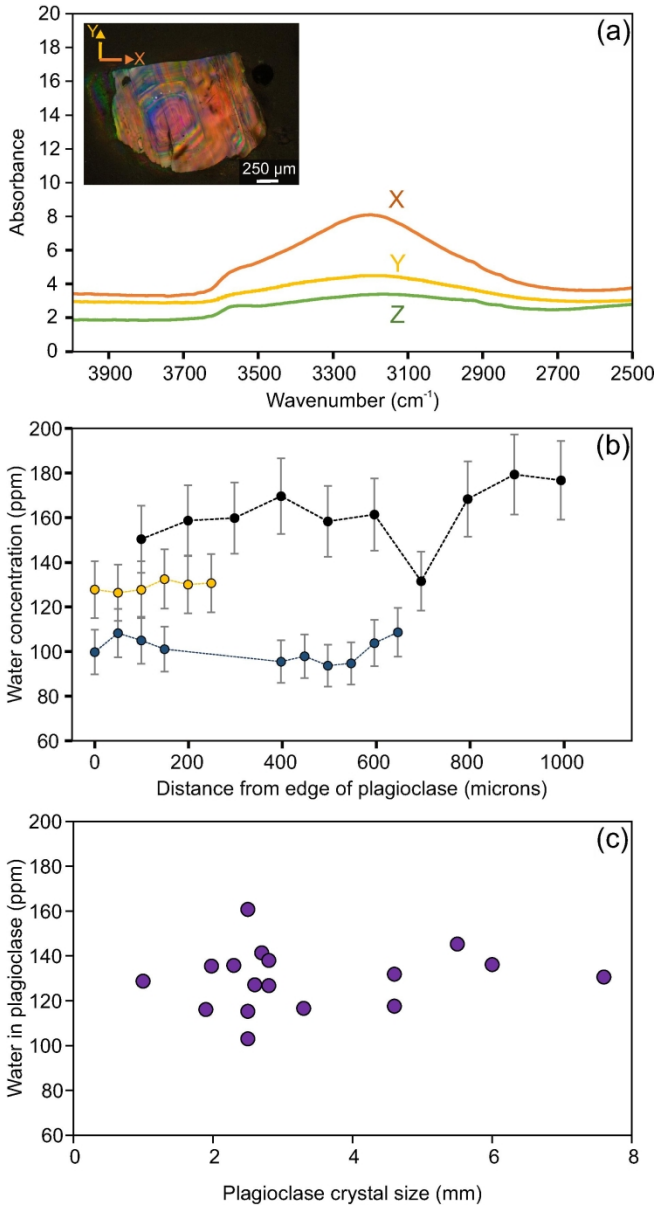

Figure 8. FTIR measurements of water in plagioclase crystals. (a) Polarized FTIR spectra measured along three perpendicular directions in a plagioclase crystal. (b) Total water concentrations measured in three plagioclase crystals (from 17 plagioclase crystals analyzed) representing the full range of measured water concentrations. Note that all crystals have approximately uniform water concentrations from core to rim. Profile lengths are shorter than the initial crystal size because crystals were cut in half for FTIR measurements. (c) Water in plagioclase versus crystal size for 17 plagioclase crystals. Notably, no relationship between size and water content is observed.

80x149mm (600 x 600 DPI)

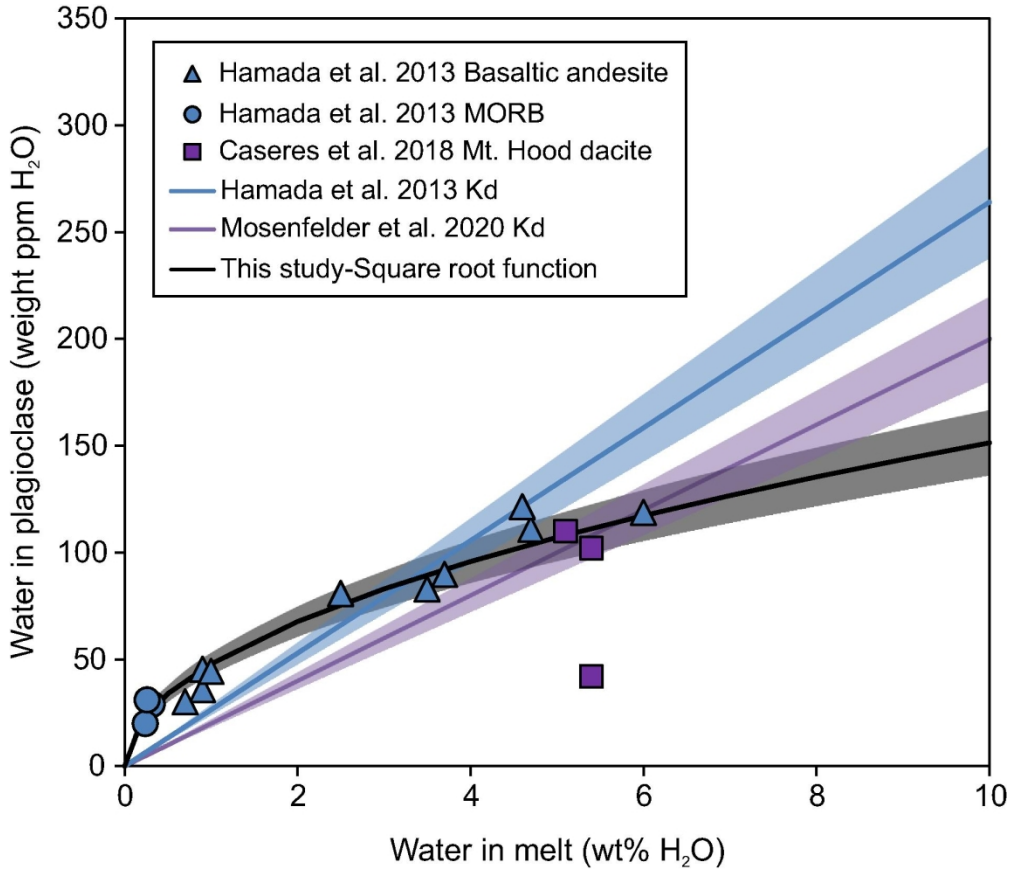

Figure 9. Water concentration (weight ppm H_2O) of hydrated plagioclase versus total H_2O concentration of coexisting basaltic andesitic glass from Hamada *et al.* (2013), MORB from Hamada *et al.* (2013) and dacites from Mt. Hood from Caseres *et al.* (2018). The partition coefficient proposed by Hamada *et al.* (2013) for melts with >4 wt% H_2O is shown in blue and a partition coefficient of 0.002 (Caseres *et al.,* 2018; Mosenfelder *et al.,* 2020) is shown in purple. We fit a square root relationship (Equation 7; shown as a black curve) to the Hamada *et al.* (2013) and Caseres *et al.* (2018) data by applying least-squares minimization. Note that the Hamada *et al.* (2013) data are recalculated using the FTIR absorption coefficient provided by Mosenfelder *et al.* (2015). Shaded areas correspond to an error of 10%.

80x69mm (600 x 600 DPI)

Table 2: Water in melt calculated using a partition coefficient of 0.002 as calculated for natural plagioclase-melt pairs from a dacitic system (Mt. Hood; Caseres *et al.*, 2018; Mosenfelder *et al.*, 2020) and the square root parameterization of the plagioclase-melt partition coefficients (section 4.4) reported by Hamada *et al.* (2013) and Caseres *et al.* (2018).

				Water in melt (wt. %)	
No	Pumice	Plagioclase	Water in Pl (weight ppm)	Melt H_2O with constant Kd (0.002)	Melt H_2O with variable Kd (Square root)
1	B1	Pl1	129 ± 12	6 ± 1	7 ± 1
2	B1	Pl2	103 ± 10	5 ± 1	5 ± 1
3	B1	Pl3	115 ± 11	6 ± 1	6 ± 1
4	B1	Pl13	141 ± 14	7 ± 1	9 ± 2
5	B1	Pl14	135 ±13	7 ± 1	8 ± 2
6	B2	Pl1	117 ± 11	6 ± 1	6 ± 1
7	B2	Pl2	117 ± 11	6 ± 1	6 ± 1
8	M7	Pl1	136 ± 13	7 ± 1	8 ± 2
9	M7	Pl2	127 ± 12	6 ± 1	7 ± 2
10	M7	Pl3	127 ± 12	6 ± 1	7 ± 2
11	M9	Pl1	132 ± 13	7 ± 1	8 ± 2
12	M9	Pl2	116 ± 11	6 ± 1	6 ± 1
13	T7	Pl1	145 ± 14	7 ± 1	9 ± 2
14	T7	Pl2	131 ± 13	7 ± 1	7 ± 2
15	T9	Pl1	138 ± 13	7 ± 1	8 ± 2
16	T9	Pl2	136 ± 13	7 ± 1	8 ± 2
17	T9	Pl3	161 ± 16	8 ± 1	11 ± 2

Uncertainties are propagated assuming an error of ± 10% for water in plagioclase from Mosefelder *et al.* (2020).

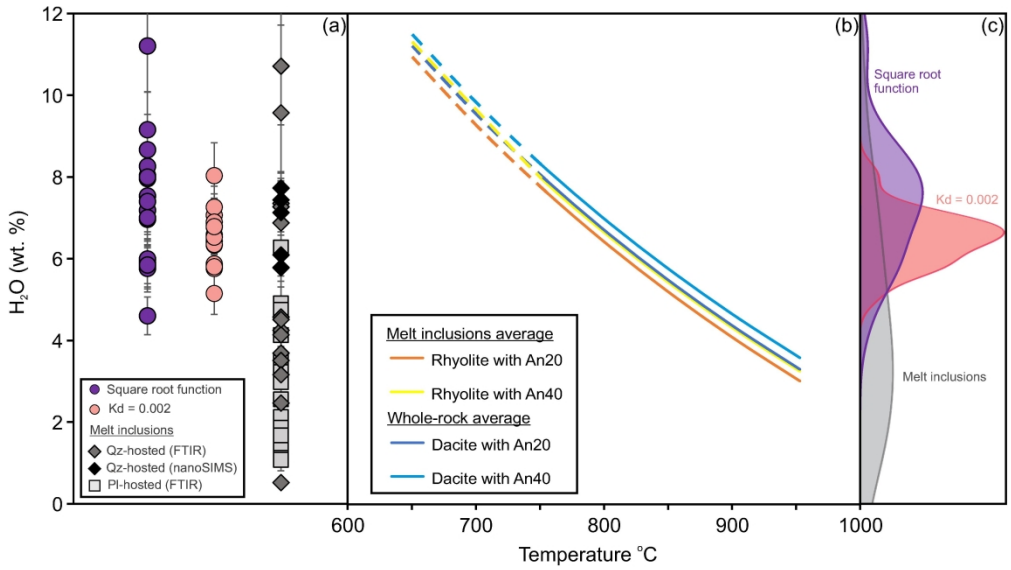

Figure 10. (a) Comparison of total water measured in melt inclusions by FTIR and SIMS, and estimates of total water in CMV melt based upon measured water concentrations in plagioclase (section 4.4). For the water-in-plagioclase partitioning calculations, we assume a partition coefficient of 0.002 (Mosenfelder *et al.*, 2020) and we also apply the square root function proposed in this study (Equation 12). (b) Plagioclase hygrometry model of Waters & Lange (2015) run at a range of anorthite contents from An_{20} to An_{40}, a range of melt compositions from dacite (corresponding to the average CMV whole rock composition) to rhyolite (corresponding to the average composition of the melt inclusions), and a pressure of 350 MPa (the maximum pressure that the model is calibrated to). Dashed lines denote extrapolation of the model to temperatures lower than 750 °C. (c) Density plots for the water data in panel a.

177x99mm (600 x 600 DPI)

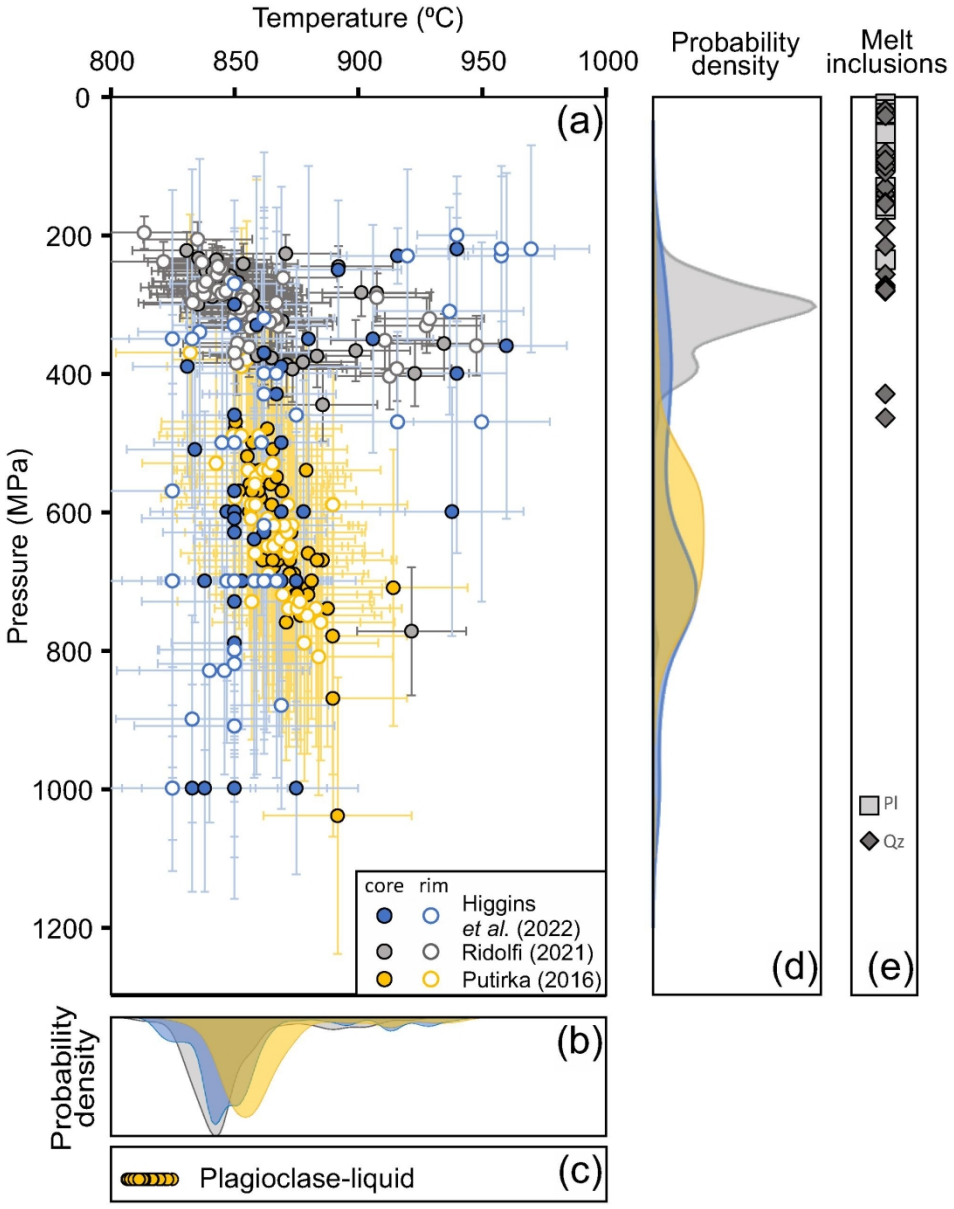

Figure 11. Pressures and temperatures of crystallization. (a) Constraints from equilibrium amphibole-liquid pairs using Putirka (2016) in yellow, Ridolfi (2021) in gray, and Higgins *et al.* (2022) in blue. Data points represent measurements in the rim (open circles) and core (filled circles) of individual crystals. (b) Probability density estimates of temperature. (c) Temperatures obtained by plagioclase-liquid equilibrium pairs using Putirka (2008). (d) Probability density estimates of pressure. (e) Saturation pressures of melt inclusions calculated by VolatileCalc (Newman & Lowenstern, 2002; see section 4.3).

85x107mm (600 x 600 DPI)

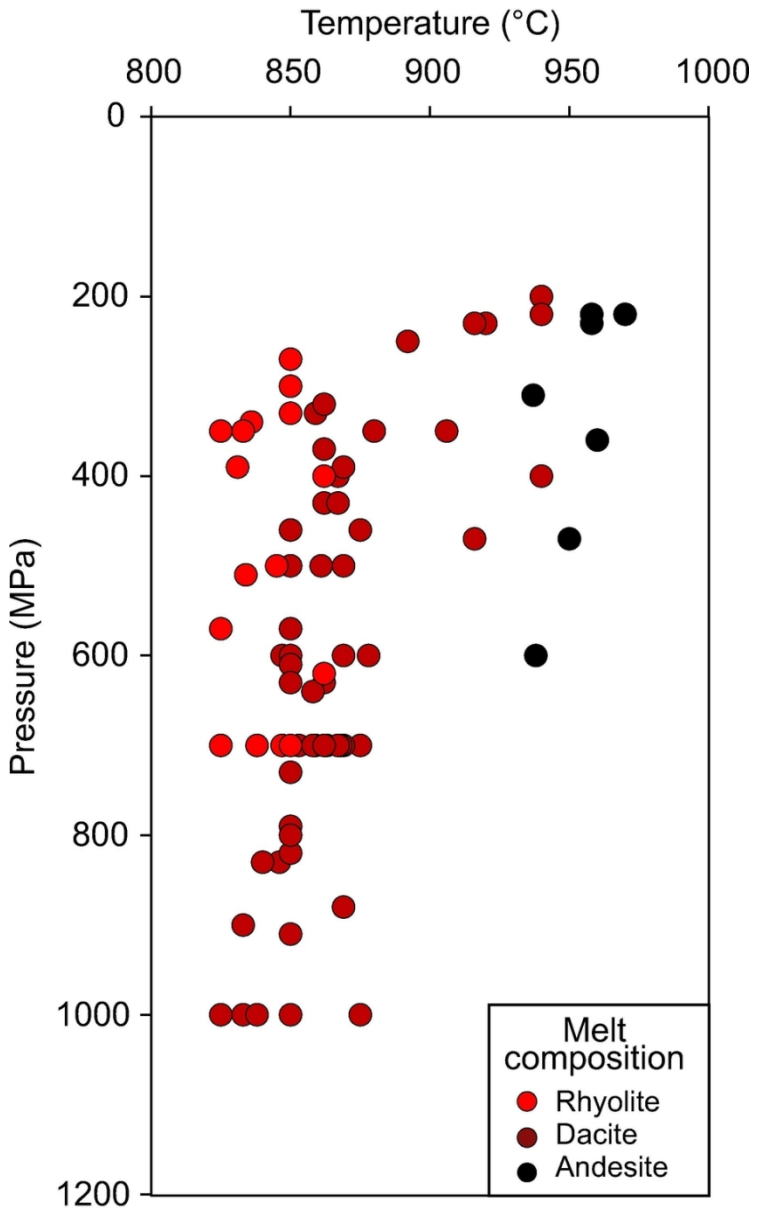

Figure 12. Melt composition based on amphibole chemometry of Higgins et al. (2022). Amphiboles crystallizing from a rhyolitic and dacitic magma are plotted as light and dark red circles, respectively. Amphiboles crystallizing from an andesitic magma are plotted as black circles.

79x129mm (300 x 300 DPI)

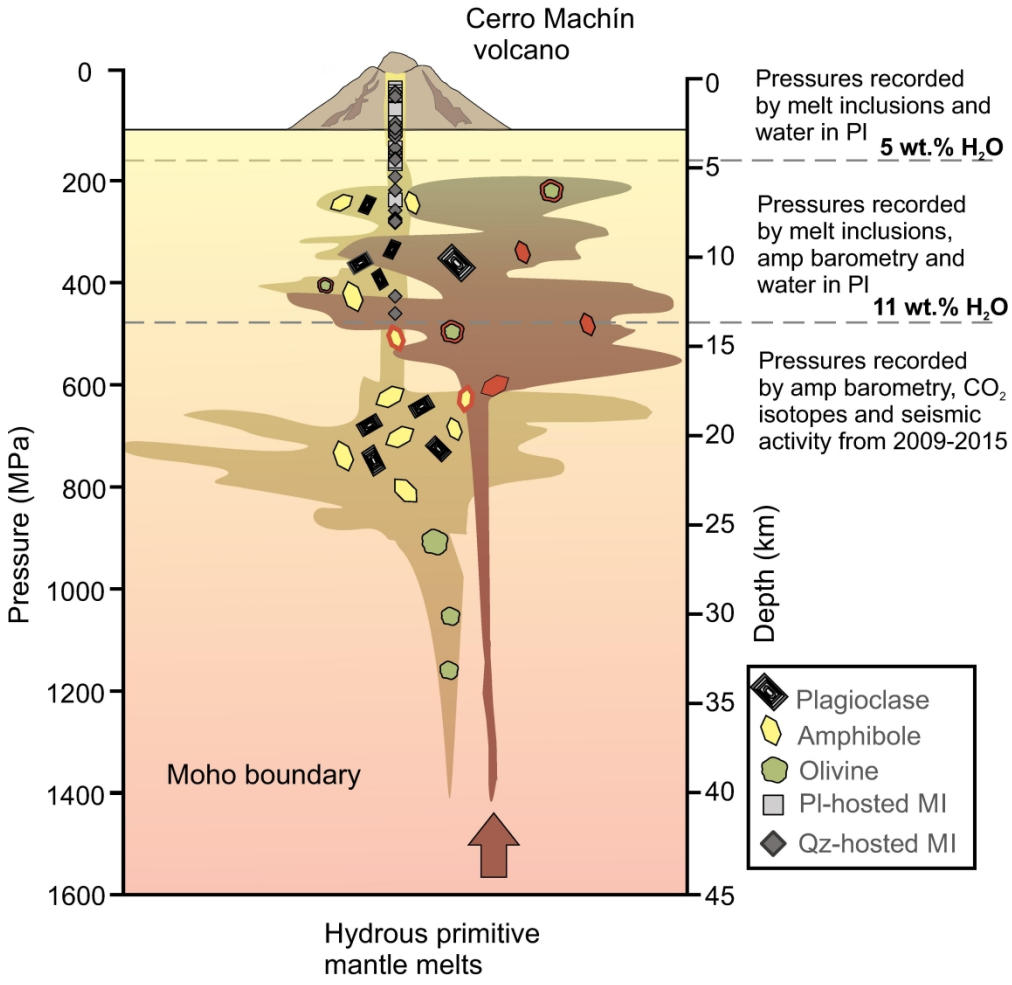

Figure 13. Summary schematic diagram representing the combined geochemical and seismic datasets. Crystallization conditions calculated from amphibole, plagioclase and melt inclusions overlap with seismicity depths at CMV from 2009 – 2015 and CO_2 isotope measurements from 2013 – 2014 campaigns (Inguaggiato *et al.,* 2017). The main dacitic reservoir is represented in green-yellowish whereas the andesitic magma recharge is in green-orangish.

168x162mm (600 x 600 DPI)

Table 3: Compositions of Cerro Machín and Pinatubo dacites (Prouteau & Scaillet, 2003), the high-Mg andesite of Mt. Shasta (Grove *et al.,* 2005), and average Cenozoic adakites (Drummond *et al.,* 1996).

	(1)	(2)	(3)	(4)
wt%				
SiO_2	63.69	64.60	63.90	56.9
Al_2O_3	16.97	16.50	17.40	17.10
TiO_2	0.62	0.53	0.61	0.36
FeO_t		4.37	4.21	
Fe_2O_3 $_t$	4.19			5.98
MgO	3.35	2.39	2.47	5.90
CaO	4.94	5.23	5.23	8.82
Na_2O	4.07	4.49	4.40	3.03
K_2O	1.89	1.54	1.52	0.74
ppm				
Cr	135	37.3	54	213
Ni	31	16.4	39	28
Sr	707	581	869	566
Y	14.4		9.5	10
Yb		1.2	0.91	
La	21	15.9	17.55	

(1) Cerro Machín (2P-B-Coarse)
(2) Pinatubo, 1991
(3) Adakites, Cenozoic
(4) Mt. Shasta, Cascade Arc (Sample 99-12A)

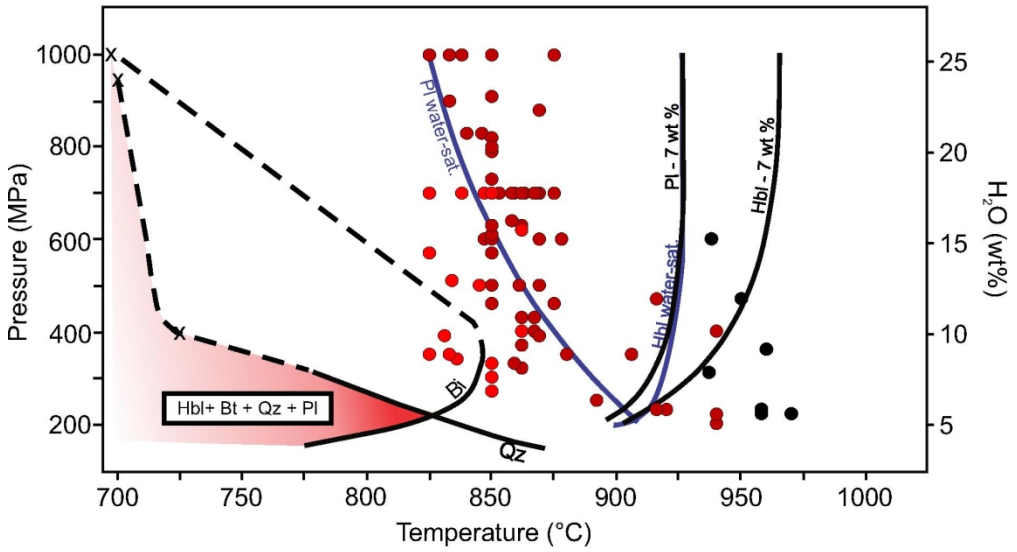

Figure 14. Phase diagram for Pinatubo dacite based on the experiments of Conrad *et al.* (1988), Prouteau & Scaillet (2003) and Rutherford & Devine (1996). Plagioclase and hornblende stability curves are shown for water-saturated magma and magma containing 7 wt% H_2O. Biotite and quartz stability curves are taken from Rutherford & Devine (1996). The dashed line for the quartz stability curve is extrapolated using Prouteau & Scaillet (2003) experiments on Pinatubo dacite at 960 MPa and 400 MPa at water saturation conditions (indicated as "x"). The dashed line for the biotite stability curve is extrapolated using Conrad *et al.* (1988) experiments on Taupo dacite at 1000 MPa at water saturation conditions (indicated as "x"). Water concentration was calculated using the VolatileCalc solubility curve for rhyolite (Newman & Lowestern, 2002). Water concentration was projected for pressures >500 MPa. CMV amphibole thermobarometry results are plotted using the same color code as Fig. 12. The P-T region in which quartz, biotite, plagioclase and hornblende are all stable is shaded in red.

80x43mm (600 x 600 DPI)

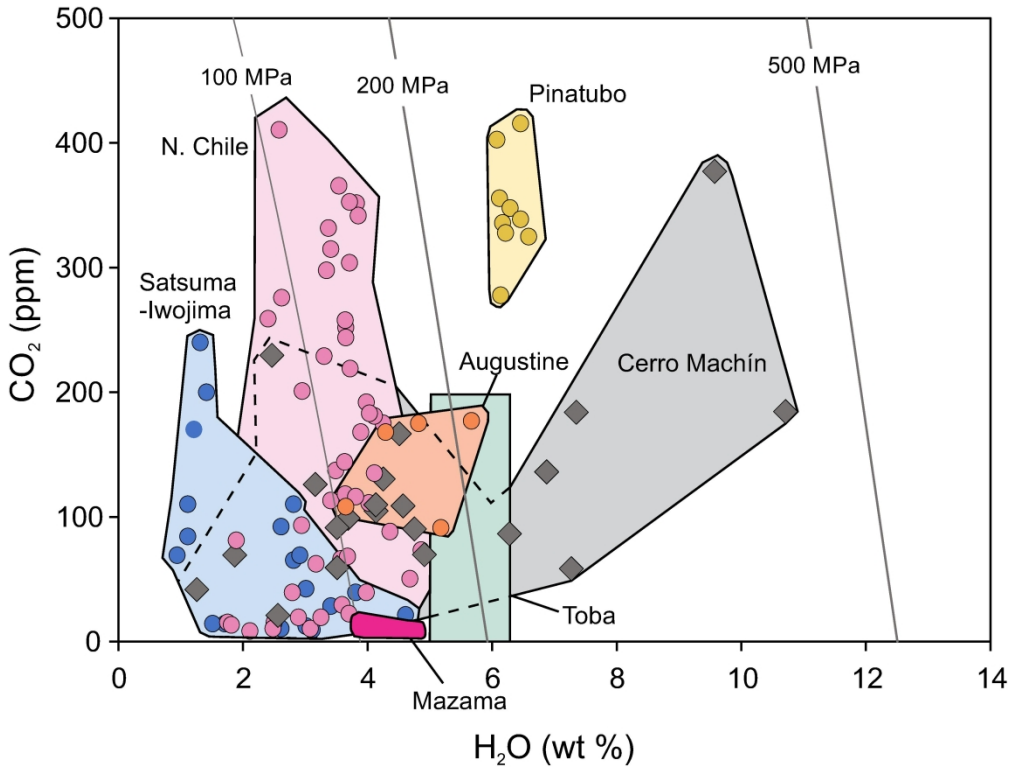

Figure 15. Compilation of H_2O vs CO_2 measurements in dacites and rhyolites from various volcanic arcs (modified from Wallace, 2005). Data are shown for the Satsuma-Iwojima (Saito *et al.,* 2001), Altiplano-Puna, Northern Chile (Schmitt, 2001), Augustine (Roman *et al.,* 2006), Toba Tuff (Newman & Chesner, 1989), Pinatubo (Wallace & Gerlach, 1994), Mt. Mazama (Bacon *et al.,* 1992). Note that Borisova *et al.* (2006) report concentrations in experimentally rehomogenized Pinatubo melt inclusions up to 8.79 wt% H_2O (by SIMS), but that study did not report CO_2 concentrations so the data are not plotted here. Isobars for 100, 200 and 500 MPa were calculated using VolatileCalc (Newman & Lowenstern, 2002).

170x129mm (600 x 600 DPI)

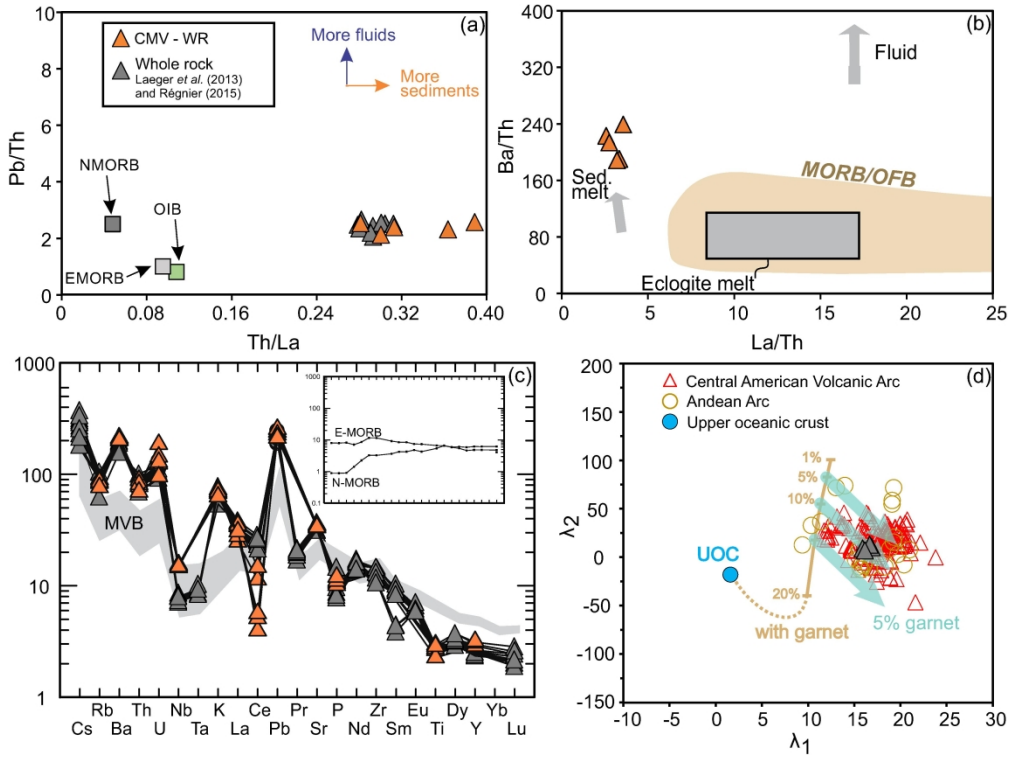

Figure 16. (a) Pb/Th vs. Th/La and (b) Ba/Th vs. La/Th diagrams support the role of melting sediments in adakite genesis. (c) Multi-element diagram normalized to primitive mantle (Sun & McDonough, 1989). Whole-rock geochemical CMV samples are orange triangles. For comparison CMV data available in the literature are also plotted (gray triangles; Laeger *et al.,* 2013; Régnier, 2015). Samples that do not exhibit a garnet signature are plotted for comparison (N-MORB, E-MORB from Sun & McDonough, 1989; the Mexican Volcanic Belt (MVB) from Straub *et al.,* 2014). (d) Petrogenetic process vectors (PPVs) of Gao *et al.,* (2023) are shown to explain the origin of CMV adakites from the rare earth element (REE) perspective. The PPVs connect the shape coefficients (λ_1 and λ_2; calculated using Anenburg & Williams, 2022 - BLambdaR program) of the upper oceanic crust (UOC) with the observed shape coefficients of CMV dacites. Approximately ~5% fractional crystallization of garnet following 10% partial melting of the UOC source provides a good match to the CMV data.

168x126mm (600 x 600 DPI)

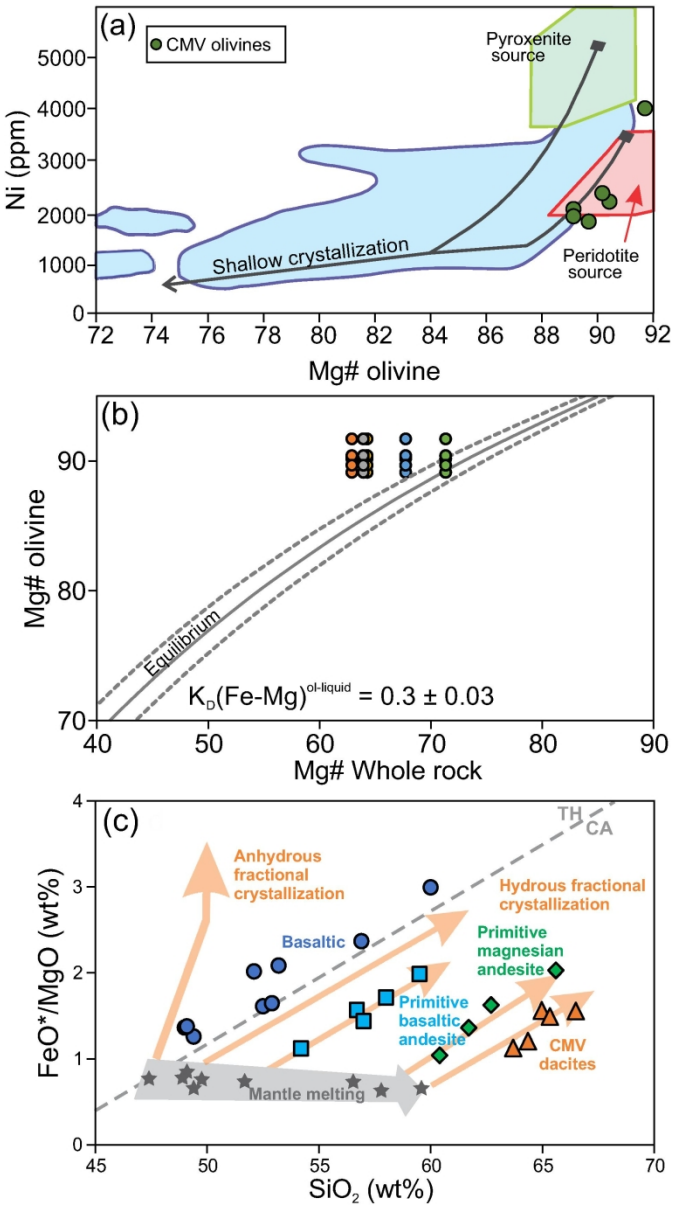

Figure 17. (a) Ni and forsterite contents in olivine phenocrysts. Green and red fields are olivines calculated to be in equilibrium with pyroxenite and peridotite source compositions (fields and shallow crystallization lines are taken from Rupretch & Plank, 2013 and Straub *et al.,* 2011). (b) The Rhodes diagram as a test of olivine-liquid equilibrium (olivine Mg# vs whole-rock Mg#). The envelope of olivine–liquid Fe–Mg distribution coefficient (K_D) of 0.30 ± 0.03 is drawn after Roeder & Emslie (1970). One whole rock composition is in chemical equilibrium with olivine. (c) FeO*/MgO versus SiO_2 diagram showing the calc-alkaline (CA) and tholeiitic (TH) dividing line of Miyashiro (1974). Primary melts defining the mantle melting array are taken from Grove *et al.* (2012). Fractional crystallization paths in H_2O magma suites are shown for three different starting compositions: basaltic, primitive basaltic andesite (compiled from Sisson & Grove, 1993), and primitive magnesian andesite (from Mt. Shasta, California, Grove *et al.,* 2003). The crystallization path for CMV dacites projects toward high-SiO_2 andesitic primary mantle melt composition. Modified after Grove *et al.* (2012).

81x146mm (600 x 600 DPI)